Tip Vortex Mitigation Using Slotted & Flexible Winglets

Master's Thesis

Jagatheaswaran Srinivasan
(5715326)

Image courtesy: Paul Bowen, Cessna Aircraft Company

TU Delft

Tip Vortex Mitigation Using Slotted & Flexible Winglets

by

Jagatheaswaran Srinivasan
(5715326)

To obtain the degree of Master of Science,
at Delft University of Technology,
to be defended publicly on
Friday August 30, 2024 at 10:30 AM.

Supervisors:	Dr.ir. Bas van Oudheusden, Dr. Morgan Li
Defense Committee:	Dr. Fulvio Scarano, Dr.ir. Leo Veldhuis
Project Duration:	January, 2024 - August, 2024
Faculty:	Faculty of Aerospace Engineering, Delft

TU Delft

Acknowledgement

Firstly I would like to thank my supervisors Morgan Li and Bas van Oudheusden for their support throughout the thesis. Thank you for being extremely patient with all my silly doubts and my insane plan to complete the thesis within 7 months, for always being available and guiding me in the right way. Particularly, I am very grateful to Prof. Morgan Li for helping me out with the experimental setup and for all the feedback on the report including the small things like how to make a contour plot look better. I would most certainly like to thank her for the delicious cupcakes she baked!

I came here with minimal knowledge of aerodynamics, and I wasn't good with coding either.But now I am happy that I can confidently say I have learned so much in the past two years, well enough to start my career as an aerodynamicist. Hence, I would like to thank all my professors and PhD students who have provided us with immense knowledge. I also extend my gratitude to the team of Formula Student Delft, where I have learned so many valuable lessons about race-car design and manufacturing.

Next, I would like to thank all the technicians who have helped me out, especially Frits Donker Duyvis for 3D printing and post-processing all the wind tunnel models multiple times! I would also like to thank Martijn Looman for helping me fix a broken wingtip, Emiel Langedijk for the help with safety measures and Stefan Bernady for helping me out with the force balance and stiffness test. I would like to thank David Bensason for lending me his VAWT mounting table for my experiments. A special thanks to Theo Michelis for helping me out with the experimental setup, Davis software issues, for the camera lens and for all the other help at LSL. Also, I convey my gratitude to Gert-Jan Berends and Marios Kotsonis for helping me transport the equipment between HSL and LSL.

I would like to thank my parents for enabling me to come so far away to chase a dream and my sister for her endless support. I feel proud to let them know that I have made it. Last but not the least, I wouldn't have stayed sane enough to finish a masters degree without my friends who made me feel home here. Thanks to everyone one of them.

Jagatheaswaran Srinivasan
(5715326)
Delft, August 2024

Abstract

The thesis work explores the primary function of slots of a winglet in the mitigation of tip vortices. Taking inspiration from real bird wingtips, the effect of the slots will be analyzed together with the effects of flexibility in the wingtips. Multiple bio-inspired wing tunnel models were designed and 3D-printed for the experiments. They were tested in a low-speed windtunnel at a low Reynolds number regime, ranging from 2.9×10^4 to 8.8×10^4. Three different experimental techniques were employed for the aforementioned purpose - the utilization of a force balance for aerodynamic force estimation, motion tracking of the wingtips of the slotted winglets and a spatially resolved 3C-2D s-PIV (Stereo Particle Image Velocimetry) analysis of cross-flow planes at different locations in the wake of the winglet. The individual drag components are estimated in non-intrusive way based on the PIV data, with the help of wake integral approaches.

As expected from the literature work, it was clear that the slots reduced the induced drag by a significant amount. The slots breaks down the tip vortex into multiple smaller ones, thus reducing its circulatory strength. The breakdown of the tip vortices could be visualized from the s-PIV results and the individual velocity component contours were analyzed. The streamwise vorticity breakdown for the different winglets was visualized in association with the flexibility of their wingtips. Additionally, the location and characteristics of the vortex cores were analyzed along with the phenomenon of vortex wandering.

By the end of the thesis, it was concluded that although slotted winglets reduced induced drag, they led to a significant increase in profile drag, resulting in higher overall drag compared to unslotted winglets. Additionally, the slots caused a loss in lift. The overall aerodynamic performance, measured by the lift-to-drag ratio, was also higher for the unslotted winglet. Among the slotted winglets, static bending was common, while wingtip vibrations were minimal. The most flexible slotted winglet had the lowest induced drag. However, the results indicate that at very low Reynolds numbers, slotted winglets deteriorate the wing's aerodynamic performance compared to unslotted ones. Among the slotted winglets, those with intermediate flexibility demonstrated the best aerodynamic performance, highlighting the importance of optimizing wingtip flexibility.

Contents

List of Figures

List of Tables

Nomenclature

Winglets

Abbreviation	Material/Definition	Slotted
PLA	Polylactic Acid	Yes
cPLA	carbon-infused PLA	Yes
TPU	Thermoplastic Urethane	Yes
norm	Normal	No

Other abbreviations

Abbreviation	Definition
AVL	Athena Vortex Lattice
CAD	Computer Aided Design

Symbols

Symbol	Definition	Unit
AR	Aspect ratio	-
b	Spanwise length: base of wing to the longest wingtip	[m]
c	Mean aerodynamic chord	[m]
D	Drag force	[N]
e	Span efficiency factor	-
E	Young's modulus	[N/mm^2 or MPa]
I	Second moment of inertia	[mm^4]
I_0	Second moment of inertia at wingtip root	[mm^4]
C_L	Coefficient of lift	-
C_D	Coefficient of drag (general)	[-]
$C_{D_{tot}}$	Coefficient of total drag	[-]
C_{D_i}	Coefficient of induced drag	[-]
C_{D_p}	Coefficient of profile drag	[-]
h	Wingtip thickness	[m]
L	Lift force	[N]
p	Static pressure	[Pa]
p_t Total or stagnation pressure	[Pa]	
Q	Q-criterion	[s^{-2}]
Re_c	Chord-wise Reynolds number	[-]
S	Cross-flow plane area	[m^2]
U_∞	Freestream velocity	[m/s]
u	x-component of velocity	[m/s]
v	y-component of velocity	[m/s]
w	z-component of velocity	[m/s]
w_i	Induced normal velocity component on wing	[m/s]
α	Angle of attack	[degree (°)]
α_i	induced angle of attack	[degree (°)]
Γ_{net}	net circulation	[m^2/s]
λ_{ci}	Swirling strength	[s^{-1}]
ω_x	Streamwise vorticity	[m^2/s]

Symbol	Definition	Unit
ϕ	Dihedral angle	[degree ($^\circ$)]
Pi_1	Effective stiffness	[-]
ψ	Stream function	[m^2/s]
ρ	Density	[kg/m^3]
τ	Viscous force	[Pa]

1 Introduction

A tip vortex (also known as *trailing vortices*) occurs wherever a lifting surface terminates [23], such as at the end of the wing where there is abrupt pressure gradient between the upper and lower surfaces of the wing. Tip vortices usually tend to trail behind the wingtip forming a vortex sheet. They can have a negative impact on the aerodynamic performance of the aircraft as briefed upon in subsection 2.0.1.

One such significant negative impact is the induced drag, and one prime benefit that could achieved from alleviating induced drag is the reduction of the take-off field length, as induced drag is the highest during take-off and landing. Also referred to as lift-induced drag to be precise, induced drag is a result of trailing wing-tip vortices [2] (explained in subsection 2.0.1), and is always a by-product of producing lift. Although the term refers to drag as a by-product of lift, the term vortex drag is used in its place often since the tip vortices can sometimes cause drag without the production of any lift. The lift-induced drag of a wing is generally given by the formula:

$$C_{D_i} = \frac{C_L^2}{\pi ARe} \tag{1.1}$$

Where e is the span efficiency factor, and AR is the aspect ratio of the wing.

For a planar wing induced drag is minimized by an elliptical lift distribution ($e = 1$), but a non-planar wing can distribute vorticity vertically allowing for even lower drag [32]. Although we have the present day winglets at the endspan of an aircraft wing, they are still under research for a better and optimized design in terms of structure and aerodynamics (refer chapter 2). Talking about non-planar wings and aerodynamics, it is not wise to ignore the natural flying beings - birds. Bird wings have been the inception point for human flight, with the earliest experiments dating back to the time of Leonardo da Vinci. The wings have evolved into diverse modifications and some give the birds the ability to fly long distances with ease. Nature has always had its way of optimizing everything and yet again, we humans have something to copy or bio mimic from - the *slotted wingtips* feature present in wings of different species of birds and its possible benefit in drag reduction.

1.1. Research Scope

As mentioned previously, wingtip slots have the tendency to reduce the strength of the tip vortex and thus reduce induced drag through a reduction in the kinetic energy transfer into the wake. However, is it possible to bio-mimic these wingtip slots from birds and incorporate it in our non-flapping aircraft wings to gain the same advantage? Is it possible to tune the flexibility of the wingtips to our advantage?

The present thesis explores the function of the slots and the flexibility of the wingtips in alleviating the negative impact of the tip vortex through its breakdown and resulting reduction in induced drag. The thesis will be primarily based on experimental analysis on a self-made wing with slotted winglets differing in the material composition and hence flexibility. Additionally, the impact of the slots and flexible wingtips on the total drag and lift will be studied. On a final note, the thesis is intended to provide a baseline for further research in flapping wing aerodynamics and bio-mimicking the vortex breakdown phenomenon for adaptations to real-world airplanes during low-speed regime, including take-off and landing.

1.2. Report structure

The report begins with the important theoretical background required along with a brief literature review (in chapter 2) of the relevant work that has been done in the past. The research objectives will be presented at the end of chapter 2. This will be followed the Methodology in chapter 3, which comprises of a discussion on the wind-tunnel model design and manufacturing, and the methodology used including the numerical models and the experimental setup. The

obtained results and corresponding inferences will be presented in chapter 4 and the report will end with appropriate conclusions in chapter 5.

1.3. Real-world Application

The real-world implications of slotted wings are plenty and we have only scratched the tip of the iceberg. A great example of upcoming concepts with bio-mimicked slotted wingtips is the Airbus *Bird of Prey* aircraft (Figure 1.1). Not only is the winglet slotted, but the wingtips or *feathers* can be controlled individually for an advanced flight control.

Figure 1.1: Airbus *Bird of Prey* conceptual aircraft [Source:airbus.com]

Additionally, slotted wingtips and bio-mimicking from birds have already been utilized in multiple research work relevant to UAVs (Unmanned Aerial Vehicles) as shown in Figure 1.2. This could of potential use in military operations and surveillance strategies.

Figure 1.2: Bionic slotted wings for UAV [20]

2

Background & Literature Review

The foundation of the literature study lies with the comprehensive study done by Dan Liu *et al.* [35] on the research work that has been done on wingtip slots so far and the future prospects of the same. According to Dan Liu *et al.*, most early work have been to compare the aerodynamic characteristics between wings with and without wingtip slots and to analyse the functions and advantages of slotted winglets. Although few in number, some of the very early works (as mentioned in section 2.1) elaborated on the possible aeroelastic effects of bird wings and wingtips made of feathers. The paper also proposes a road map for future research. As shown in Figure 2.1, the research prospect can be divided into 3 categories - Geometric dependence study in steady flow, kinematics study in unsteady flow and study of aero-structure coupling or flexibility effects of slotted wingtips.

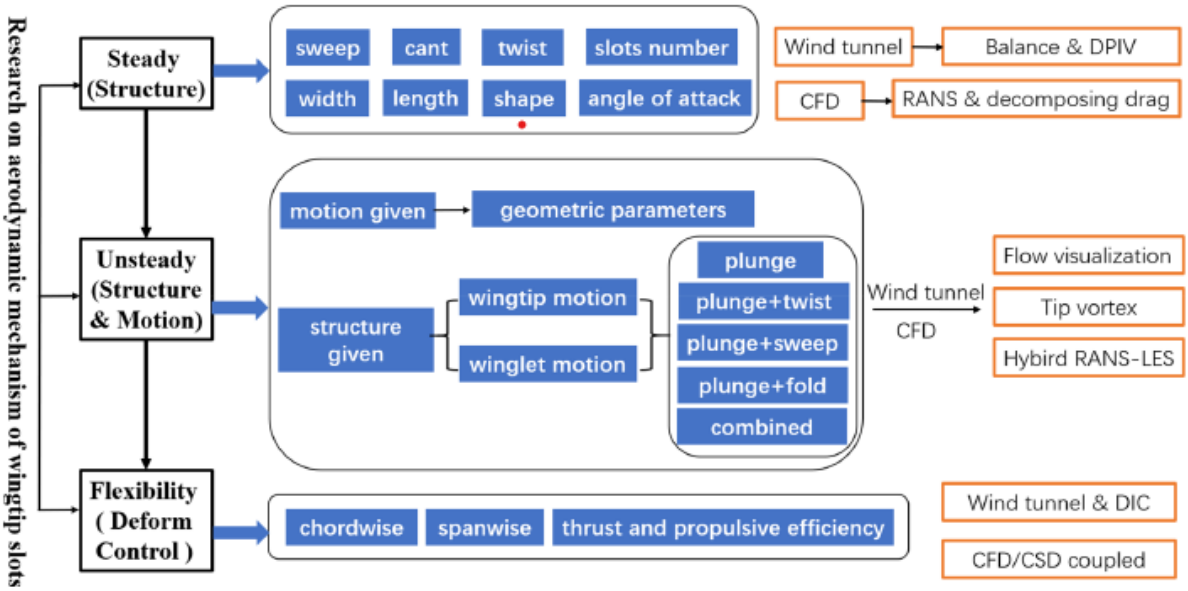

Figure 2.1: Future research possibilities on the aerodynamics of wingtip slots [35]

As mentioned in chapter 1, the category of slots in winglets and flexibility of the resulting wingtips shall be explored in this thesis work, with a particular focus on how the flexibility affects the formation of tip vortices and aerodynamic parameters. The following chapter presents the theoretical background required and an overview of the work that has been done in this field. Finally, a brief synthesis of the literature review and the formulated research objectives will be presented.

2.0.1. Tip Vortex

Starting with the very basics, the understanding of why a tip vortex is detrimental to performance is essential. Wingtip vortices could have several negative impact on the aircraft's stability and performance:

- Tip vortices cause a downwash on the wing and lower lift due to lowering of the effective angle of attack that the plane receives. This is explained by the Lanchester-Prandtl lifting line theory (Figure 2.2) and the resulting induced downwash angle is given by [29]:

$$\alpha_i \approx \frac{-w_i}{U_\infty} \tag{2.1}$$

$$w_i = \frac{1}{4\pi}\int_{-b/2}^{b/2} \frac{\frac{-d\Gamma(y_0)}{dy}dy_0}{y - y_0} \tag{2.2}$$

where U_∞ is the freestream velocity and w_i is the integrated induced normal velocity component in a wing throughout the spanwise locations $(-y_0 < y < y_0)$ due to horseshoe bound vortices of strength $\delta\Gamma = \frac{-d\Gamma(y_0)}{dy}dy_0$. And the effective angle of attack will be $\alpha_e = \alpha - \alpha_i$.

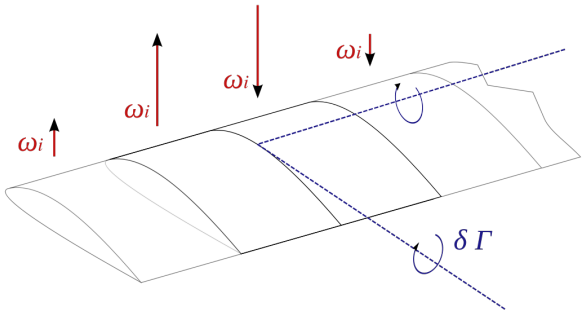

Figure 2.2: Upwash/Downwash from Lifting Line theory

- Vortex roll-up in the wake can cause alarming problems to the flights in its vicinity. As shown in Figure 2.3, directly downstream of the wingtips it can lead to an additional rolling moment on the following flight and a loss of altitude due to induced downwash in the middle [16]. Similarly, a flight travelling along a cross-plane to these tip vortices can have an imposed pitching moment resulting in additional pitching moments.
- Results in induced drag, which amounts to almost 50% of the total drag during take-off and landing [53].

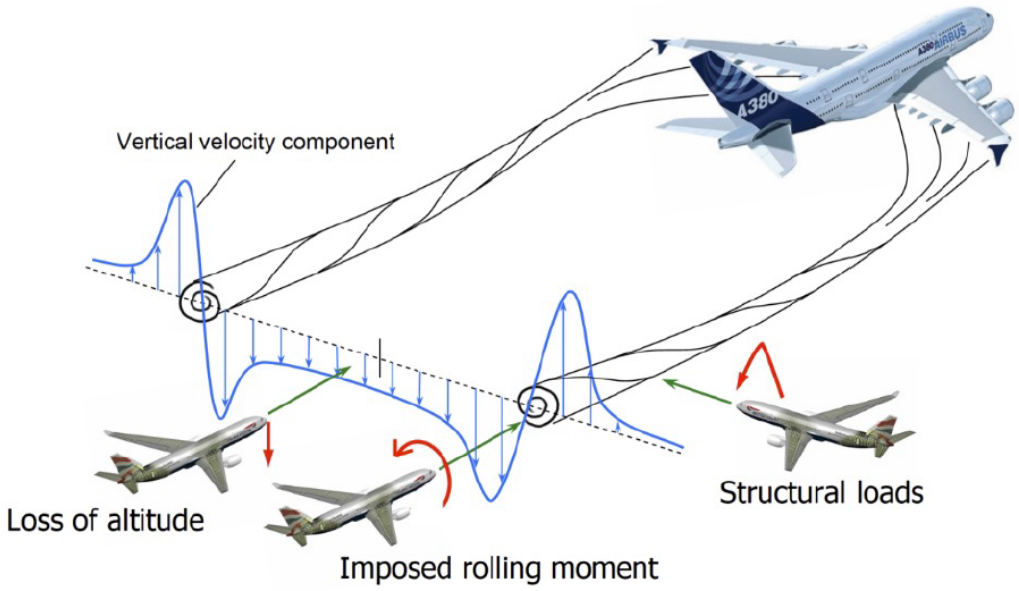

Figure 2.3: Impact of wing tip vortices [53]

Perhaps the most important question is, where do these tip vortices originate from? Green [23] has mentioned three possible explanations for the origin of trailing vortices: In the simplest way, a tip vortex can be described as the result

of a abrupt pressure gradient at the wingtip, i.e., between the upper surface of a finite span wing with lower static pressure and the lower surface with higher static pressure Figure 2.4a. Tip vortices may also be explained in terms of a shear layer that exists near the wing tip. Parallel lines in the direction of U_∞ represent the undisturbed flow some spanwise distance away from the wing, and the arrows parallel to the wing represent the in-plane component of the flow over the wing (the flow has not separated). A third explanation of trailing vortices involves the second Helmholtz vortex law. For a finite-length lift generating wing impulsively starting from rest, there must exist a net circulation around the wing (*bound vortex*) according to Kutta-Joukowski law:

$$L = \rho V_\infty \Gamma \tag{2.3}$$

Kelvin's theorem demands that this circulation be matched by an equal and opposite shed circulation (*starting vortex*). Because vortex lines can never end in a fluid, these two vortices must be connected by tip vortices, as illustrated in Figure 2.4c.

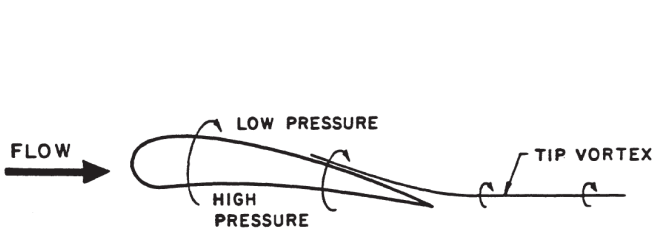

(a) Pressure field

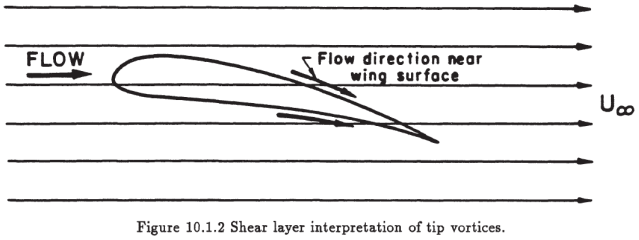

(b) Shear layer

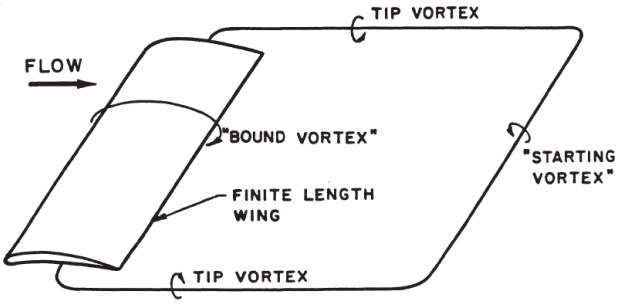

(c) Helmholtz vortex law

Figure 2.4: Various interpretations of origin of tip vortex [23]

So how do we reduce the impact of the tip vortex on the induced drag of the wing? Here in comes the concept of winglets, the non-planar wing extensions. A lot of the present-day aircraft with low AR such as a Boeing 737 possess winglets that aids in the reduction of induced drag. Reid's *multiplane theory* in 1932 [46] proposed that a multiplane (or non-planar) wing has a lower induced drag than a monoplane of equivalent area and lift if the wings have similar span, regardless of how much they are staggered. The geometry of the winglets can vary vividly depending on the requirement. The different types of winglet geometries in the current aircraft can be seen in Figure 2.5.

Figure 2.5: Types of winglets *[Source:avgeek.gp]*

Although the above mentioned winglets are performing sufficiently well in the skies, the optimization of these winglets to give better results is still in progress. Here in comes the role of bio-inspired designs from bird wings. As mentioned in chapter 1, birds have always been the source of inspiration for human flight. It is very evident that birds have evolved their wings over time to adapt to nature and improve its flight performance.

Apart from the prominent morphing capability, bird wings also possess feathers that partially or completely overlap to produce unique wing surfaces with or without slots [58]. The shape of bird wings is predominantly determined by their tip vortex behaviour [23] and each of the feather act as as an aerodynamic surface. These slotted configuration, along with the bending and twisting motion could be contribution to the high aerodynamic efficiency of bird flights during the flapping motion. These slots help in the breakdown of the tip vortex, hence reducing its strength, especially during soaring[1] flight. [7, 8, 33].

2.0.2. Bio-mimicking Bird Wings

A very prominent feature of birds is their ability to morph their wing planforms according to the flight regime and requirement. As shown in Figure 2.6, it can go from fully folded during fast dives to fully extended (thus higher AR and lift) during a soaring flight. And the soaring flight is what interests the author the most because of the notable slotted wingtips.

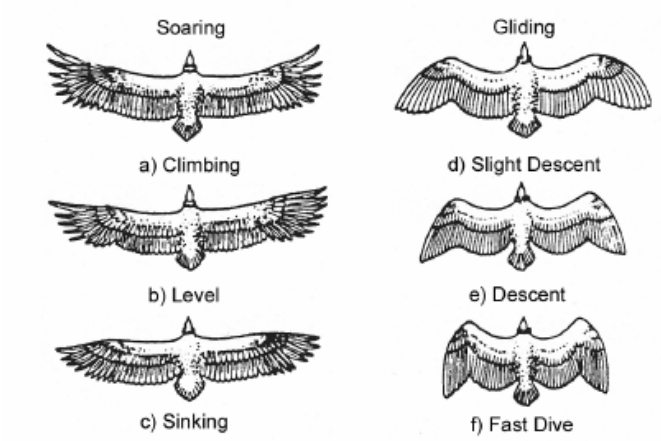

Figure 2.6: Different bird wing planforms according to the flight regime [5]

Multiple research work have been conducted on bio-inspired wing design, especially in the field of UAVs (Unmanned Aerial Vehicles). Lucas kilian *et al.* [31] took inspiration from the Carrion crow (*Corvus corone*) and American crow (*Corvus brachyrhynchos*) to design his/her wing. Both these crow species had an average wingspan of 85-100 cm and weighed around 300-600 grams. They had taken up the high-lift, low-Re *Selig S1223 airfoil* for the wing cross-section to closely bio-mimic the cross-section wing profile of real birds. The close resemblance of S1223 airfoil to a bird's cross-sectional wing profile, particularly to those of Seagull and Merganser Figure 2.7a, was earlier confirmed by Tianshu Liu *et al.* in 2006 as well.

The spanwise variation of the wing cross-section has been briefed on by Berens [5] in 2008. They showed how the camber reduces towards the slotted wingtip, along with the shift of the max camber location towards the trailing edge as depicted in Figure 2.7b.

[1] Flying over a rising current of air, usually a thermal, while remaining aloft without flapping its wings [40]

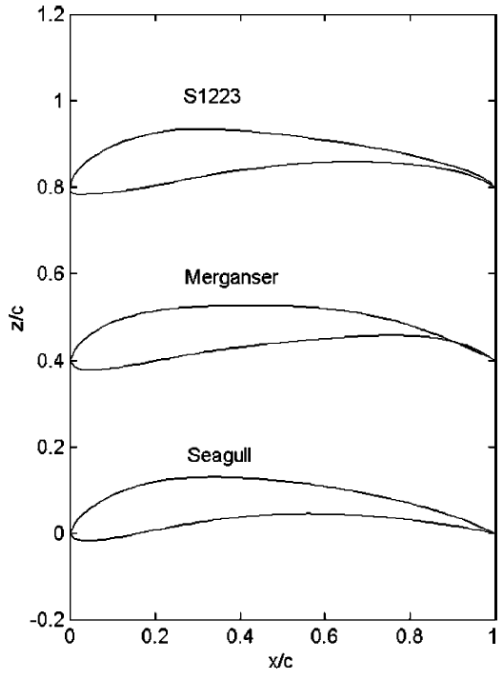

(a) Comparison between the wing cross-section of Seagull & Meganser with S1223 airfoil [36]

Tab. 4: Maximum camber values and corresponding chordwise locations.

Section:	(a)	(b)	(c)	(d)
Maximum camber m	11.0 %	9.6 %	8.2 %	5.6 %
Chordwise position of maximum camber p	20.0 %	24.6 %	31.0 %	44.6 %

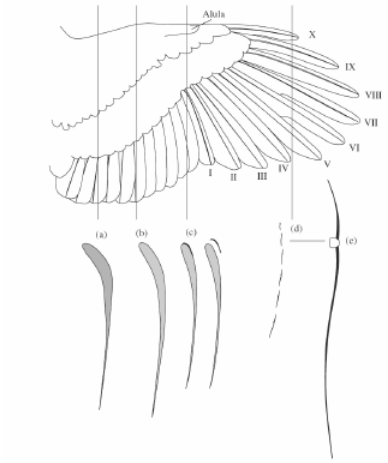

(b) Wing cross-sectional profile variation along span [5]

2.0.3. Wingtip Slots

In 2008, Berens [5] had clearly summarized the various interpretations on the functions of the slotted outer primaries of bird wings in his thesis on the potential of Multi-winglet configurations.

- Thrust production in flapping flight
- Increase of maximum lift
- Enhancement of low speed manoeuvrability
- Induced Drag reduction
- Increase of static longitudinal stability
- Mitigation of wake vortices

Many early works have tried to determine the evolutionary purpose of wingtip slots in such a context as well. Surprisingly in 1962, when flow visualization techniques were still limited, Cone [14] suggested that the function of bird wingtip slots was to reduce the drag by increasing the number of wing-tips which were shedding vortices, implying the breakdown of large vortex into more smaller ones, and also that the bent primary feathers acted as endplates which reduce induced drag. B.G. Newmann [40] stated in his paper that the opening of the wing feathers clearly increases the span of the wing and thereby reduces the trailing vortex, or induced drag, but probably at the expense of increasing the profile drag slightly. For fast gliding on the other hand, the vortex drag that decreases with the square of the speed, becomes relatively less important than the profile drag that increases with the square of the speed. In this case it is indeed beneficial to reduce the area of the wing by reducing the wing span.

In 1975, Blick *et al.* [7] conducted multiple experiments to study the aerodynamic properties of bird feathers. In his second experiment, they tried to examine Cone's speculation [15] that the slotted tip feathers of hawks, eagles and buzzards maybe responsible for their excellent soaring ability. Cone [15] had hypothesized that the flexible-slotted-tips which bend upward during flight may alter the trailing vortex pattern enough to alter the induced drag. Blick hence used a wooden wing with rectangular planform and NACA 2418 airfoil section. Two configurations were present in the same model - plain tipped and slotted-tipped with 5 wild goose bird feathers attached, at inboard and outboard sections of wingspan respectively on the same model. Wind tunnel tests were run at $49, 58 \ \& \ 70 \ ft/s$, and measurement of vorticity was done behind the wings (1.7 chord lengths) using a vorticity meter. As can be seen in Figure 2.8a, they observed 3 distinctive vortex cores (2 other cores present out of measurement plane probably) behind the slotted-wingtips, with peak vorticity less than that of the plain tip by over an order of magnitude. Figure 2.8b shows the maximum vorticities measured at the same downstream location for several wind speeds. The solid line in the figure represents the theory of McCormick [38] for maximum vorticity behind wingtips. McCormick [38] described the vorticity equation at the vortex core at a distance of Z feet downstream of wing with plain wingtips as:

$$\omega = \frac{34 C_L U_\infty}{c_0 C_{L_0}(1 + 0.00063 Z/\bar{c} C_L)} \, rad/sec \tag{2.4}$$

where U_∞ is the freestream (m/s), C_L is the wing lift coefficient, $\bar{c}$ is the mean chord length (m), C_{L_0} is the midspan section lift coefficient and c_0 is the midspan chord length (ft).

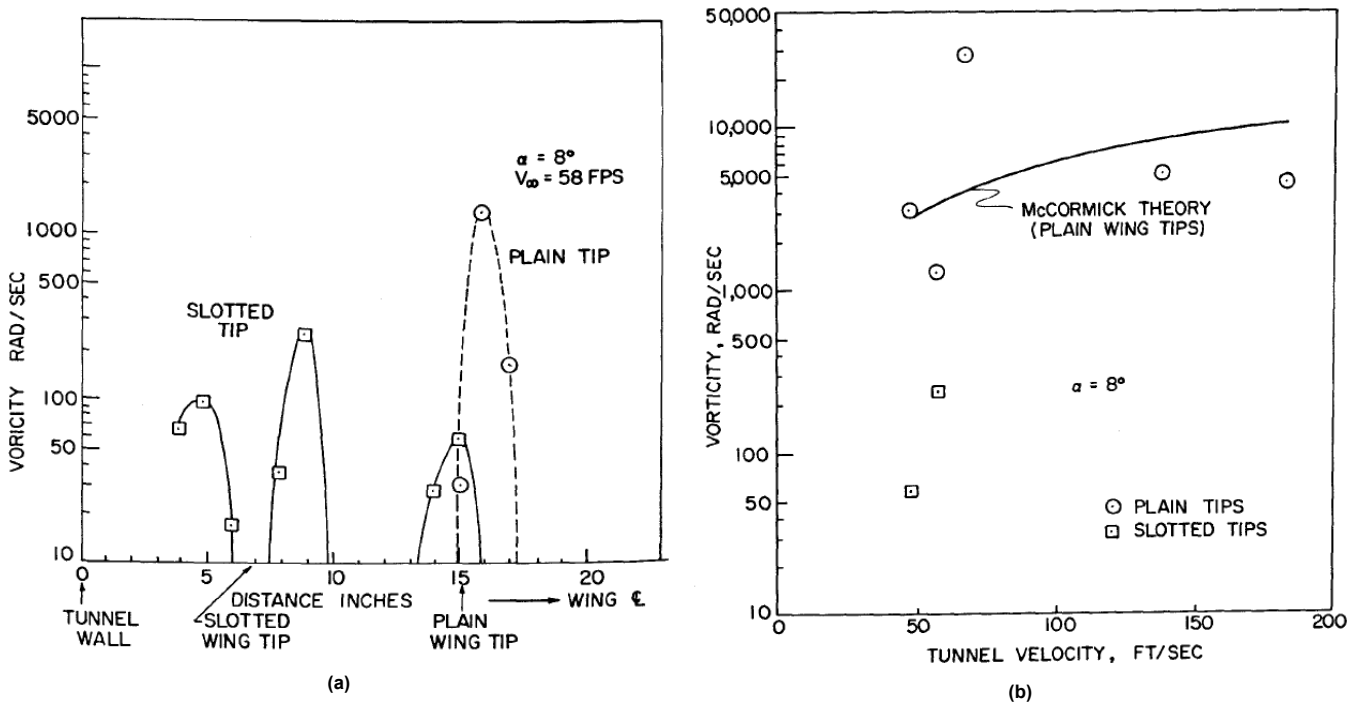

Figure 2.8: (a) Vorticity near plain & Slotted wingtips; (b) Maximum Vorticity behind wingtips [7]

In 1977, Oehme [43] suggested that wingtip slots function more as multi-planes than as leading edge slots to which they are often compared with. Later in 1981, Withers built on this idea in his investigation of a slotted Red-shouldered Hawk wing and a Black Vulture feather tips [56] and concluded that wingtip slots would increase the effective aspect ratio AR of the wing and thus reduce the induced drag. However, Reid had also suggested that the actual reduction in induced drag is negligible for multi-planes with more than about 3 wings [46], which might require a re-investigation.

In 1987, Spillman *et al.* [50] conducted an analysis of wing tip sails, structures closely resembling the slotted winglets in our case. His preliminary studies suggested that since there is a large variation in the flow incidence angle at the wing tips, the sail incidence could be varied for a reduced fuel consumption and wing weight overall could be achieved and flow separation effects minimised, due to a resulting reduction in wing bending moment under gusty or manoeuvring conditions. The aforementioned reduction in fuel consumption could possibly be a result of reduced drag.

In 1993, V. A. Tucker [51] experimentally proved that for 3 configurations composing a common base wing and different winglets - one configuration made of hawk's feathers and two made of balsa wood, the slotted tips indeed does reduce the drag because of the tip feathers being exposed to upwash at the end of base wing. The feathered wing tip was slotted and was made of four primary feathers from a Harris' hawk *(Parabuteo unicinctus)*. Out of the two balsa wood configrations, the unslotted configuration was shaped to a Clark Y aerofoil tip. The other one was made of three balsa wood wings shaped like feathers. The base wing in a wind tunnel at an air speed of $12.6 m/s$ generated upwash angles as high as $15°$ at the end of the wing when the angle of attack of the wing was $10.5°$. The feathered tip responded to upwash by increasing its lift to drag ratio (L/D) by 107% from 4.9 to 10.1, as the angle of attack of the base wing increased from $4°$ to $14°$. The L/D values of the balsa feather tip and the Clark Y tip increased by 49% and 5%, respectively, for the same change in angle of attack. They also confirmed through flow visualization the wing theory which states that winglets reduce induced drag by spreading vorticity, both horizontally & vertically.

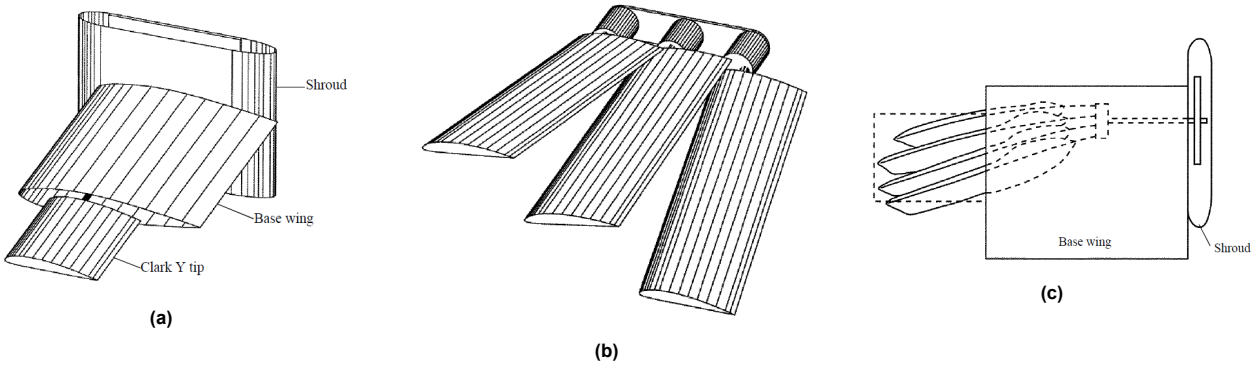

Figure 2.9: (a) Clark Y tip (single, unslotted) (b) Clark Y tip (slotted) (c) Bir feather tips [51]

Recently, Daniel *et al.* [18] also made a similar observation through a stereo PIV experiment that a wing with *featherlet*, a slotted winglet configuration (shown in Figure 2.10), created distinct pockets of vorticity with no clear vortex cores at the two PIV planes analysed in the wake region.

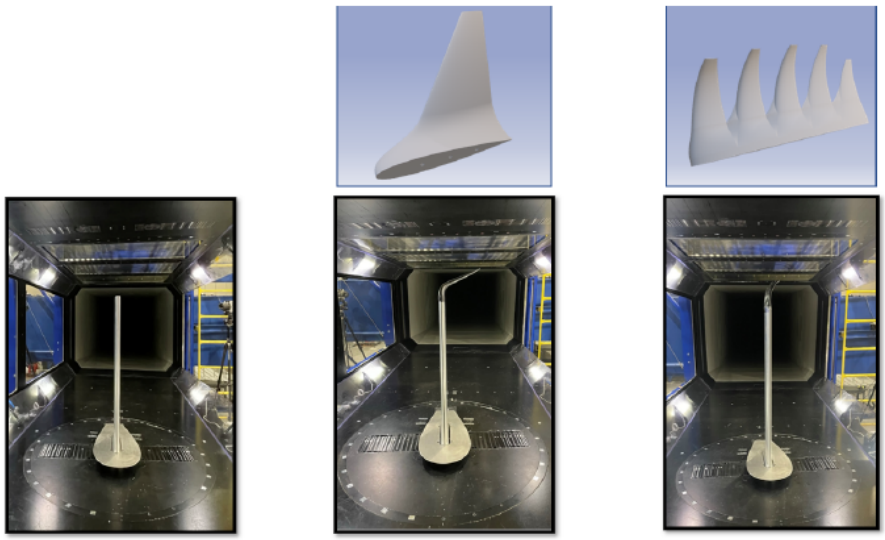

Figure 2.10: Wing Configurations used in [18]:
a. Base wing configuration b. With a winglet c. With a *featherlet*

The vortical structures in this case seemed to be more diffused than in the cases with just a base wing or a regular winglet. Interestingly, at the closer plane 1, the streamlines indicate a distorted vortex core, while at plane 2, the vortex core appears more organized and circular, as shown by the pseudo-streamlines. The velocity deficit at the vortex center is also lower at plane 2 than at plane 1 Figure 2.11a. This occurs because the vortex wake expands, drawing higher momentum fluid into the core as it moves downstream, resulting in a larger, more diffused vortex. At the upstream location ($x/c = 0.7$), there are five regions of concentrated vorticity, likely corresponding to small vortices generated by the five featherlets Figure 2.11b. At the downstream location ($x/c = 2$), these five regions are not seen. Instead, three distinct regions of concentrated vorticity form a larger region, with the largest of the three approximately at the center of the weaker vortices' larger region. However, Daniel *et al.* did not measure or analyze the induced drag from the breakdown of the tip vortex.

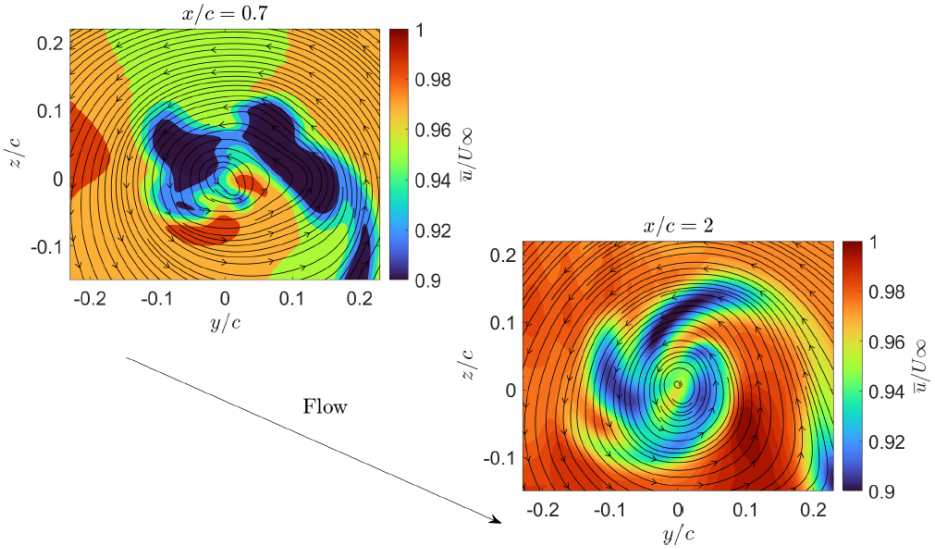

(a) Streamwise mean velocity $\bar{u}/U_\infty$ of "featherlet" for Plane 1 (top) and Plane 2 (bottom)

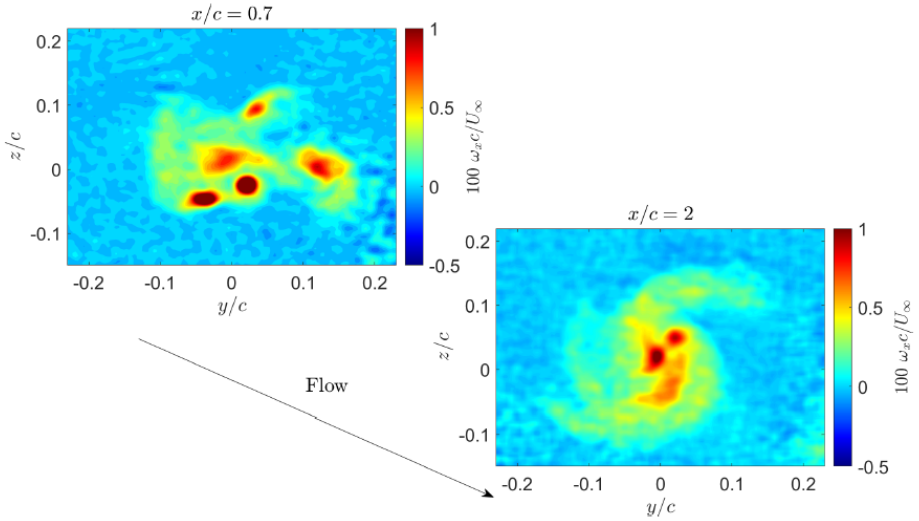

(b) Mean vorticity $\omega_x c/U_\infty$ of "featherlet" for Plane 1 (top) and Plane 2 (bottom)

Figure 2.11: Cross-planar PIV results from [18]

Tucker [51] and Cone [14] had also suggested that the vertical separation of the outer primaries of large thermal soaring birds to be a common adaption to improve span efficiency. However, KleinHeerenbrink [32] disapproved of this theory since they didn't observe any such span efficiency gain during his thesis work.

In KleinHeerenbrink's paper on multi-core vortices, [33], it has been mentioned that many bird species that specialize in gliding flight seems to not exhibit a slotted wingtip configuration and instead have evolved high aspect ratio wings. This is indeed an alternative to reduce induced drag and is achieved through extending their primaries to form a pointed wing, as can be seen in birds such as Albatross and Petrels. On the other hand, feather emarginations indicating a slotted configuration are found in many bird species that neither soar nor glide across the avian phylogenetic tree[21] and among the most basal lineages of birds, including species that only fly occasionally (e.g. *Tinamiformes, Galliformes*). Hence, intrigued by the possibility of a more general function and benefit of a slotted wing tip rather than for gliding flight only, KleinHeerenbrink *et al.* [33] conducted an experimental analysis and showed that the slotted wingtips of a Jackdaw bird wing created a multi-core vortex system in its wake (can be seen in Figure 2.12). The resulting multi-core tip vortex from the multi-slotted wingtips was proven to increase the maximum lift coefficient and hence maximizing the available thrust and aerodynamic efficiency of the wing by spreading the vorticity in both powered and gliding flight [49]. On a side note, Prantik D. *et al.* [20] showed that a modelled wing based on an Albatross wing showed clear indications of a reduction in induced drag when analyzed.

One notable difference in the visualization of the broken down tip vortex is that, contrasting to KleinHeerenbrink's [33] work, the analysis of bio-mimicked man-made *'featherlet'* by Daniel *et al.* [18] which confirmed the presence of no clear vortex cores at both the chosen downstream locations. Hence, this raises a question of whether the vortices are becoming more diffused, or if the bio-mimicry was missing an element, say flexibility of the wingtips? It is also important to note that KleinHeerenbrink made the bird fly into the PIV cross-plane during the experiment, whereas Daniel *et al*. had a stationary wing-winglet configuration which points out to different testing methodologies.

In his PhD thesis (paper 5) [32], KleinHeerenbrink mentions that although it was clear about the advantage if reduction in induced drag, the vertical separation of the tips is expected to come at a cost in terms of friction drag, which is inversely related to the chord Reynolds number. In case of laminar flow the friction drag coefficient $c_f = 2.66/\sqrt{Re_c}$ [2], so that splitting the aerofoil in N parts increases friction drag $\sqrt{N}$ times. This means that the benefit of primary separation must at least outweigh this cost. They inferred through his experiment that each of the separated primaries has its own drag wake. However, the cost-to-benefit ratio of having slotted wingtips remains to be examined in gliding flight. A contrasting yet interesting point from the same thesis (paper 1) is that they has mentioned the results did not find a relation describing how the separation of the primary feathers is an adaptation to improve span efficiency as quoted by previous works [5, 14, 51].

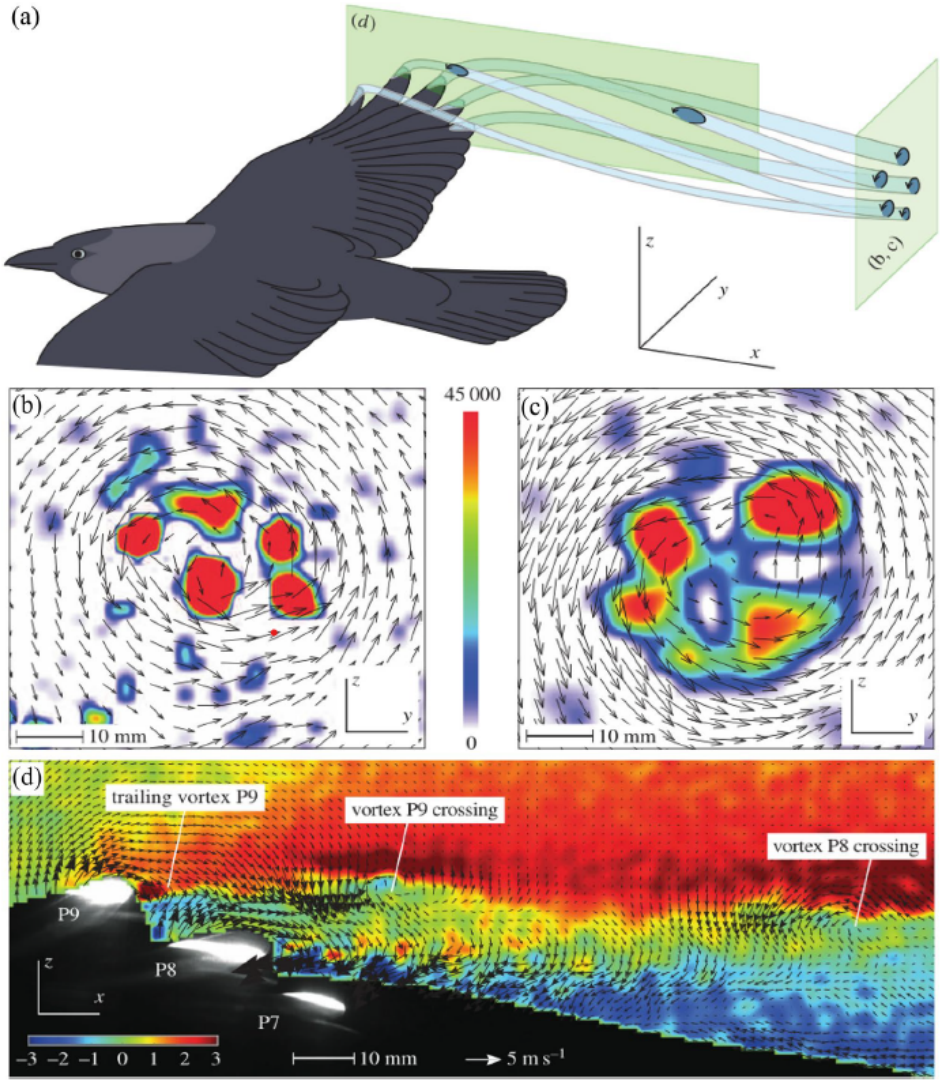

Figure 2.12: Wingtip vortex of a Jackdaw's wing [33]

2.1. Flexibility effects

Blick [7], in his first experiment, determined the relation between the compressive modulus of the feathers and the bird maximum level flight speed. The feather compressive modulus was defined to be the applied pressure on the feather during experiment $(Force/Area)$ divided by the relative deflection of the feathers $(\Delta s/s)$, where s is the thickness of the bird's chest feathers. Estimating the flying speeds from available literature, they plotted the feather compressive

modulus versus maximum level flight speed of the particular species, as shown in Figure 2.13. They concluded that in general higher compressive moduli were associated with birds with high speeds, and that the compressive modulus was proportional to the velocity squared. This implied that the stiffness of bird feathers were proportional to the maximum dynamic pressure.

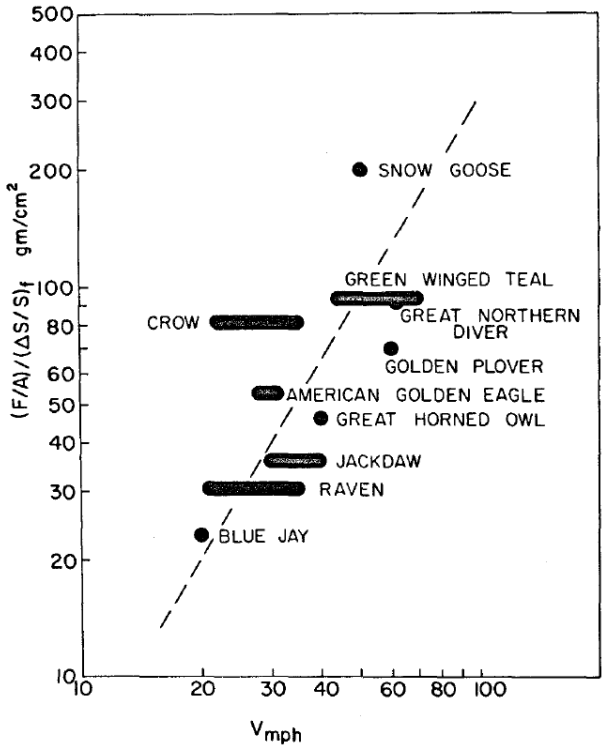

Figure 2.13: Feather compressive modulus *vs* flight speed for different birds [7]

In the same investigation of slotted Red-shouldered Hawk wing and Black Vulture feather tips [56], Withers P. C. also tried to re-evaluate the role of the wing-tips and the possible role of flexibility in it. As shown in Figure 2.14, they determined the aerodynamic forces and moments as a function of angle of attack. From the plot shown in Figure 2.15a, One noteworthy finding they made was that because the proximal or distal part of the vulture feather was always at a higher α, the drag was significant at lower velocities. The drag was significantly decreased at higher velocities, though, as the proximal and distal tips of the vulture feather twisted into a plane closer to the air flow. As visualized in Figure 2.15b, Withers regarded the evolution of wing-tip slots to the compensate for the low-aspect ratio bird wings with biomechanical strength limitations.By allowing the anterior primary feathers to bend up more than the posterior ones, slotting reduces the likelihood of wingtip stall caused by higher angles of attack and pitching moments that result in steep pressure gradients. Slotting also enables each primary feather tip to function as an independent aerofoil. KleinHeerenbrink in his PhD thesis [32] had also suggested that during flapping the outboard sections of a bird's wing experience an increased effective angle of attack, which can be mitigated by aeroelastic twist of the individual tip feathers.

In another experiment [57], Withers found that wing twist can markedly increase $C_{D_{in}}$ by simultaneously producing positive and negative lift (which algebraically cancel out so C_L is low) but drag is high since the induced drags from positive and negative lift add together, rather than cancel [57]. Such an effect of wing twist on $C_{D_{in}}$ is seen in the aerodynamic data not as induced drag, but as an apparently high profile drag coefficient. The high twist of bird wings thus contributes to their high $C_{D_{pro}}$ and probably explains why the minimum drag coefficients were often not observed at the angle of zero lift.

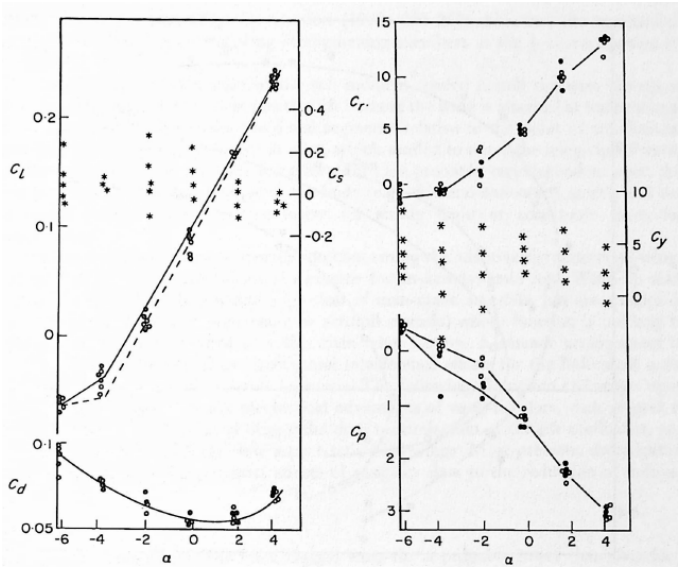

Figure 2.14: Aerodynamic forces & Moments for a hawk *(Buteo Linearis)* wing [56]
Lift coefficient C_L; Drag Coefficient C_d Side force coefficient C_s, Pitching Moment C_p; Roll moment C_r; Yaw moment C_y as a function of angle of attack (α)
○: Slots covered with tape ●: Slots open

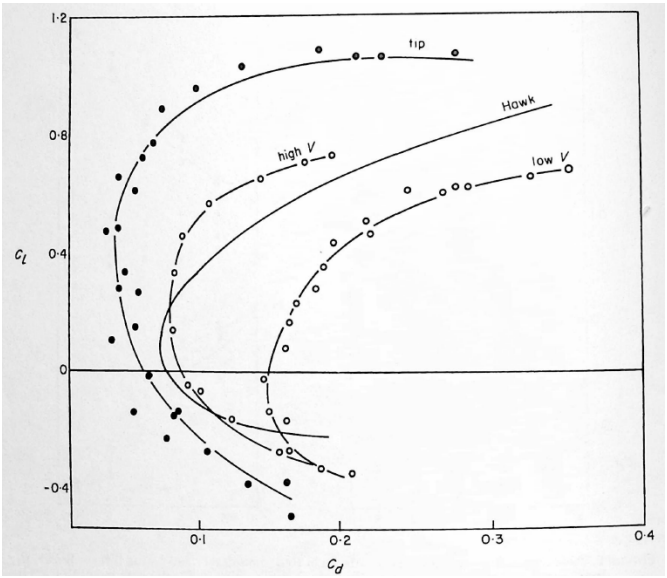

(a) Lift-drag polar for a black vulture feather tip at high $(12 - 26m/s)$ & low $(6 - 8m/s)$ velocities and a red-shouldered hawk wing

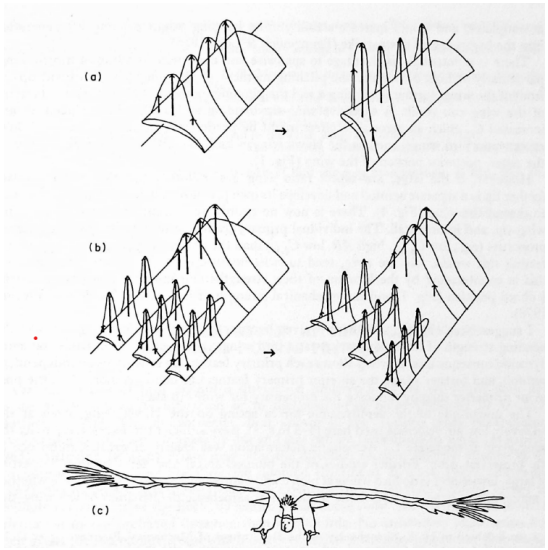

(b) Pressure distribution *(approx.)* over the top of (a)non-slotted (b)slotted wing; (c) Pattern of spanwise & chordwise bending of the primary feathers for a White-headed Vulture during landing

Figure 2.15: Important results from Withers *et al.* [56]

Lucas kilian [31] had studied the phenomenon of morphing in bird wings and its effect on the aerodynamic parameters such induced drag C_{D_i}. They had built an extensive wing model based on bio-mimicking an American crow's wings, including the cross-sectional airfoil profiles and tested it in a wind tunnel in extended and folded conditions. They used tufts to visualize the flow (Figure 2.16b) and the obtained plots for the various aerodynamic parameters for the fully extended configuration can be seen in Figure 2.16a.

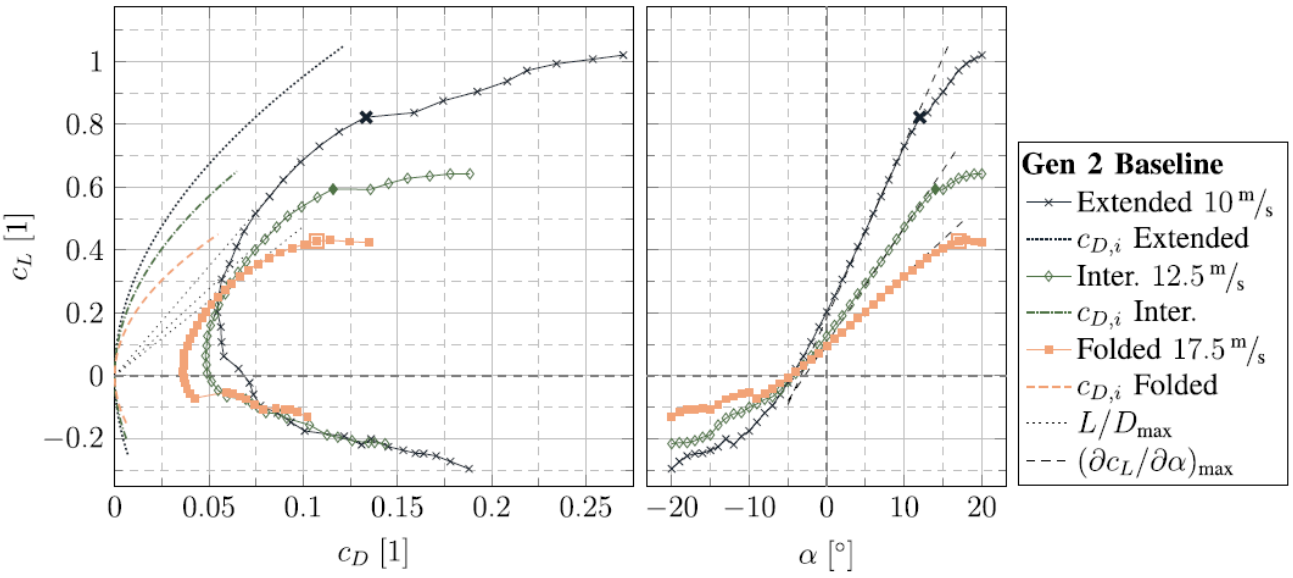

(a) Comparison of wing extensions for Gen 2 baseline at the respective optimal velocity. Induced drag C_{D_i}, best glide coefficient $(L/D)_{max}$ and maximum lift slope $(\partial C_L/\partial\alpha)_{max}$ are provided. The highlighted measurement points represent the point of maximum lift coefficient $C_{L_{max}}$

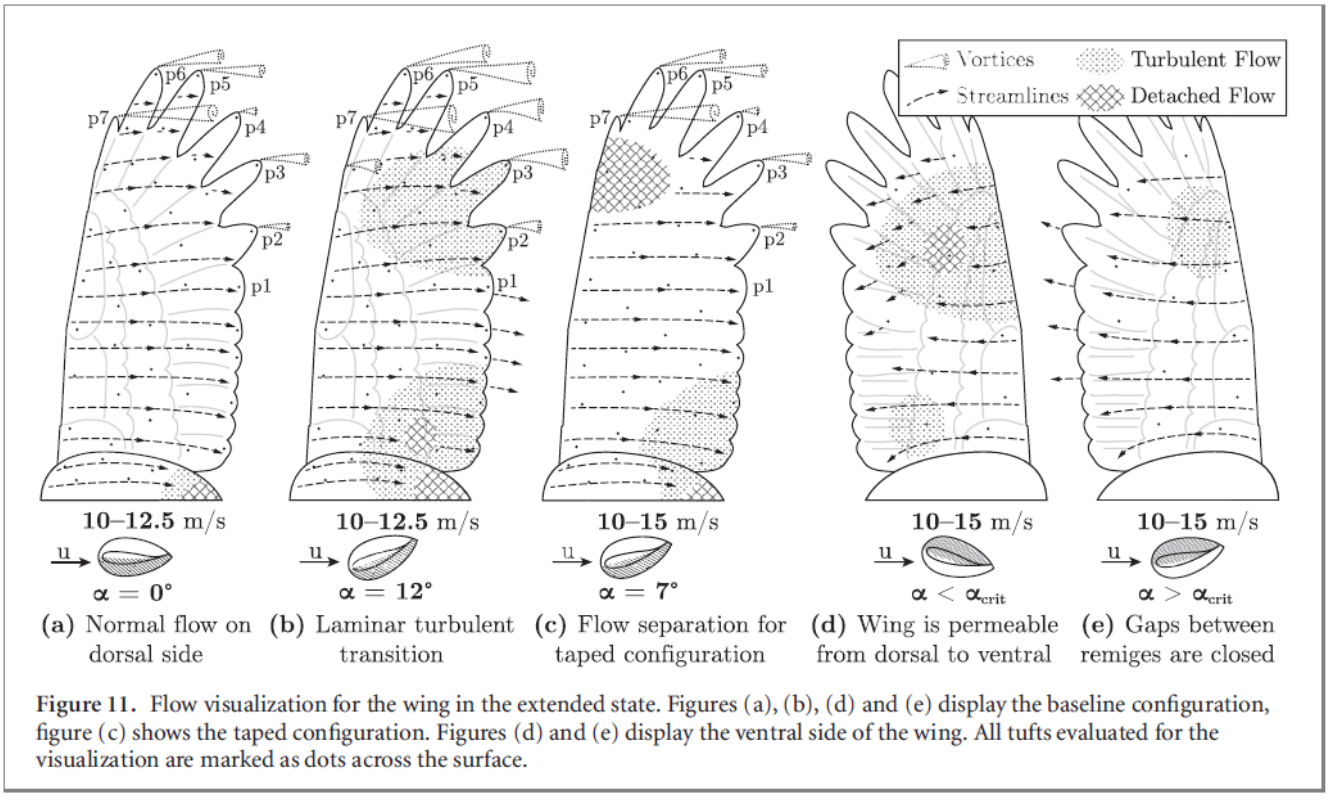

(b) Flow visualization for the wing in the extended state. Figures (a), (b), (d) and (e) display the baseline configuration, figure (c) shows the taped configuration. Figures (d) and (e) display the ventral side of the wing. All tufts evaluated for the visualization are marked as dots across the surface

Figure 2.16: Analysis of Morphing in bird wings [31]

2.2. Vortex dynamics and instability

Widening the perspective a little more about tip vortices, an important field of study are the dynamics and instability characteristics of a vortex. Three factors can be used to draw conclusions about the characteristics of vortex instability: vortex wandering, short wavelength instability, and long wavelength instability [12]. One of the most significant studies on long-wavelength instability was carried out by Crow [17], who modeled the phenomenon and explained it in terms of three combined effects:

- Self-induced rotation in the opposite direction of the core fluid's rotation;

- Motion induced by the other vortex
- Mutually induced motion of two vortices

Short-wavelength instability originating from the resonance mechanism of two Kelvin modes is another important instability event of the trailing vortex that corresponds to Crow instability. One of the other forms of vortex instability is vortex wandering, which is quantified by the instantaneous vortex core locations in the measured section. Vortex wandering is defined as the low-frequency coherent side-to-side motion of the vortex in the surrounding flow.

Cheng *et al.* [12] investigated the vortex instability characteristics of 3 wingtip configurations, through eigen value spectrum and perturbation modes. Their most highlighting conclusions were:

- First, as vortex wandering alters the tangential velocity and streamwise vorticity of trailing vortices, it pollutes the value of induced drag by roughly 3%.
- Second, the trailing vortex evolution and produced drag are further influenced by the growth rate and penetration depth perturbation mode. More turbulence specifically injects inside the vortex core at bigger growth rates and penetration depths, which results in a faster and more intense attenuation of the trailing vortex and a lesser induced drag.

Cheng *et al.* [12] also showed that the wandering amplitude increases with the chordwise Reynold's number (Re_c) while decreases with the angle of attack (α) at a given streamwise location. Furthermore, as anticipated, the wandering amplitude increases in tandem with the streamwise location model, suggesting that the instability is amplified throughout the trailing vortex's evolution to the far field. This can be explained by the trailing vortex's Q parameter, which progressively becomes closer to both the streamwise location and the unstable zone.

In the recent article on Flexible-Slotted Winglets [39], Midemer *et al.* had studied the vortex dynamics of a self-made bio-inspired design Figure 3.5, including the movement of the instantaneous vortex core locations (shown in Figure 2.17).

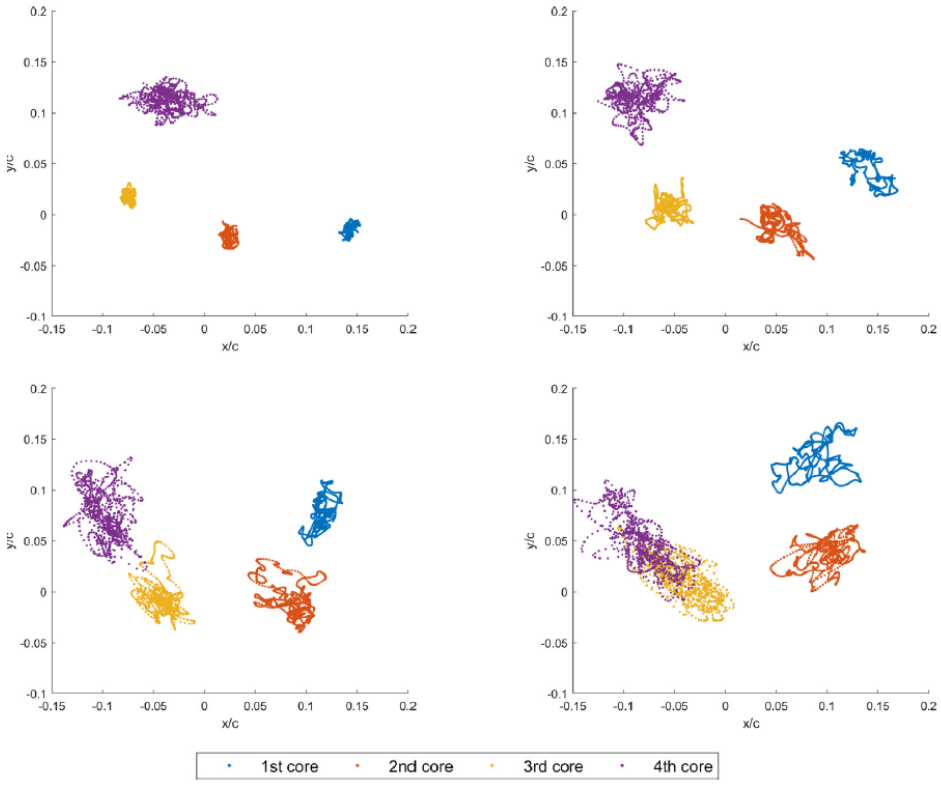

Figure 2.17: Scatter plots of the instantaneous vortex core locations of the four strongest vortices in C-type configuration (refer Figure 3.5) at $Re = 90,000$, $\alpha = 5°$ and 0, 0.5, 1 and 1.5 chords downstream respectively

They had also used the vortex identification criterion λ_2, which is described as the second invariant of the local pressure Hessian [11, 26]:

$$\lambda_2 = \frac{\partial u}{\partial y}\frac{\partial v}{\partial x} + \frac{1}{2}\left[\left(\frac{\partial u}{\partial x}\right)^2 + \left(\frac{\partial v}{\partial y}\right)^2 + \left|\frac{\partial u}{\partial x} + \frac{\partial v}{\partial y}\right| \sqrt{\left(\frac{\partial u}{\partial x} - \frac{\partial v}{\partial y}\right)^2 + \left(\frac{\partial u}{\partial y} + \frac{\partial v}{\partial x}\right)^2}\right] \tag{2.5}$$

The λ_2 criteria contours for the Time resolved particle image velocimetry (TR-PIV) for the wing configurations in Figure 3.5 are shown in Figure 2.18.

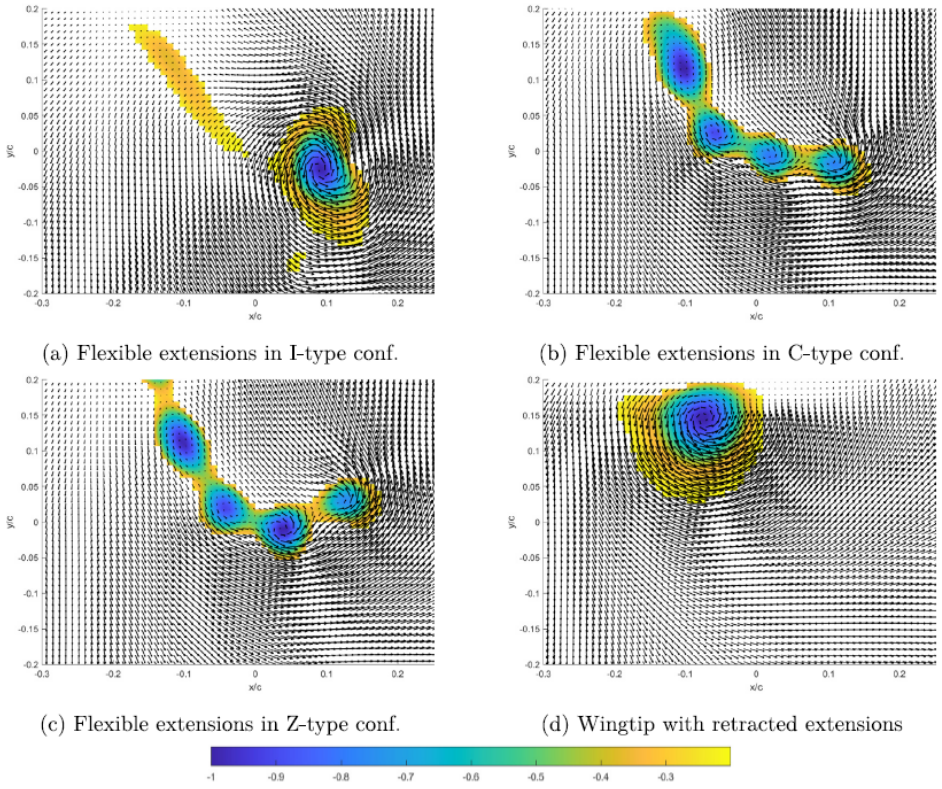

Figure 2.18: Contours of lambda-2 criterion, in the fully deployed and bird-like configurations (refer Figure 3.5) at $Re = 70,000$ and $\alpha = 10°$.

2.2.1. Q Criterion

Distinctive identification of vortex cores are essential to studying its dynamics. Qigang Chen [11] has compared multiple vortex identification criteria for a 2D flow such as $\Delta, Q, \lambda_{ci}, \lambda_2$ criteria. Among these, the second invariant of ∇u, the Q criterion deserves a special attention. Initially introduced by Hunt *et al.* in 1988 [25], the Q criterion for a full velocity gradient tensor in incompressible flows can be decomposed into two parts and written as:

$$Q = \frac{1}{2}\left(||\boldsymbol{\Omega}||^2 - ||\boldsymbol{S_T}||^2\right) \equiv \frac{1}{2}(u_{i,i}^2 - u_{i,j}u_{j,i}) \tag{2.6}$$

where $\boldsymbol{\Omega}$ is the *rate of rotation* tensor corresponding to pure rotational motion and $\boldsymbol{S_T}$ is the *rate of strain tensor* corresponding to the pure irrotational motion:

$$\boldsymbol{\Omega} = \frac{1}{2}[\nabla \boldsymbol{U} - (\nabla \boldsymbol{U})^T]] \qquad \boldsymbol{S_T} = \frac{1}{2}[\nabla \boldsymbol{U} + (\nabla \boldsymbol{U})^T]] \tag{2.7}$$

For a 2D velocity data, Equation 2.6 can be simplified to obtain a 2D Q-criterion equation:

$$Q = \frac{\partial u}{\partial x}\frac{\partial v}{\partial y} - \frac{\partial u}{\partial y}\frac{\partial v}{\partial x} - \frac{1}{2}\left(\frac{\partial u}{\partial x} + \frac{\partial v}{\partial y}\right)^2 \tag{2.8}$$

Alexander Heintz [24] in his article on *Influence of Configurational Parameters on the Vortex System of a Rotor in Hover* has described his work on visualizing secondary vortices that arise from the primary tip vortex of a helicopter blade. Obtaining data through high and low speed PIV systems, they had used the Q criterion to identify the location of these secondary vortices, after the swirling strength λ_{ci} Equation 2.9 had failed to provide reliable data due to low resolution in vortex cores.

$$\lambda_{ci} = max\left[\tau\left[\frac{1}{2}\left(\frac{\partial u}{\partial x}\frac{\partial v}{\partial y}\right) + \sqrt{Q}\right], \tau\left[\frac{1}{2}\left(\frac{\partial u}{\partial x}\frac{\partial v}{\partial y}\right) - \sqrt{Q}\right]\right] \tag{2.9}$$

The noisy Q criterion data was filtered using a Gaussian convolution filter Figure 2.19 with a standard deviation of $\sigma_{gauss} = 6pnts = 3.24mm$. The identified secondary vortex core structures can be visualized in Figure 2.20.

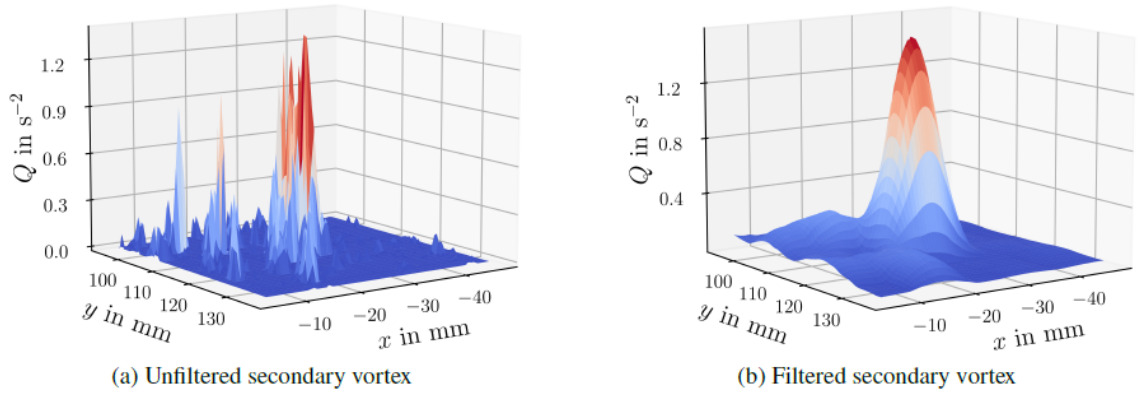

(a) Unfiltered secondary vortex

(b) Filtered secondary vortex

Figure 2.19: Q criterion of secondary vortex structures - filtered and unfiltered [24]

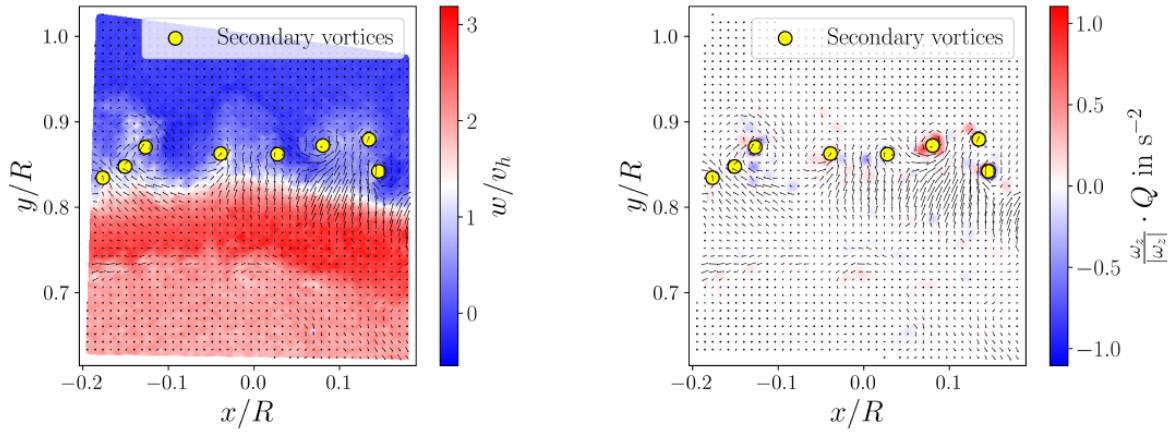

(a) Velocity component in z-direction and detected secondary structures

(b) In-plane vorticity and detected secondary structures

Figure 2.20: Detection of secondary vortex structures [24]

2.3. Research Objectives

It can thus be summarized that most of the available literature points out to the reduction of induced drag in the presence of slotted winglets/wing-tips, in the low speed regime. Additionally, there seems to be a diffusion of vortices with bio-mimicked wings, as compared to original bird wings. The evolutionary purpose of flexible wingtips is deemed to be for increasing $C_{L_{max}}$ and preventing wingtip stall at higher α through mitigation of the effective angle of attack.

The literature study presented in this chapter raises multiple questions. Most importantly, there seems to be a research gap related to the actual cost-benefit of using bio-inspired slotted winglets. There was very minimal mention

on how the slots affect the profile drag, and hence an important question is if the total drag is also getting reduced. KleinHeerenbrink's work [32] seems to address using the streamwise velocity component contour that each separated primary has its own drag wake indicating that vertical separation of the primaries does indeed have detrimental effects on the friction drag. However, they have not quantified the effect or provided an estimate of the resulting profile drag increase. Additionally, the question of this cost-benefit ratio of using slots in a human-made (i.e., bio-mimicked) wing is still murky. Especially, the effect of flexibility still seems to be unaddressed in terms to the drag reduction advantage the slotted winglets provide.

A novel approach in this thesis could be to investigate slotted winglets with the following research objective based on multiple research questions:

How much tip vortex mitigation is achievable through a bio-mimicked flexible and slotted winglets at low Reynolds numbers? How much is this sensitive to stiffness?

2.3.1. Drag reduction:

1. Do slots reduce induced drag and do flexible wingtips reduce it further?
2. Is this valid across a range of angles of attack?
3. Is the total drag also reduced (or) is the reduction is induced drag compensated by an increase in profile drag?
4. How sensitive is this phenomenon to Reynold's number in the low-speed regime?

2.3.2. Aerodynamic efficiency:

1. Does it improve the aerodynamic performance? How about flexibility?
2. Does flexibility in slotted wingtips improve $(C_L/C_D)_{max}$ by reducing the effective AOA?
3. Do slots only increase the total lift through an increase in surface area, or does it actually improve C_L?

2.3.3. Vortex characterization:

1. How does tip vortex breakdown & dissipation look like? Are the vortex cores distinct and notable?
2. Are the slots reducing the strength of the tip vortex?
3. Vortex wandering effect - how does the vortex core displacement look like?

3 Methodology

The required results for the thesis work were achieved through three distinct experimental campaigns. Firstly, motion tracking of the flexible wingtips was conducted alongside force balance measurements. The motion tracking data were used to reconstruct wingtip deformations, determine the average maximum deflection at various angles of attack and Reynolds numbers, and qualitatively correlate this deflection with vortex diffusion. This was followed by a $3C - 2D$ Stereo-PIV (Particle Image Velocimetry) test campaign, wherein multiple cross-flow planes were setup in the wake of the wing and the cross-plane velocities were used for the calculation of vortex parameters and the drag components subsection 3.2.3. The third and final experiment involved determining the flexural rigidity and Young's modulus of each winglet, which were then used to compare and quantify the performance of winglets with different flexibility.

All tests were conducted at the M-tunnel facility in the Low-Speed Laboratory at TU Delft. The tunnel was operated as an open-jet tunnel, although it can function as both an open or closed-jet tunnel. The test section of the tunnel measures $0.4m \times 0.4m$, and due to the large contraction ratio, the turbulence level in the test section is low. Under open-jet conditions, the tunnel can reach a maximum speed of $35m/s$.

The following chapter briefly describes the theoretical background and the work done to obtain the data required to answer the research questions mentioned in section 2.3.

3.1. Wind-tunnel models

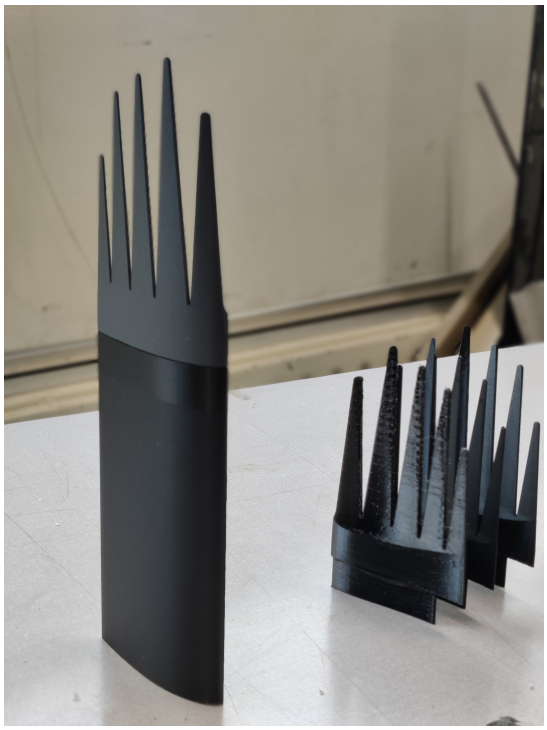

Figure 3.1: Wind-tunnel models

The set of wind-tunnel models consists of the following:

- 3 slotted winglets with different materials and thickness but otherwise similar geometry.

- 1 normal unslotted winglet with span and tip outline resembling that of the slotted winglets.
- 1 base wing

All the winglets and wing used for the experiments were designed and 3D modeled using the cloud-based CAD (Computer-Aided Design) software *Catia 3Dexperience*. Using the generated CAD models, the wing and winglets were 3D printed at the High Speed Laboratory of TU Delft Aerospace Engineering department.

3.1.1. Material

It was decided to go for three slotted winglets with varying stiffness for the experiments to evaluate the flexibility characteristics and its influence - one stiff, one flexible and one intermediate. The following properties were considered in order to chose materials for the winglets:

- Stiffness based on Young's modulus:
- Bending Strength
- 3D print-ability
- Availability of material

Multiple materials such a balsa wood, carbon fibre, PETG (Polyethylene Terephthalate Glycol), TPE (Thermoplastic Elastomers) and PBS (Polybutyene Succinate) were considered for the winglets. However, based on the above mentioned points, 3 plastic based materials - TPU (Thermoplastic Polyurethane), PLA (Polylactic Acid) and cPLA (carbon-infused PLA) were chosen for each of the wing and winglets. The material allotment for each of the wing/winglet is displayed in Table 3.1 and the Young's modulus of each of the material is shown in Table 3.2 (Refer chapter 6 for more information).

Model	Material	Abbreviation	Wingtip flexibility	3D-printability (1-10)
Slotted Winglet 1	Thermoplastic Polyurethane	TPU	Flexible	6
Slotted Winglet 2	Polylactic Acid	PLA	Intermediate	8
Slotted Winglet 3	carbon-infused PLA	cPLA	Rigid	9
Normal Winglet	Polylactic Acid	PLA	-	10
Base Wing	Polylactic Acid	PLA	-	10

Table 3.1: Material Allotment

Material	Abbreviation	Young's Modulus (E)
TPU	Thermoplastic Polyurethane	56 ± 3 MPa
PLA	Polylactic Acid	3071 ± 181 MPa
cPLA	Carbon-infused PLA	2420 ± 120 MPa
	Bird feathers (Owl & Pigeon [4])	6000-8000 Mpa

Table 3.2: Material Young's Moduli

3.1.2. Geometry

Since the study was mainly focused on bio-mimicking the wingtips of an average bird's wingtips, numerous airfoils and winglet geometries were considered for the models. The primary consideration for the tip outline was to bio-mimic the outer primaries of a generic bird such as a crow wing during a soaring flight as shown in Figure 3.2. Note that the individual feathers at the wingtips of a bird flex greatly to create wider slots. The designed CAD model of such a slotted winglet along with a regular non-slotted winglet can be seen in Figure 3.3a & Figure 3.3b, along with the sketched tip outline with dimensions in Figure 3.3c. The geometric parameters are quantified in Table 3.3.

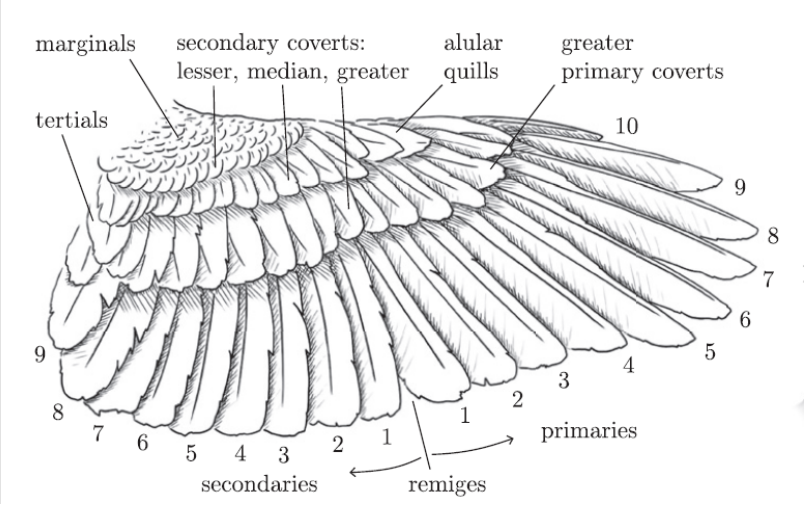

Figure 3.2: Feather morphology and wing outline (dorsal) of an adult American crow [31]

Parameter	Symbol	Value
Total semi-span	b_{tot}	$0.29m$
Aspect ratio	AR	3.36
Base wing & winglet taper	λ	1
Total Wing Area	S	$\approx 0.02m^2$
Base airfoil	-	S1223

Table 3.3: Wing characteristics

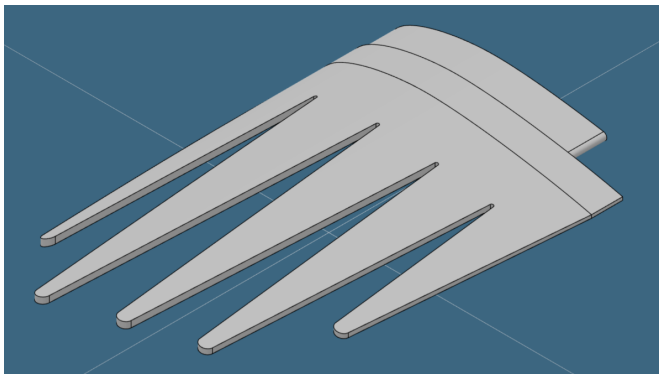

(a) CAD model of a slotted winglet

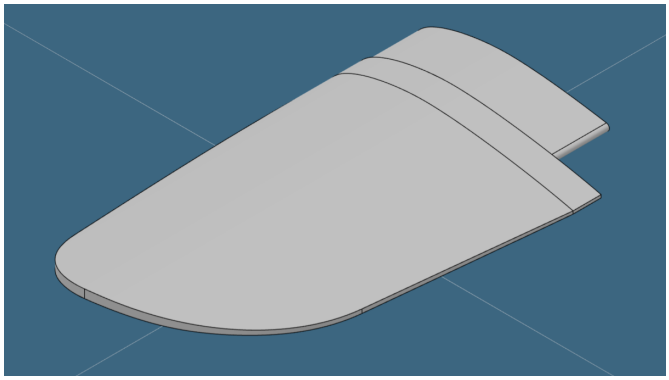

(b) CAD model of a normal winglet

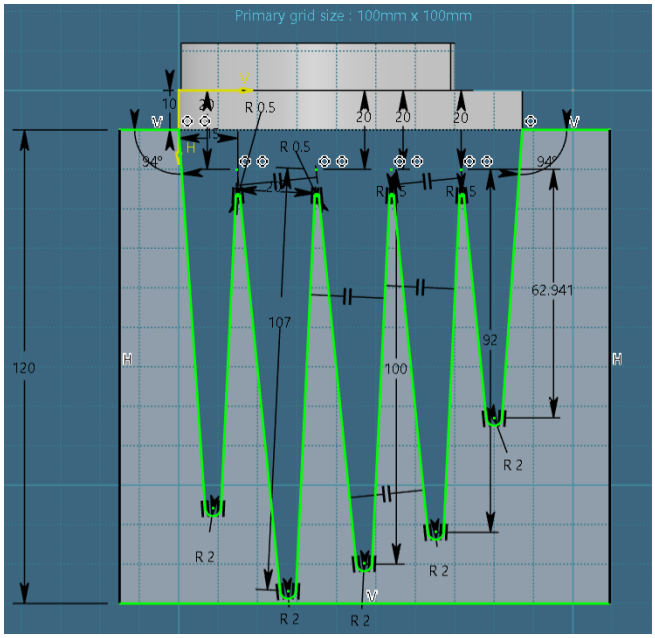

(c) Sketch of the Wingtip Slots

A soaring bird's wing is very similar to a highly cambered, low Reynolds number airfoil [31]. After literature review, the choices were narrowed down to two unique airfoils - *goe 174* (albatross wing [41]) and *Selig S1223* [31]. Comparing the C_L/C_D and $C_L\alpha$ plots[1] at low Re, it was inferred that the *S1223* airfoil had a more predictable behaviour across a range of α than the *goe 174* . Hence, it was decided to go for the Selig $S1223$ airfoil with the following characteristics:

Parameter	Chordwise location (%)	Value
Max t/c	19.8	12.1 %
Max camber	49	8.1 %
Chord	-	87.113 mm

Table 3.4: Airfoil characteristics

The trailing edge of the airfoil was modified to a thickness of $1mm$ for compatibility with the 3D-printer, as can be seen in Figure 3.4.

[1] Airfoil Tools

Figure 3.4: S1223 airfoil with modified TE

3.2. Theoretical Background

3.2.1. Aeroelastic parameters

Now that the materials for the winglet were chosen based on the Young's modulus, the next step would be to find out non-dimensional parameters to characterize the flexibility of the designed winglet models under aerodynamic loads, considering both material and geometry. During a work on the effects of flexibility and aspect ratio on the aerodynamic performance of flapping insect wings, Junjiang Fu *et al.* used various non-dimensionless parameters for comparing their models including Flexural stiffness $EI(Nm^2)$ and Effective stiffness denoted by Π_1, obtained from [48]:

$$\Pi_1 = \frac{Et_w^3}{12(1-\nu^2)\rho_f U_{ref}^2 c^3} \tag{3.1}$$

where t_w is the thickness of the wing, ρ_f is the fluid density, c is the mean aerodynamic chord and ν is the poisson's ratio. This is a measure of the ratio between elastic bending and aerodynamic (or fluid dynamic) forces.

Previously, Combe [13] calculated the local flexural stiffness for his/her study on insect wing stiffness. He treated each wing as heterogeneous, 2D beam in the spanwise (or chordwise) direction and used a continuous beam equation to estimate the stiffness along this axis. With the beam attached at one side and point force applied at the other end (i.e., a tip-loaded cantilever beam) flexural stiffness at any point along the beam is the moment at that position divided by the local curvature (or the 2^{nd} derivative of displacement):

$$EI(z) = \frac{M(z)}{d^2w/dz^2} \tag{3.2}$$

$$\implies EI(z) = \frac{F(L-z)}{d^2w/dz^2} \tag{3.3}$$

Where F is the applied load and L is the total length of the beam.

Very recently, Alden Midmer *et al.* [39] used the non-dimensional parameter Cauchy number C_y to represent flexibility of wingtips under a fluid load in his/her work on the Vortex dynamics of bio-inspired flexible slotted winglets. Based on the work of [27], Cauchy number is the ratio between the inertial force to the elastic force of the structure:

$$C_y = \frac{\rho_w U^2 C_L W L^3}{2EI} \tag{3.4}$$

where W represents the geometry of the wingtip (i.e., thickness), ρ_w represents the density of the wingtip. The wingtips can be seen in Figure 3.5. The Cauchy number of the wingtips were matched with that of the outer 25% of a primary feather of the *Peregrine Falcon* bird under study.

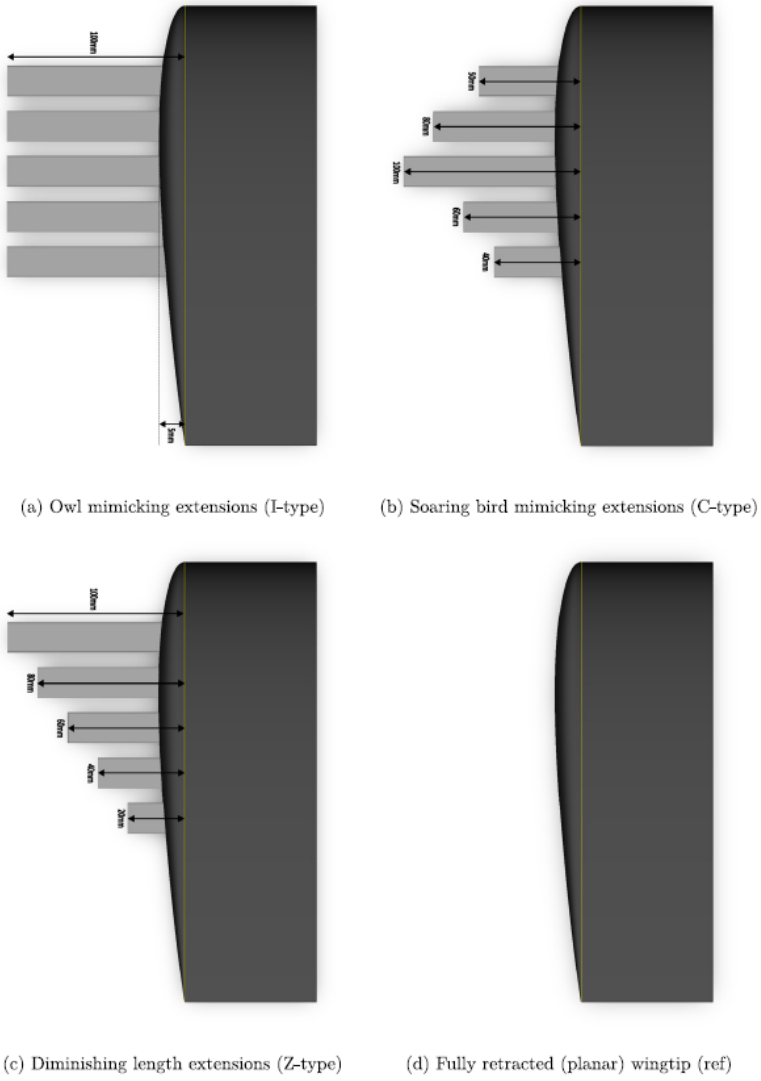

(a) Owl mimicking extensions (I-type)

(b) Soaring bird mimicking extensions (C-type)

(c) Diminishing length extensions (Z-type)

(d) Fully retracted (planar) wingtip (ref)

Figure 3.5: Wingtip Configurations of [39]

It was finalised to use the flexural stiffness or rigidity (EI) for the current thesis, as it can be easily estimated from a simple bending test and as it is comprehensive of both material and geometric properties.

3.2.2. Wingtip bending

The wingtips of the slotted winglet have been considered as simple tapered cantilever beams with uniformly varying width and constant thickness. The bending equation of a simple cantilever beam with constant thickness and a point load at the end is given by:

$$EI(z)\frac{d^2w}{dz^2} = M = P(L-z) \qquad BCs: \quad \frac{dw}{dz}|_{z=0} = 0; \quad w(z)|_{z=0} = 0 \tag{3.5}$$

Where w is the deflection in y direction at each z location along the tip. Note that y is the normal direction to the winglet (refer Figure 3.8b), M is the moment, P is the pointwise load and L is the length of the beam. It has been assumed that the second moment of inertia I varies linearly with the spanwise location z, since the width varies linearly, and can be expressed as:

$$I(z) = I_0(1 - \frac{z}{L}) \tag{3.6}$$

Where I_0 is the 2^{nd} moment of inertia at the root ($z = 0$). Therefore Equation 3.5 becomes:

$$\frac{d^2w(z)}{dy} = \frac{P(L-z)}{E\left[I_0(1-\frac{z}{L})\right]} \tag{3.7}$$

Integrating the above equation twice:

$$w(z) = \int_0^z \int_0^z \frac{P(L-z)}{E\left[I_0(1-\frac{z}{L})\right]} dy = \frac{PL}{E.I_0}\frac{z^2}{2} \tag{3.8}$$

Evaluating $w(z)$ at the tip $(z = L)$, we can obtain:

$$w(L) = \frac{PL^3}{2E.I_0} \tag{3.9}$$

Note that the cross-section of the beam (i.e., wingtip) is a rectangle. In order to find the Young's modulus of each of the winglet material, the second moment of inertia at the root I_0 for a constant thickness h and root width b_0 has been estimated as:

$$I_0 = \frac{x_0 h^3}{12} \tag{3.10}$$

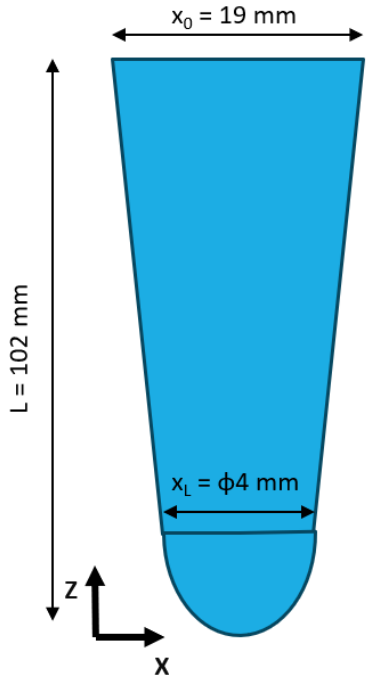

Figure 3.6: Dimensions of the longest wingtip

3.2.3. Drag Estimation

Jumping from the structural aspect back to aerodynamics, one of the highlighting elements of the thesis is the estimation of different components of drag. The subsonic drag of a finite lifting system can be resolved, at high Reynold's numbers, into two essentially distinct components - profile and vortex drags. The difference between both the components lies inherently in the physical phenomenon behind them - one corresponds to the energy losses in the fluid entrained into the boundary layers and wake of the lifting system, and the other to the energy required to maintain the large scale and predominantly inviscid secondary flow generated in association with the shedding of trailing vorticity [37]. The total drag can thus be decomposed as follows:

$$D_{total} = D_{induced} + D_{profile} \tag{3.11}$$

$D_{induced}$ represents the lift or vortex induced drag as mentioned in chapter 1. The profile drag $D_{profile}$ is usually seen as the combination of the pressure, wave and viscous drag.

The most widely used tool to estimate the aerodynamic forces in wind tunnels is the force balance. However, these force balances are typically strain-gauges and are only good at measuring the lift which is often one magnitude higher than the drag force. Additionally, there is no possibility of measuring the various components of drag. This has turned the focus to numerical drag estimation methods such as the widely used Trefftz Plane analysis in the AVL (Athena Vortex-Lattice [2]) software and in similar wake integration approaches based on control volume formulation.

The earliest work in this field dates back to 1925 by Betz [6], who used the momentum deficit integral formulation and modified it to accommodate the presence of wind tunnel walls and reduced the area of integration to the region directly behind the model [22]. Their theory was extended into including the measurement of both profile and vortex drag by Maskell in 1973 [37].

The wake integration methods originate from a simple control volume formulation. The net aerodynamic force F of an aircraft wing can be expressed as a surface integral enclosing the aircraft of the sum of the pressure and viscous forces and the momentum deficit over any control volume as follows:

$$\vec{F} = \int_S (-p\vec{n} - \rho(\vec{u}\cdot\vec{n})\vec{u} + \vec{\tau}\cdot\vec{n})dS \tag{3.12}$$

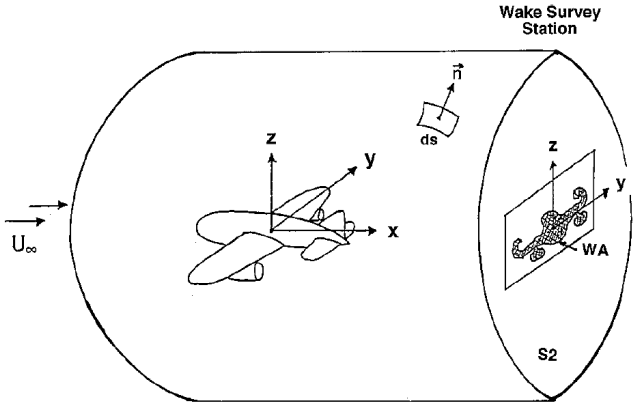

Figure 3.7: Control Volume configuration with wake survey station[34]

The control volume is taken to be a cube aligned with the (x,y,z) axes and with the far-field face a fixed distance downstream of the aircraft referred to as *Wake survey station*, as shown in Figure 3.7. Giles [22] in his paper on 3D flowfield wake integration had mentioned that as the size of the cube increases, the contribution to the drag component of the integral from the other five faces tends to zero. If the control volume surface is sufficiently far from the aircraft, the viscous stress terms may be neglected, and the final expression for the drag force as mentioned by Giles [22]is:

$$D = -\iint_S [p - p_\infty + \rho u(u - U_\infty)dydz \tag{3.13}$$

However, as previously mentioned, in order to adapt the numerical model to the wind tunnel testing environment, Betz had proposed a velocity u' corresponding to the flow producing drag which is identical to the flow outside the vortical region (i.e., outside the wake region). This implies that outside of the vortical region, $u' = u$ but $u' > u$ inside the vortical region and is given by [3]:

[2] https://web.mit.edu/drela/Public/web/avl/

[3] ∞ indicates freestream value

$$p_\infty = p + \frac{1}{2}\rho(u'^2 + v^2 + w^2) \tag{3.14}$$

And the drag components can be derived as follows [9]:

$$D_{profile} = \iint_S [p_{t_\infty} - p_t + \frac{\rho}{2}(u' - U_\infty)(u' + u - 2U_\infty]dS \tag{3.15}$$

$$D_{induced} = \frac{\rho}{2}\iint_S \rho(v^2 + w^2 - u'^2)dS \tag{3.16}$$

Brunes [9] had quoted that the elimination of the u' term was perhaps the most questionable aspect of Maskell''s theory since the distinction between the vortex drag and induced drag disappears. Maskell neglected u', and expressed the induced drag integral with cross-flow plane velocities in terms of stream function and streamwise vorticity as follows:

$$D_{ind} = \frac{\rho}{2}\iint_S \psi\omega_x dS \qquad where: \ \nabla^2\psi = -\omega_x \tag{3.17}$$

The pressure field is generally not available in a PIV experiment, and basically two approaches can be followed to amend this [3]. The first is to use a formulation of the control-volume approach from which the pressure has been eliminated ([42]). The second is to explicitly evaluate the pressure ([52]) using the momentum equation.

In the present thesis, the second approach is utilized and the profile drag component was evaluated using a simple momentum-based approach and it was assumed that the the mid plane 2 and far-field plane 3 are in a potential flow region where the static pressure in the plane has reached the freestream value ($p = p_\infty$). This indeed resulted in errors, as will be discussed in subsection 4.4.3, however the resulting data was sufficient to quantify the drag performance of the winglets. The vortex-induced drag was formulated based on the cross-flow plane velocities obtained from the PIV experiment, following Gile's [22] work based on Maskell's approach without the velocity u'. The final equations for the drag and its components are as follows:

$$D_{tot} = \underbrace{\iint_S \rho u(U_\infty - u)dS + \iint_S \cancelto{0}{(p_\infty - p)dS}}_{\text{Profile drag}} + \underbrace{\frac{1}{2}\iint_S \rho(v^2 + w^2)dS}_{\text{Induced drag}} \tag{3.18}$$

Note that there lies an assumption of the plane being located sufficiently downstream where the flow is invariant in the x-direction. The double integrals were approximated for the PIV cross-flow plane grid of size (N_y, N_z) and cell size $(\Delta y, \Delta z)$ as follows:

$$D_{ind} = \frac{1}{2}\iint_S \rho(v^2 + w^2)dS = \frac{1}{2}\rho\Delta y\Delta z \sum_{i=0,j=0}^{(N_y,N_z)} (v_{ij}^2 + w_{ij}^2) \tag{3.19}$$

$$D_{prof} = \iint_S \rho u(U_\infty - u)dS = \rho\Delta y\Delta z \sum_{i=0,j=0}^{(N_y,N_z)} u_{ij}(U_\infty - u_{ij}) \tag{3.20}$$

The simplest physical interpretation of the induced drag equation is that the moving aircraft is doing work on the surrounding air at the rate $D \times U_\infty$, which, in its wake, must equal the rate at which it is leaving kinetic energy associated with the crossflow [22].

3.3. Experimental Setup

The wing-winglet model mounted on top of the mounting table can be seen in Figure 3.8b. The wing was attached to the table through a rod that approximately passes through the quarter-chord point and covers the entire span of the wing. A simple printed protractor pivoted at the quarter chord location was used to measure the angle of attack.

(a) Wing mounting in the experiment; with attached transition strips and tufts

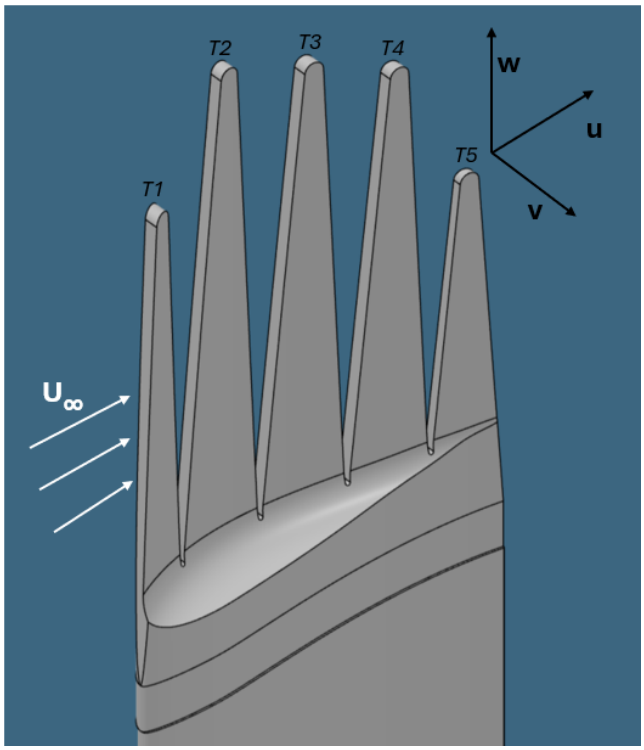

(b) Wing CAD model with reference axes and tip numbering

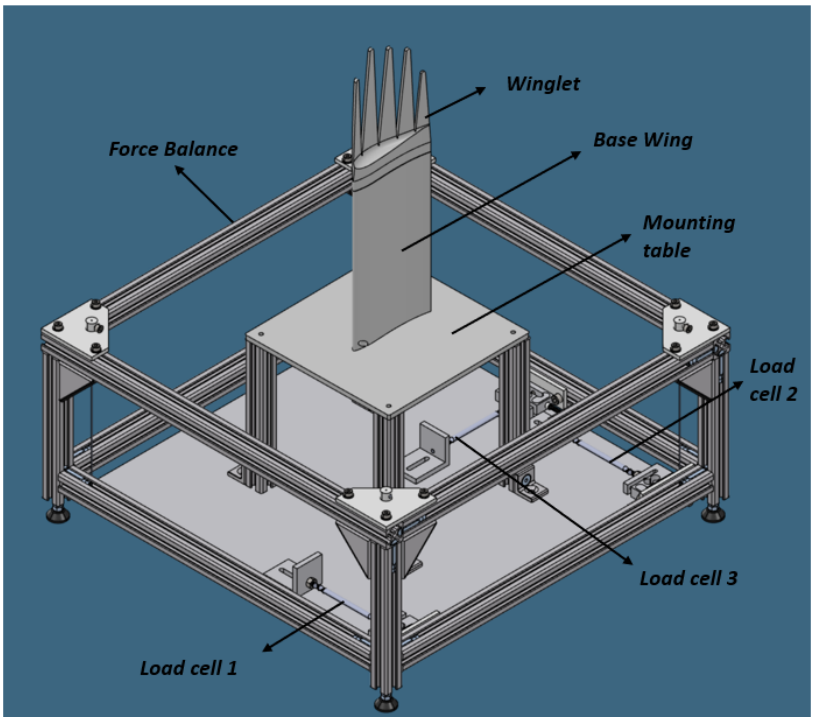

Figure 3.9: Complete CAD model with mounting table and force balance

3.3.1. Wingtip bending (Stiffness test)

The apparatus used to perform the stiffness or bending test can be seen in Figure 3.10. The measurements were taken using a vertical gauge with a high level of accuracy. The weights shown in the picture were attached through through a weightless thread and hung down from the tip of the longest wingtip $T2$ of the winglet. A vertical gauge was used to read the magnitude of displacement of the tip. The deflection at the tip $w(L)$ was measured during the experiment using two different weights and was repeated multiple times to improve precision and accuracy. The thickness of the 3D-printed wingtips were measured using a vernier caliper, and was found to have slightly different thickness from the CAD model. All the readings (Δy) and their the root-mean-square values (z_{rms}), along with the

standard deviation of the readings (σ_y) have been mentioned in Table 3.5. The bending of the wingtip is modelled as a second order differential equation as given in Equation 3.5. However, only the deflection in the y direction (normal to winglet) is required for estimating EI_0. Although EI could be estimated at the tip using the value at the root, it decided to use EI_0 directly, as we only require a comparison between the flexural rigidity of the different winglets.

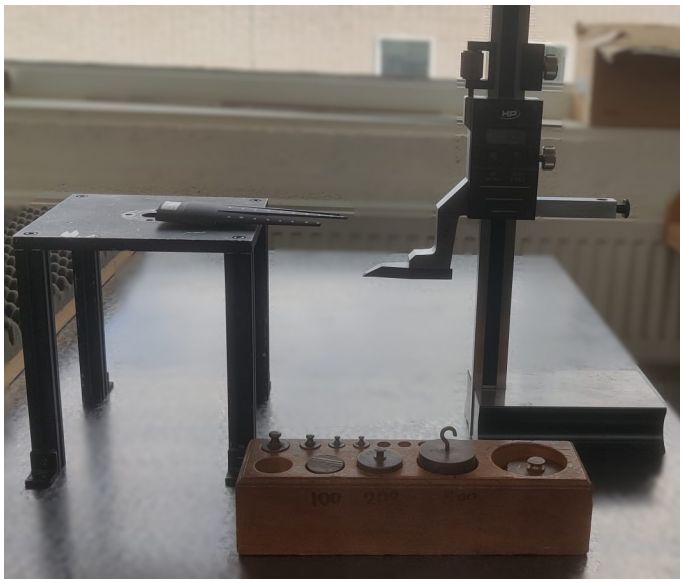

Figure 3.10: Stiffness test apparatus

The results from the experiment have been tabulated in Table 3.6. The EI_0 results from using a $10g$ weight and $20g$ weight have been averaged, I_0 was calculated using Equation 3.10, and E was calculated with these values. It can be seen that the calculated Young's modulus E compares well with the values from the technical data sheets of the 3D printing materials.

Mass (g)	Winglet	Readings - $\Delta y(mm)$										$h(mm)$	Δy_{rms} (mm)	$\sigma_y(mm)$
		1	2	3	4	5	6	7	8	9	10			
10	PLA	11.14	11.29	11.45	11.42	11.5	11.49	11.43	11.55	11.5	11.33	1.07	11.41	0.12
10	cPLA	1.66	1.63	1.59	1.62	1.55	1.96	1.81	1.66	1.83	1.7	2.07	1.70	0.12
10	TPU	34.84	37.63	37.45	37.82	37.80	37.43	37.98	37.85	37.49	37.86	2.8	37.42	0.88
20	PLA	21.82	22.02	21.72	21.8	22.12	22.09	22.13	22.22	22.16	22.21	1.07	22.03	0.17
20	cPLA	3.29	3.57	3.4	3.49	3.43	3.37	3.25	3.48	3.36	3.46	2.07	3.41	0.09
20	TPU	50.82	52.02	52.99	52.79	52.85	52.71	52.28	52.69	52.08	52.44	2.8	52.37	0.60

Table 3.5: Stiffness test readings

Winglet	$EI_0(Nm^2)$	$I_0(m^4)$	$E_{calc}(MPa)$	$E_{data}(MPa)$
PLA	4.66×10^{-03}	1.94×10^{-12}	2399.29	$2890 - 3252$
cPLA	3.06×10^{-02}	1.40×10^{-11}	2190.69	$2320 - 2540$
TPU	1.70×10^{-03}	3.48×10^{-11}	48.71	$53 - 59$

Table 3.6: Stiffness test results

The standard deviation values for the readings have been mentioned in the last column Table 3.5, indicating a small amount of uncertainty. The readings were indeed taken for different weights to reduce the random errors. It could be noticed that the standard deviation increased as the flexibility of the material and hence the deflection Δy increased. This primarily because the vertical gauge was adjusted manually with naked eye to measure the displacements. As can be seen the standard deviation is the highest for TPU with a standard weight of mass of $10g$, at $0.88mm$.

3.3.2. Motion Tracking & Force balance measurements

As mentioned in the beginning of the chapter, the motion tracking and the force balance measurements were done together in the same experiment. As shown in Figure 3.11, the wing-winglet model was mounted on a force balance built in-house. A mounting table designed specifically for the force balance was utilized. The wing-winglet model was placed with its chord aligned with the freestream, and its base just within the lower wall of the tunnel.

The force balance was built in-house as mentioned, and was made up of three load cells. The balance was positioned such that two of the load cells represented the lift readings (summed up) and one represented the drag force. The acquisition was made through a DAC (Digital Analog Converter) connected to the PC. The system had an acquisition rate of 25 KHz, and the readings were averaged out over a period of 10 seconds. The readings were zeroed out after any setup changes before acquisition, in order to subtract the weight of the mounting table. Additionally, the empty table measurements of lift and drag (normalized; in the form of C_L and C_D) were subtracted from the readings. However, no further boundary corrections were applied.

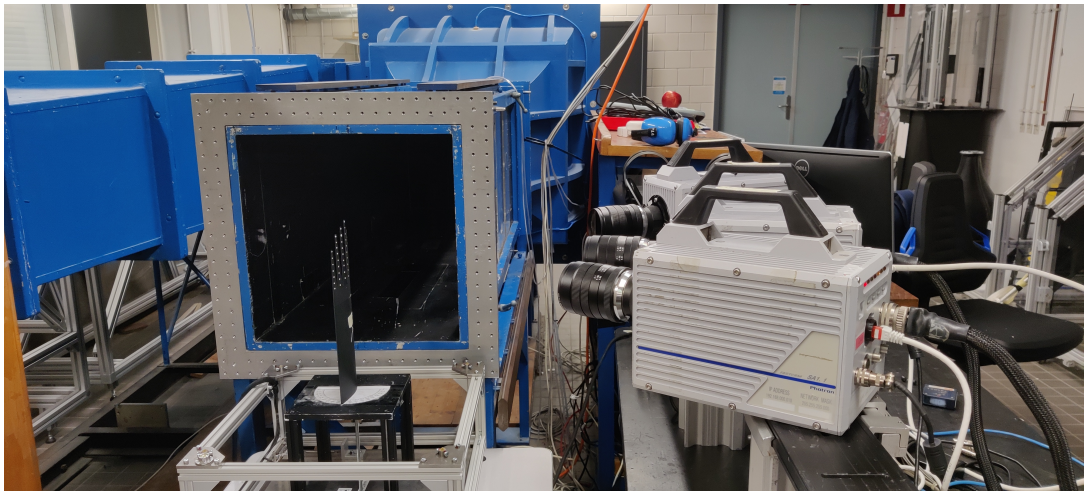

Figure 3.11: Setup for motion tracking experiment

The working behind motion tracking is simple - markers were drawn by hand on the wingtips as shown in Figure 3.12, and the deformations of the wingtips are traced using the image recognition of these markers. Three *Photron Fastcam SA1.1* high speed cameras were used to record the images over a timespan of 10s. As can be seen in Figure 3.11, the cameras were mounted on a beam raised to obtain the required field of view *(fov)* of the winglet, which was approximately kept at $2c \times 1.5c$ or $174mm \times 131mm$. The cameras had a resolution of $1024 \times 1024\, pixels$ at $5400fps$ and the zoom rate was kept at 40 %. The frame rate was however kept at $50fps$ since the high frequency oscillation of the wingtips was moreover absent and to avoid an extra lighting source. The aperture of the 3 cameras were mostly kept at $f^{\#} = 5.6$, however was varied for certain cases to adjust the amount of background lighting. For each of the camera, a Laowa $f60mm$ lens was used.

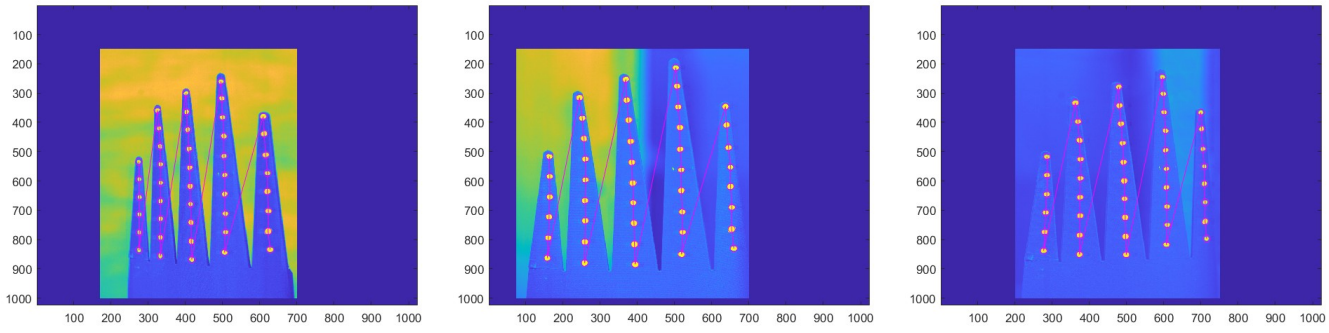

Figure 3.12: Marker recognition in motion tracking experiment using three cameras - a) Camera 1 b) Camera 2 c) Camera 3

The recording was done using the software Photron FASTCAM Viewer (PFV v3), with an acquisition speed of $30fps$ and an ensemble size of 500 images. Each measurement thus had $3 \times 500 = 1500$ images. All three cameras were synchronized within the Photron software. These images were calibrated and processed using an in-house developed Matlab script to detect the markers (refer Figure 3.12) and trace the positions of each individual marker over the 10s timespan. The script had an algorithm based on image processing tools from Matlab. It basically consists of two steps:

1. The markers were recognized based on using a filter on the light intensity of each of the pixel and picking out the highest intensities to be the marker dots. This is achieved through masking the winglet from the background

and through normalizing the intensities to find the peaks. The pixel coordinates of these marker dots were then sorted and aligned based on the wingtip number and the location within the wingtip. The pixel coordinates are then saved to a .mat file.

2. The extracted pixel coordinates were then converted into Cartesian coordinates in real-world using calibration data. The calibration data was obtained through a pin-hole calibration algorithm in *LaVision Davis*, which involves the usage multiple images of a calibration target in different alignments as shown in Figure 3.13.

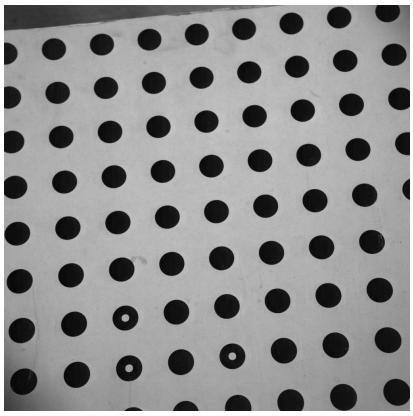

Figure 3.13: Motion tracking - Pinhole Calibration target

3.3.3. PIV

Particle image velocimetry (PIV) is an optical flow diagnostics tool based on the scattering of particles subject to a light source [54]. The fluid motion is made visible by adding small tracer particles and from the positions of these tracer particles at two instances of time, i.e. the particle displacement, it is possible to infer the flow velocity field. The experimental set-up of a PIV system typically consists of several subsystems [44].

- **Tracer particle addition:** Particles such as smoke which are good in tracking the flow and can scatter light are added into the wind tunnel flow.
- **Particle Illumination** The tracer particles are illuminated by laser at atleast two consecutive time instances.
- **Recording and Calibration:** The tracer particles are captured throught the light they scatter, and are recorded as images at consecutive time instances. They are then calibrated to correlate the displacement of the particle in the image planes to the actual displacement of the particle in the flow between the two time instances.
- **Cross-correlation:** The displacement of the particle images is estimated using a statistical approach called cross-correlation (refer Figure 3.15a).
- **Post-Processing:** Filtering out the abnormal correlation values, and several other refinement process is carried out in this step to make the data more accurate.

In the present thesis, a 2D-3C stereoscopic PIV system was utilized, which unlike a simple planar PIV measures the out-of-plane velocity component using an additional camera.

Basic working:

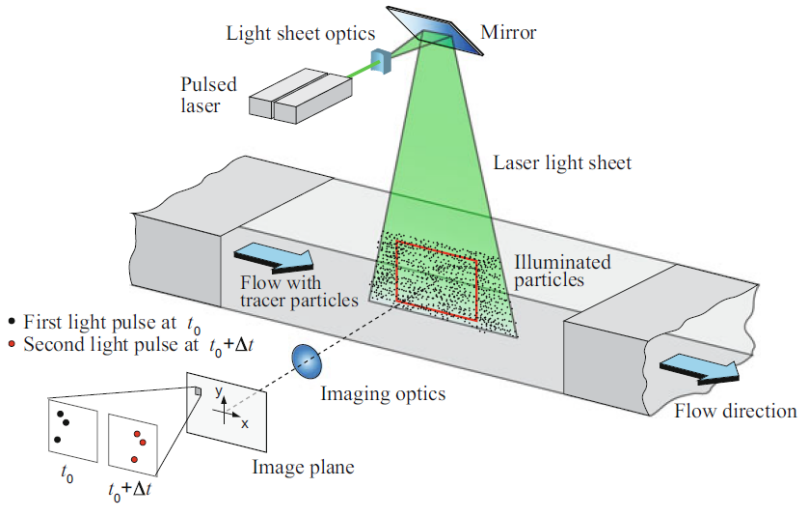

Figure 3.14: Setup for planar 2C-2D PIV with laser sheet [44]

Figure 3.14 briefly sketches a typical set-up for a planar PIV recording of two velocity components within the flow field in a plane in a wind tunnel (2C-2D PIV). At a point where they won't interfere with the flow of interest, small tracer particles are added to the flow. The plane of interest inside the flow is twice illuminated by a laser light sheet. The imaging magnification and flow velocity must be taken into consideration while choosing the time delay between the pulses. The tracer particles are thought to travel between the two illuminations at the local flow velocity. The light scattered by the tracer particles is captured by a high-quality lens onto two different frames of a cross-correlation digital camera. The output of the digital sensor is loaded into the memory of a computer. The digital PIV recording is segmented into tiny subareas known as "interrogation areas" for examination. Statistical techniques (cross-correlation) are used to compute the local displacement vector for each interrogation area for the images of the tracer particles from the first and second illumination. Taking into account the interval between illuminations and imaging system calibration, the projection of the local flow velocity vector (two-component velocity vector) into the plane of the light sheet is computed. All of the PIV recording's questioning zones undergo this review again.

Cross-correlation is perhaps the most crucial aspect of the PIV post-processing phase. The image is first divided into multiple interrogation windows as shown in Figure 3.15a. A cross-correlation map is generated for each interrogation window by comparing of the interrogation windows of the first image taken at a time t with each of the interrogation windows of the second image taken at a time interval of $t + \Delta t$. The cross correlation values in the map indicates the degree of matching of the particle intensity distributions of the two windows, and the peaks are calculated by using a Fourier Transform to convert the time-domain data into frequency domain. The position of the highest correlation peak (shown in Figure 3.15b) indicates the average particle image displacement. The normalized cross-correlation function is given by [44]:

$$R(x,y) = \frac{\sum_{i=1}^{I}\sum_{j=1}^{J} I(i,j)I'(i+x,j+y)}{\sigma\sigma'(x,y)} \tag{3.21}$$

where I is the first image and I' is the second image. (x,y) represents the position of the second image, while σ and σ' are the standard deviations of the first and second image pixel displacements respectively, defined as follows:

$$\sigma = \sqrt{\sum_{i=1}^{I}\sum_{j=1}^{J}[I(i,j)-\mu_I]^2} \tag{3.22}$$

$$\sigma'(x,y) = \sqrt{\sum_{i=1}^{I}\sum_{j=1}^{J}[I'(i,j)-\mu_{I'}(x,y)]^2} \tag{3.23}$$

The value μ_I is the average of the image intensities and is computed only once while $\mu_{I'}(x,y)$ is the average of I' coincident with I at position (x,y) [44].

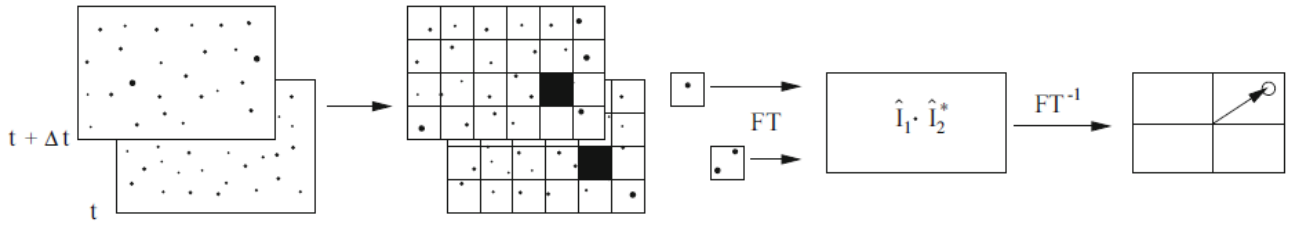

(a) Process of cross-correlation

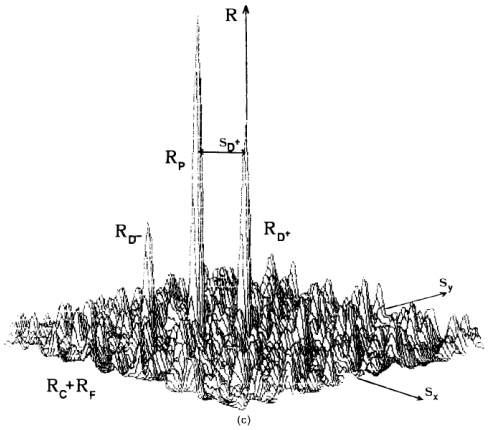

(b) Cross-correlation function R for double-exposure frames

Figure 3.15: Cross-correlation [30]

A stereoscopic PIV is an extension of the planar PIV method,wherein the measurement of the third velocity component (out-of-plane) is made possible using multiple cameras. Reconstruction of the three-component velocity vector in effect relies on the perspective distortion of a displacement vector viewed from different directions [44]. There are two different stereoscopic recording arrangement know as translation method and angular displacement technique with titled back plane. The second method was utilized in this thesis, which is based on the Scheimpflug criterion. The technique will be briefed upon later in this section.

Setup

The equipment used for the stereo-PIV experiment are given below,and the setup is shown in Figure 3.16. Post-processing was done using the software *LaVision Davis FlowMaster*, and additionally using *Matlab*.

- Quantec Evergreen 200 III laser
- Safex Twin Fog Double power smoke generator
- Lavision sCMOS 1
- Lavision sCMOS 2
- PTU X synchronizer
- Acquisition PC
- Scheimpflug adapters and optic lenses

The two sCMOS cameras used provided a good spacial resolution, however, the images were not temporally resolved. They are 16-bit, double shutter ($120ns$), low-speed cameras capable of acquiring images up to a frequency of $50Hz$. The camera has a sensor size of $2560 \times 2160pixels$ and a pixel pitch of $6.5\mu m$. The field of view was approximately $111 \times 123mm^2$. The camera lens used were of focal length $f = 60mm$. The two cameras and the laser were synchronized using a PTU-X synchronizer (Programmable Timing Unit). Both the cameras were mounted at the same side of the laser sheet roughly at an angle of $\theta \approx 30 - 35°$, although $\theta = 45°$ is said to be ideal. This is because of two reasons [19]:

- The software DaVis computes vectors in a virtual interrogation window in the world coordinate system which is mapped to the raw images to get the corresponding pixels. So the interrogation windows in the world coordinate system (system of final vector field) are compressed in the raw images of camera 1 and camera 2 and hence there are less pixels available for computing the velocity vectors in x direction. This increases the error by a factor of $1/\sqrt{cos\theta}$.

- The other effect more difficult to quantify is the error originating from both camera viewing not the same interrogation volume given an extended light sheet thickness. When there are gradients of the velocity in z-direction in combination with in-plane gradients the errors may become as large as 10% to 50% depending on the light sheet thickness. The error gets larger for larger camera angles.

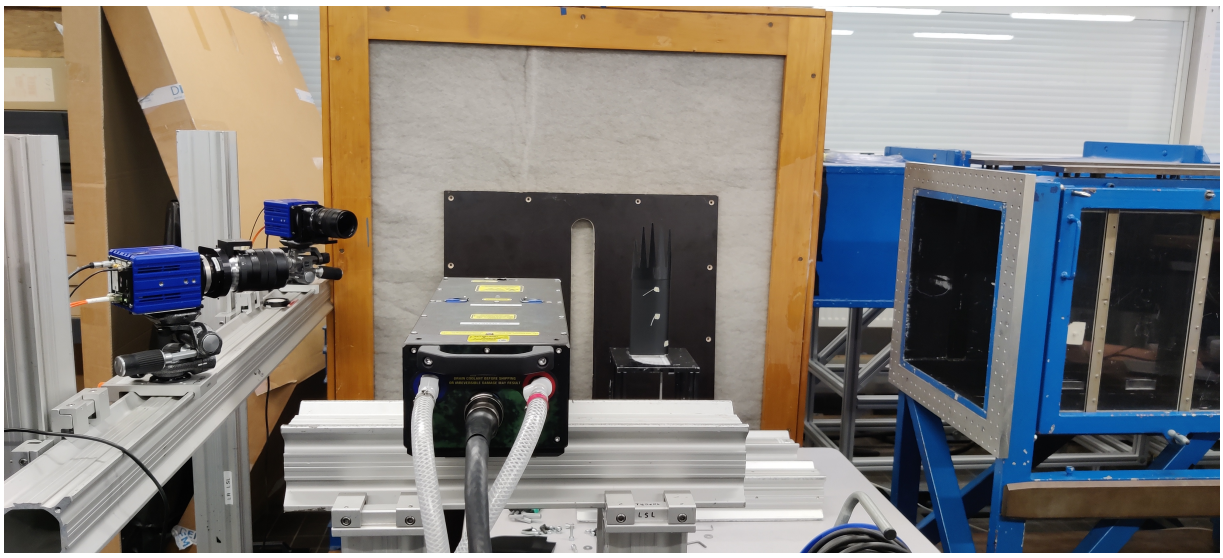

Figure 3.16: Setup for the $stereo - PIV$ experiment

The measurement precision for in-plane and out-of-plane components is similar if the angle between viewing directions is $90°$. One problem of an oblique viewing direction is the limited depth of field, which can be accommodated by additionally tilting the image plane in respect to the orientation of the camera lens and light sheet according to Figure 3.17b. A *Scheimpflug adapter* was attached to the camera lens and adjusted in order to do so and achieve the best possible field depth by aligning the image plane, lens plane and object plane for each of the cameras intersect in a common line as shown in Figure 3.17b.

Additionally, both the cameras were kept at a different aperture with one at $f/5.6$ and the other at $f/16$. This was in order to accommodate for *backward forward scattering* [19] as shown in Figure 3.17a.In this instance, the two cameras are situated on the same side of the laser sheet. The intensities detected with both cameras with the same focal length of the camera lens are different (usually a factor of 10 between backward and forward direction), so the camera viewing in the backward scattering direction typically needs a larger aperture [19]. This is because one camera is recording the light scattered in forward direction, while the second camera is recording the scattered light in backward direction.

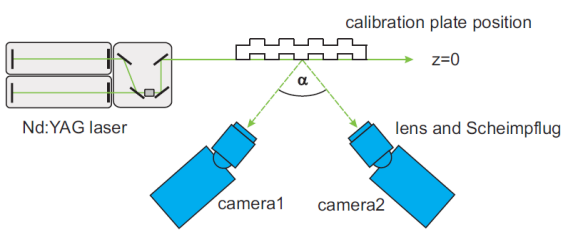

(a) Camera alignment

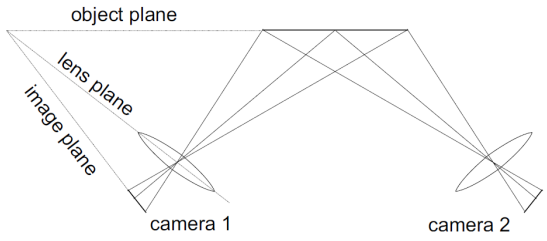

(b) Scheimpflug criterion

The Quantec Evergreen $200mJ$ laser generator was utilized that emits a double-pulsed green laser at a wavelength of $532nm$ and a pulse repetition rate of $15Hz$. The laser sheet was expanded into a plane using appropriate combination of convex and concave lenses, and the thickness was kept at a nominal value of $5mm$, abiding to the $(1/4)^{th}$ rule. This thickness was sufficient to capture the out-of-plane velocity component using suitable time steps - $\Delta t = 100\mu s$ for $U_\infty = 5m/s$, $\Delta t = 50\mu s$ for $U_\infty = 10m/s$ and $\Delta t = 33\mu s$ for $U_\infty = 15m/s$. The Laser sheet was fixed and the model was placed on a traverse to capture different cross-flow planes in the wake. The three different downstream locations thus generated are depicted in Figure 3.18.

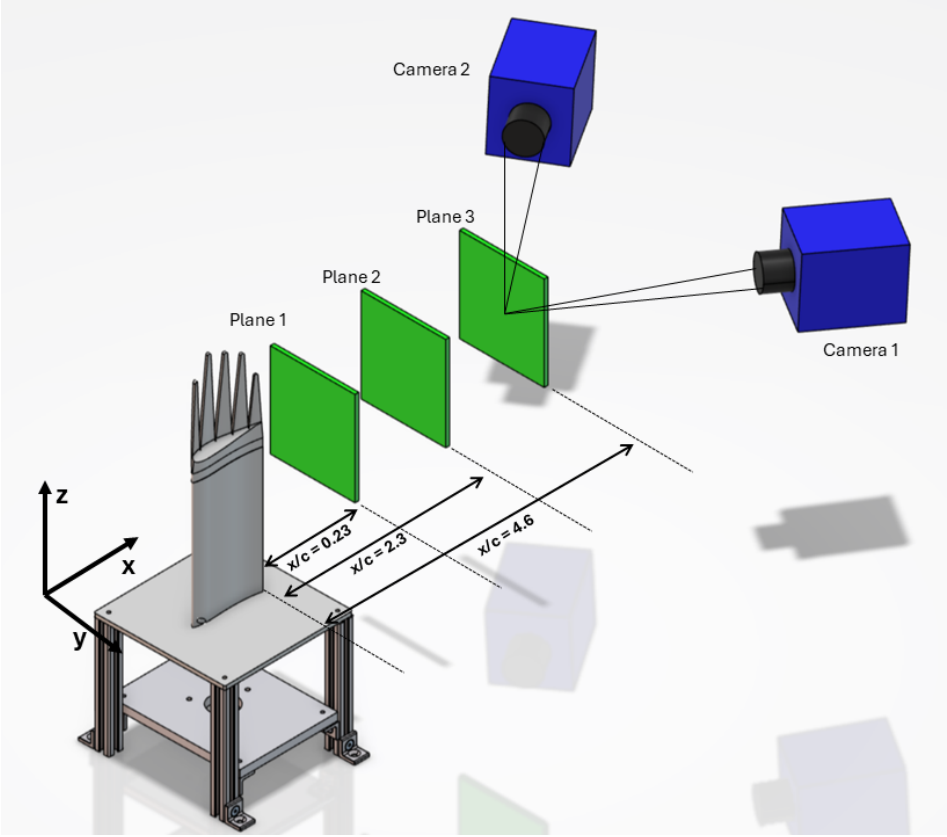

Figure 3.18: Location of the cross-flow planes

Finally, the Safex twin fog was used to generate smoke created from a mixture of glycol and water. The particle size was not exactly known, but was sufficient enough to trace the complex vortex structures. the smoke was directly introduced into the tunnel and the seeding distribution was ensured to homogeneous and sufficiently concentrated before recording images.

Calibration

Since the viewing perspective of the two cameras are different, a stereoscopic PIV experiment requires precise calibration of both cameras [19]. Carefully correcting for off-axis viewing is crucial to the evaluation process and essential for ensuring reliable results. A LaVision two level calibration plate was used for this purpose (Figure 3.19) and calibration was performed within the *DaVis FlowMaster* software.

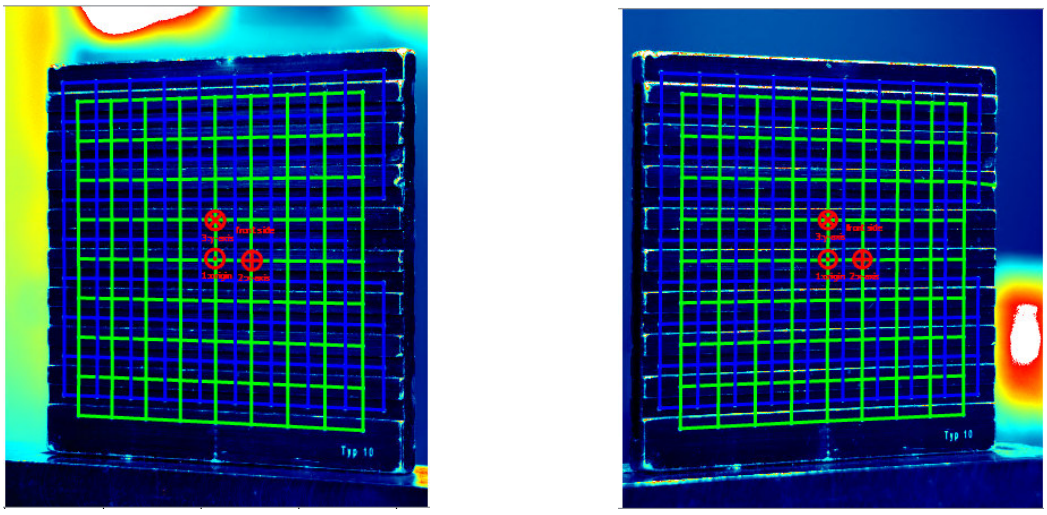

(a) Camera 1 **(b)** Camera 2

Figure 3.19: Calibration for stereo-PIV with 2 cameras

The captured images were pre-processed to adjust for normalising the light intensities throughout the plane and to remove any unnecessary background. An additional problem associated with PIV setup is the misalignment of the laser sheet with the calibration plate, i.e., the captured plane as depicted in. This could potentially cause errors in vector calculation, which materialize as a disparity vector as shown in Figure 3.20. The disparity vector is crucial for understanding the self-calibration procedure. After calibrating the cameras, the $z = 0mm$ plane is defined by the calibration plate's surface. The laser light sheet usually deviates from this plane. Dewarping images transforms them as if captured by a camera perpendicular to the light sheet on the z-axis, assuming particles are in the $z = 0mm$ plane. If the light sheet coincides with this plane, particles appear at the same (x, y) positions in dewarped images from both cameras. If the light sheet is behind the $z = 0mm$ plane, particles shift left in the left camera's view and right in the right camera's view. The disparity vector is defined as the vector that connects these shifted positions (Figure 3.20), with its length increasing as the light sheet moves further from the $z = 0mm$ plane.

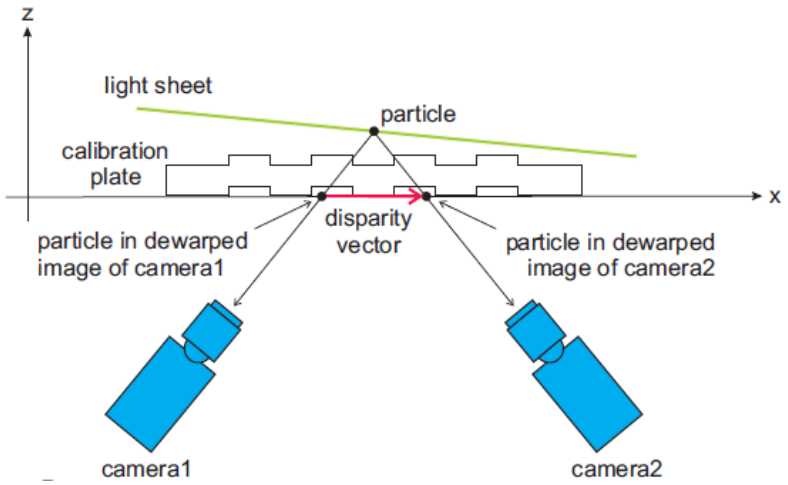

Figure 3.20: Misalignment of the laser sheet with the calibration plate and resulting disparity

The Planar ***Self-Calibration*** in DaVis provides the possibility to adjust the coordinate system and the camera calibration of a stereoscopic PIV setup in such a way that the plane $z = 0mm$ will be adjusted exactly to the center of the laser light sheet [19]. The disparity map is calculated from peak positions of the correlation map. The correlation and disparity maps after the planar self-calibration process are depicted in Figure 3.21, and the calibration properties are depicted in Figure 3.22. It was ensured that the minimum correlation peak was 0.5 while the maximum absolute disparity in the y direction was $0.4mm$.

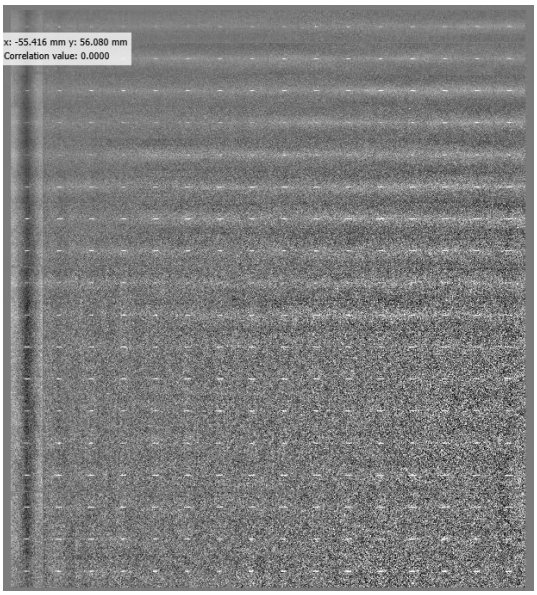

(a) Correlation peaks after self-calibration

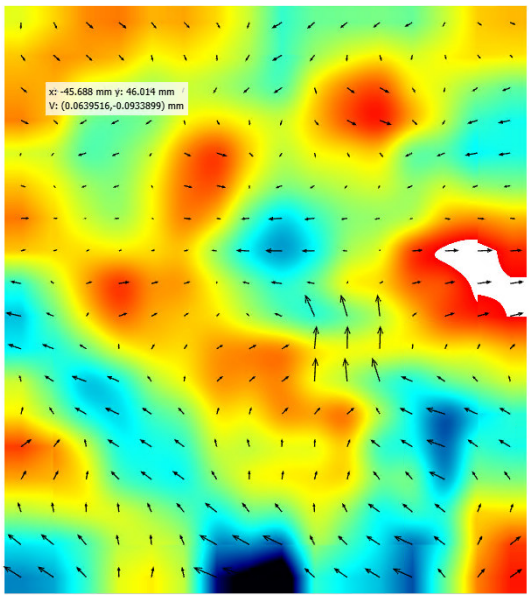

(b) Disparity map after self-calibration

Figure 3.21: PIV Self calibration

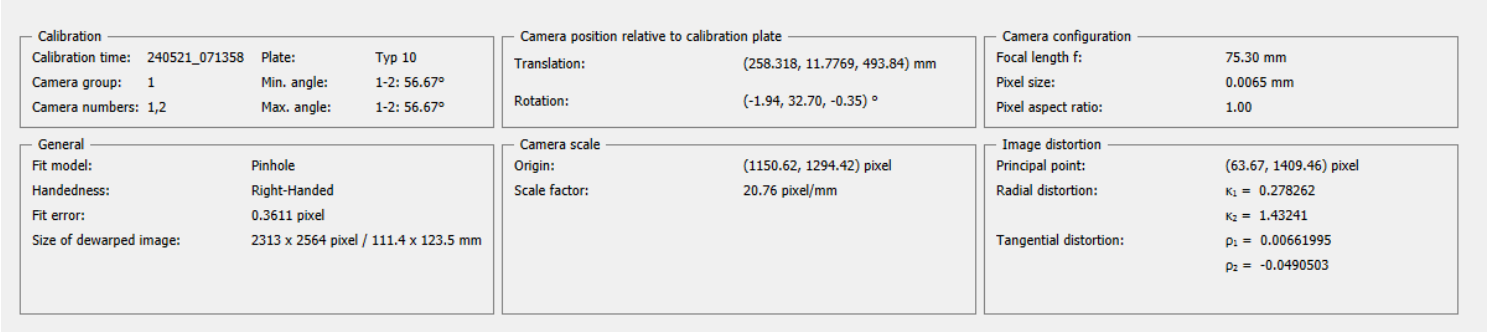

Figure 3.22: Self-calibration Properties

Post-processing

The captured images were post-processed using *Davis FlowMaster 10.2* using a multipass algorithm. A multi-pass algorithm is an iterative method wherein the interrogation windows are moved in order to follow the particle path, with or without decreasing the window size in the subsequent iterations. The window size was maintained constant in our case. This, when compared to a single-pass method, gives a higher signal-to-noise ratio for the correlation and hence a better flow resolution.The following makes up the multipass algorithm:

- 1 Initial: 50% overlap, 32×32 window
- 4 Final: 75% overlap, 12×12 window

Note that overlap defines the overlap among neighboring interrogation windows. The bigger the specified overlap, the closer is the grid of computed velocity vectors (the number of pixels for each interrogation window is not affected) [19]. It can be inferred that the spacial resolution of the flow was maximized in order to capture the tiniest of vortices. The ensemble size was 500 images, and the obtained grid spacing in the crossflow plane was $0.1444mm \times 0.1445mm$.

Finally, some of the additional tools in DaVis were utilized to refine the results:

- Vectoring filtering to remove windows with correlation values less than 0.5
- Universal outlier detection

4

Results & Discussion

The following chapter presents the important results produced from the thesis work. The major aspect of the discussion will be on the qualitative and quantitative comparison between the non-slotted and the different slotted winglets (refer subsection 3.1.1), highlighting the effect of slots and flexibility of wingtips on aerodynamics of the wing. The primary focus of the analysis will be laid on the freestream velocity of $U_\infty = 10m/s$, resembling the gliding/soaring speed of birds such as Jackdaws, which are approximately in the range of 6-11 m/s [28, 47]. The freestream velocity measured by the PIV method was slighter higher than the set velocity in the wind tunnel as mentioned in subsection 3.3.3, resulting in an uncertainty $\leq 4.5\%$.

The chapter begins with a briefing on the bending of the wingtips, followed by a general discussion on the instantaneous velocity fields. The chapter then dives deeper into a qualitative wake analysis composing of studies of vortex characteristics and dynamics for slotted and non-slotted winglets. Later, a more quantitative analysis will follow, including a discussion on the aerodynamic performance of different winglets and the estimation of drag components using a far-field wake integral approach. The cross-plane velocity field data from the stereo-PIV experiment shall be utilized for the wake integral based drag estimation and for the instantaneous and averaged contours. The data from the near-field plane 1 ($x/c = 0.23$) will be used for the visualization of the immediate wake, in order to capture the vortex breakdown before the vortex structures dissipate. On the other hand, the data from mid-plane 2 ($x/c = 2.3$) and far-field plane 3 ($x/c = 4.6$) shall be utilized for the wake integral approaches, as they are more closer to satisfying the far-field assumption (subsection 3.2.3).

Note: The velocity components are in the nominal aerospace convention, with u representing the streamwise/-chordwise component, v representing the spanwise cross-flow component and w representing the normal cross-flow component, as mentioned in Figure 3.8b.

4.1. Bending of wingtips

The results obtained from the marker tracking experiment was utilized to measure the static deflections of each of the wingtips and the tip deflections for $U_\infty = 10m/s$ and $\alpha = 10°$ and $\alpha = 15°$ have been tabulated in Table 4.1 and plotted in Figure 4.1. The maximum deflections of each of the wingtips were estimated by subtracting the y-coordinates of the tip marker of the individual tip at $U_\infty = 10m/s$ from that of $U_\infty = 0m/s$ at each angle of attack.

Winglet	$\alpha°$	Tip displacement (mm)				
		T1	T2	T3	T4	T5
PLA	10	0.24	1.87	3.12	1.86	1.04
cPLA		0.30	0.39	0.56	0.60	0.41
TPU		0.11	1.58	3.63	2.99	1.96
PLA	15	0.49	2.13	2.96	1.42	0.36
cPLA		0.43	0.90	0.94	0.93	0.71
TPU		0.58	3.70	3.59	3.09	1.77

Table 4.1: Recorded average tip deflections of each wingtip at $U_\infty = 10m/s$

As predicted, generally the wingtips of $cPLA$ ($EI_0 = 3.06E^{-2}Nm^2$) bended the least while TPU ($EI_0 = 1.7E^{-3}Nm^2$) bended the most. The bending of PLA was in between these two($EI_0 = 4.66E^{-3}Nm^2$). It was observed that tip $T3$ bended the most during the experiment, while tip $T1$ bended the least. Contrary to what was expected, the longest tip $T2$ bended lesser than the shorter $T3$ tip for all the winglets at $\alpha = 10°$ by around 14-43 %. Additionally, it was interesting to note that the $T2$ tip of PLA bending slightly more than that of TPU at $\alpha = 10°$.

Even at $\alpha = 15°$, the bending of $T2$ was more than $T3$ only for the case of TPU, but the increase was small at around 2.3 % compared to $T3$. $T3$ was followed by $T4$ in terms of greater bending at $\alpha = 10°$, then $T2$ and $T5$ while

$T1$ bended the least.

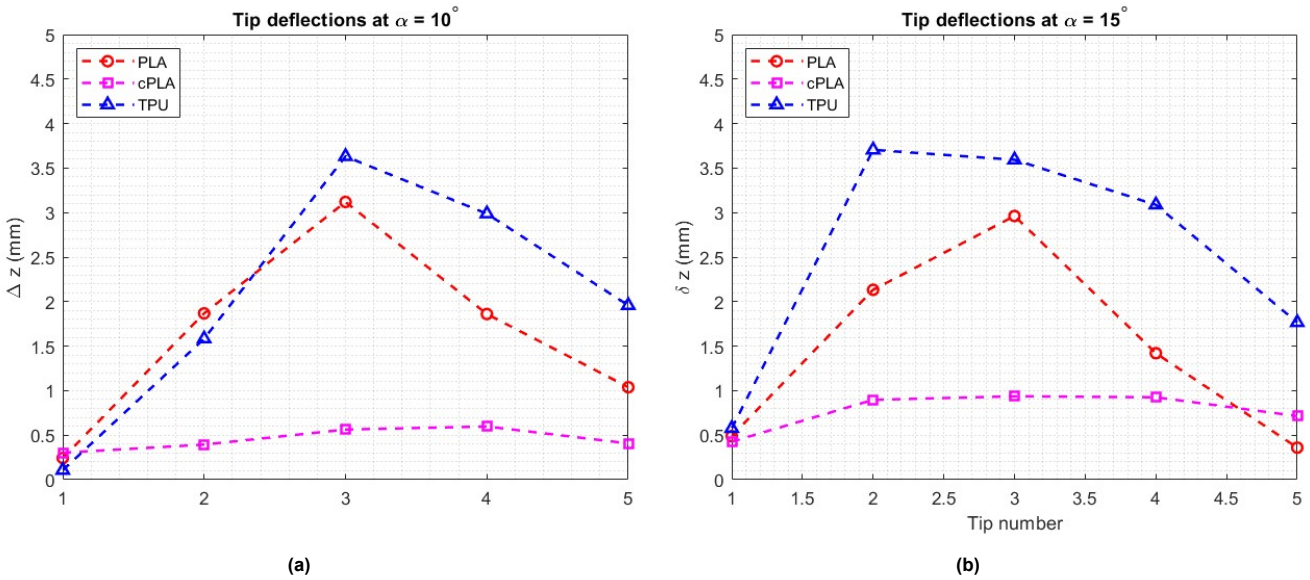

Figure 4.1: Averaged tip deflections at $U_\infty = 10m/s$

At $\alpha = 10°$, the maximum deflection ($T3$) of PLA and $cPLA$ were 14 % and 85 % lower than TPU. The same were 17% and 74 % lower at $\alpha = 15°$. Interestingly, the deflection of $PLA's$ last tip ($T5$), was lesser than that of $cPLA$ at $\alpha = 15°$. One possible reason could be the lower thickness of the wingtip of PLA inducing a flow separation towards the trailing edge and hence resulting in a loss of lift force at the wingtip location.

4.2. General discussion on Instantaneous flowfield

As mentioned in chapter 2, the breaking down of vortices by slotted tips result in a clear difference in the wake structure of the winglet. The emerging wake varies further with changing material, as can be noted from the instantaneous flow field components (u,v & w) plotted in Figure 4.2, Figure 4.3 and Figure 4.4. The flow-fields of the wake displayed were captured at Plane 1, immediately downstream of the winglet at around $x/c = 0.23$. Vectors indicating the flow direction at each pointwise location have been added on top of the contours. The contours of velocity fields have been directly taken from the DaVis software.

The single vortex core of the normal winglet was evident at $\alpha = 10°$ (see Figure 4.2). The tip vortex can be seen profoundly to curl into the singularity representing the core. Flow vectors plotted indicate a net clockwise circulation created by the tip vortex, for both the cases of slotted and unslotted winglets. In Figure 4.3 and Figure 4.4, the single vortex can be visualized a doublet distribution as they represent the cross-flow planar velocity components. The lower side of this doublet distribution has negative velocity values while the upper side has positive ones in Figure 4.3, while the same is negative on the right side and positive on the left in Figure 4.4.

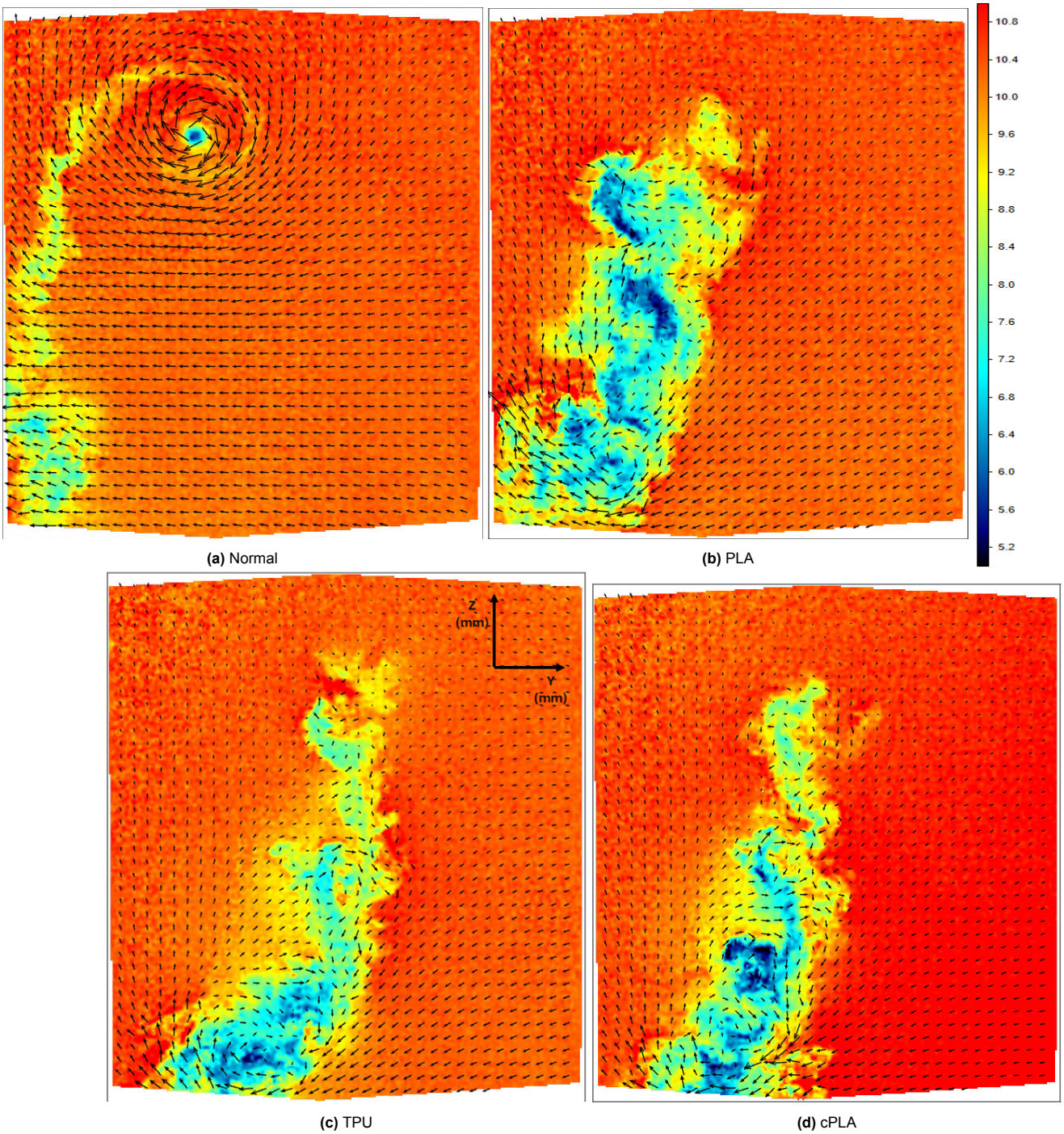

(a) Normal **(b)** PLA

(c) TPU **(d)** cPLA

Figure 4.2: Instantaneous u velocity (m/s) component at Plane 1; $\alpha = 10°$; Wind tunnel set at $U_\infty = 10m/s$

Evidently, the magnitude of the u component of the velocity field within the vortex is lower than the freestream. The vortex core, clearly visible in Figure 4.2a, has a drop in the velocity magnitude of around 20% compared to the freestream. As for the case of slotted winglets, the diffused vortex structures have regions of even lower u velocity component, dropping upto around 54% of the freestream value. Note that the longest wingtip $T2$ was almost at the same spanwise distance from the bottom as the normal winglet. It was observed from multiple instantaneous images that the tip vortex generated by the longest wingtip in the slotted winglet cases are highly diffused.

The length of the flow vectors outside the vortical region seems to indicate lower upwash magnitudes (on the left) and lower downwash (on the right) for the slotted winglets, as compared to the unslotted winglet. This serves as an additional supporting evidence to the net circulation results presented in subsection 4.3.4.

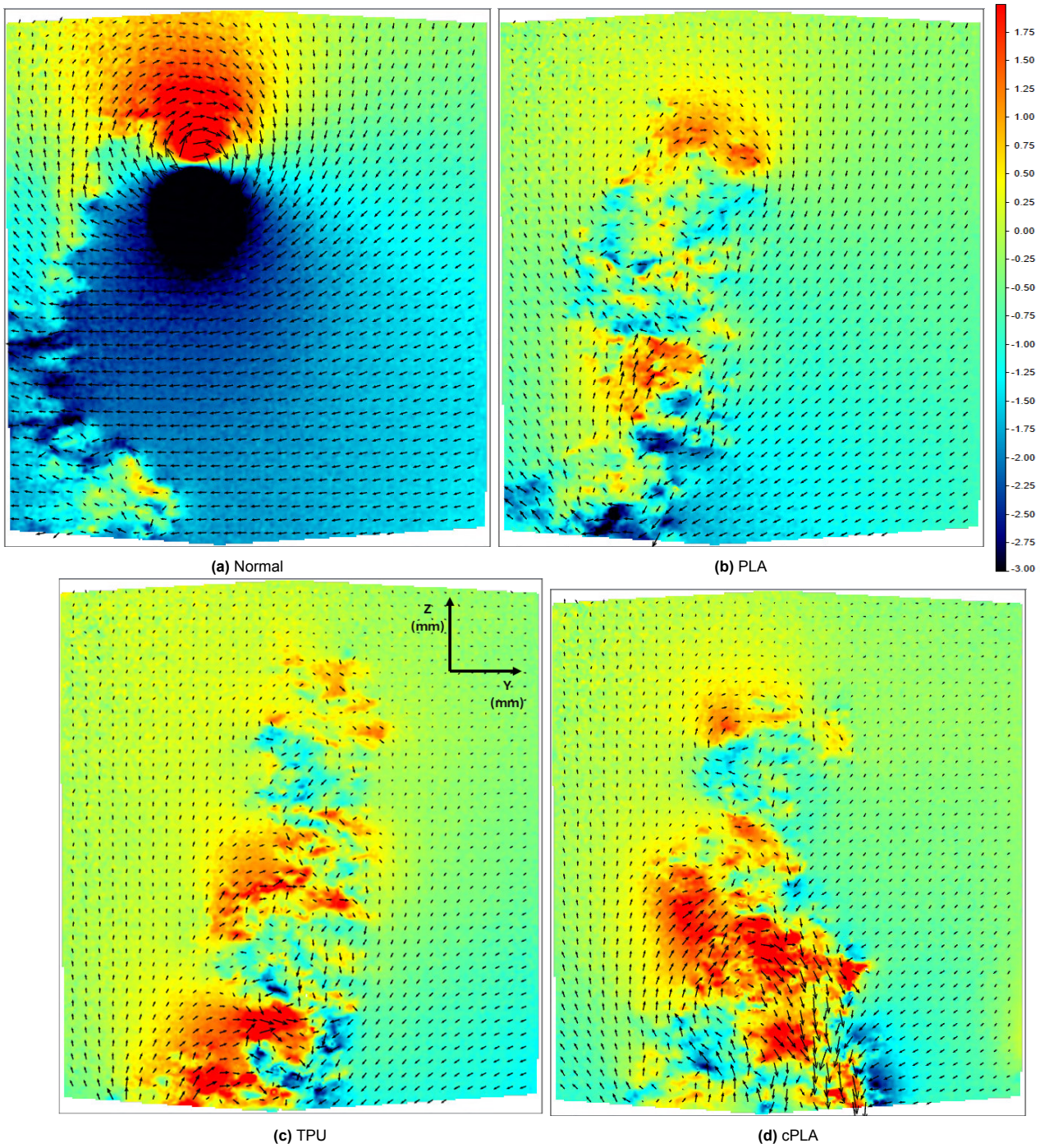

(a) Normal **(b)** PLA

(c) TPU **(d)** cPLA

Figure 4.3: Instantaneous v velocity (m/s) component at $\alpha = 10°$, Wind tunnel set at $U_\infty = 10m/s$

As mentioned previously, the v component of the velocity appears as a doublet distribution in the contour plots. At a initial glance, the vortex core locations of the slotted winglets were impossible to locate using this inference, as they were partially/completely diffused. Only the distinctive core of the unslotted $norm$ winglet was visible with a notable doublet distribution. However, a general inference from the contour plots is that the overall v velocity distribution of the slotted winglets within the cross-flow plane seems to of a relatively lower intensity (i.e., absolute magnitude), as compared to $norm$. The dense doublet distribution seems to be more diffused or distributed for the slotted winglet cases. Since the v component is directly linked to the streamwise vorticity, this could mean lower vorticity peaks and better vorticity distribution for the slotted winglet cases.

From Equation 3.17, it could be realized that the lower vorticity peaks and density would give rise to a lower induced drag value. Therefore, one clear inference is that the breakdown of vortices leads to lower concentrations of vorticity peaks which in turn lead to a lower vortex-induced drag. As a method to estimate this effect, the values of net or integrated vorticity parameter have been discussed in subsection 4.3.4. Additionally, the quantification for this

phenomenon can be observed in subsection 4.4.3.

A better visualization of the vortex sheet produced by the slotted winglets can be seen in the contour plot of w velocity contours of in Figure 4.4. As expected, the doublet distribution of the w velocity contour of $norm$ can be observed to have rotated $90°$ with respect to the v velocity contour. The vortex sheet appears to be the most distinct for TPU in Figure 4.4c, due to the intense negative velocity pockets that are visible in the w component contour.

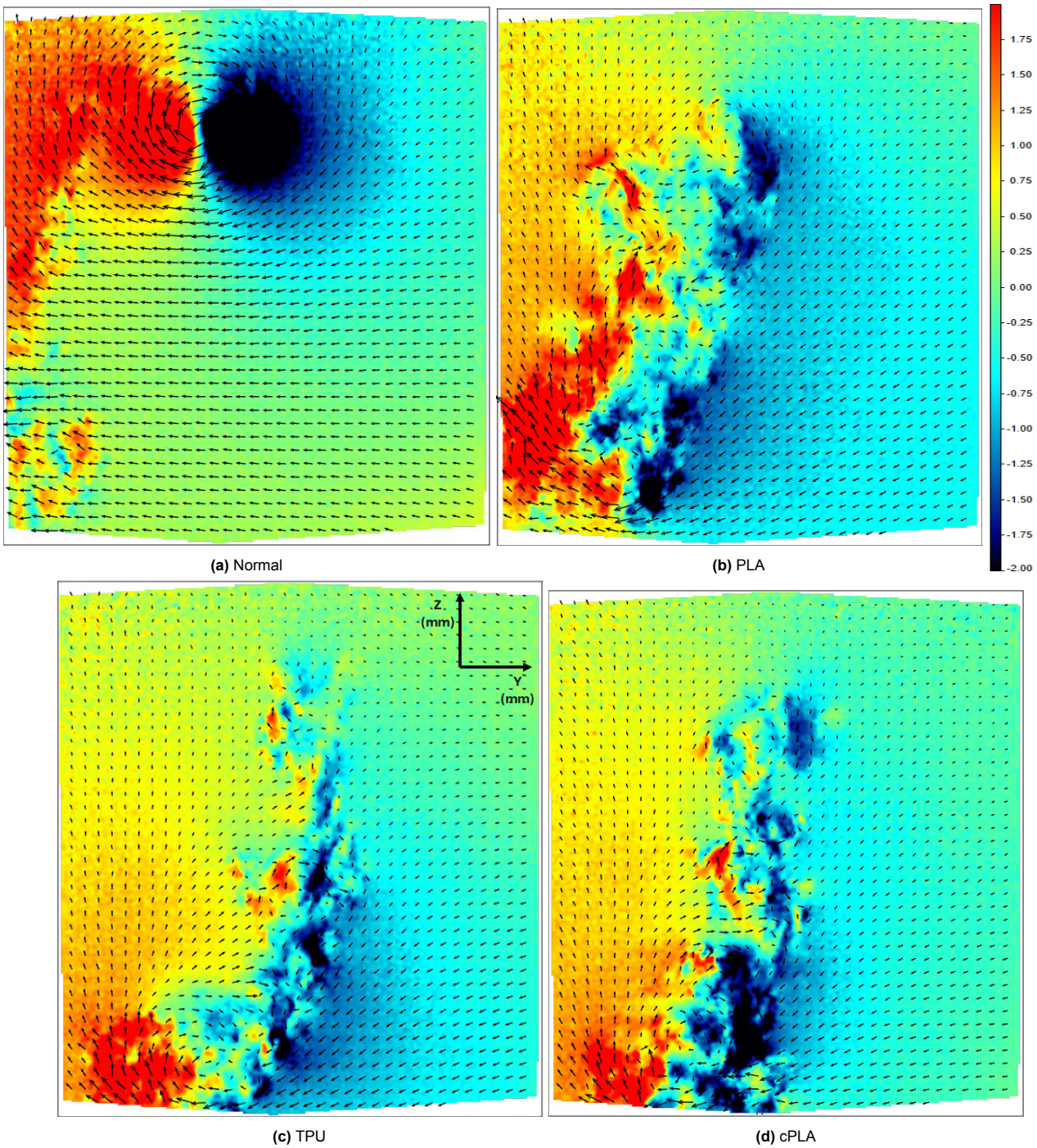

(a) Normal **(b)** PLA

(c) TPU **(d)** cPLA

Figure 4.4: Instantaneous w velocity (m/s) component at $\alpha = 10°$, Wind tunnel set at $U_\infty = 10m/s$

4.3. Wake analysis for vortex breakdown

Now that we have looked at the bending of the wingtips and how the instantaneous flow-fields in the wake look like, a brief analysis using the averaged flowfields of the wake of normal and slotted winglets will be presented in this section to further dive into how they actually correlate with each other. After an initial comparison of the wake of non-slotted and slotted winglets, the bending and flexibility of the wingtips will be associated with the streamwise vorticity fields

and a comprehensive analysis will be presented. Finally, the vortex core characteristics will be explained further using the $Q - criterion$ to end the section.

The averaged flowfield data was extracted from *DaVis* during post-processing. However, the obtained data was noisy and a Gaussian filter was used in order to smoothen the velocity components and gradient data. A filter kernel with standard deviation $\sigma_{gauss} = 3$ was utilized in Matlab for the smoothing. Furthermore, since the gradient operator introduces noise into the Q criteria [24], an additional Gaussian kernel with $\sigma_{gauss} = 6$ was used on the calculated Q-criteria data. As an example the raw data and the corresponding filtered data of Q-criteria can be seen in Figure 4.5.

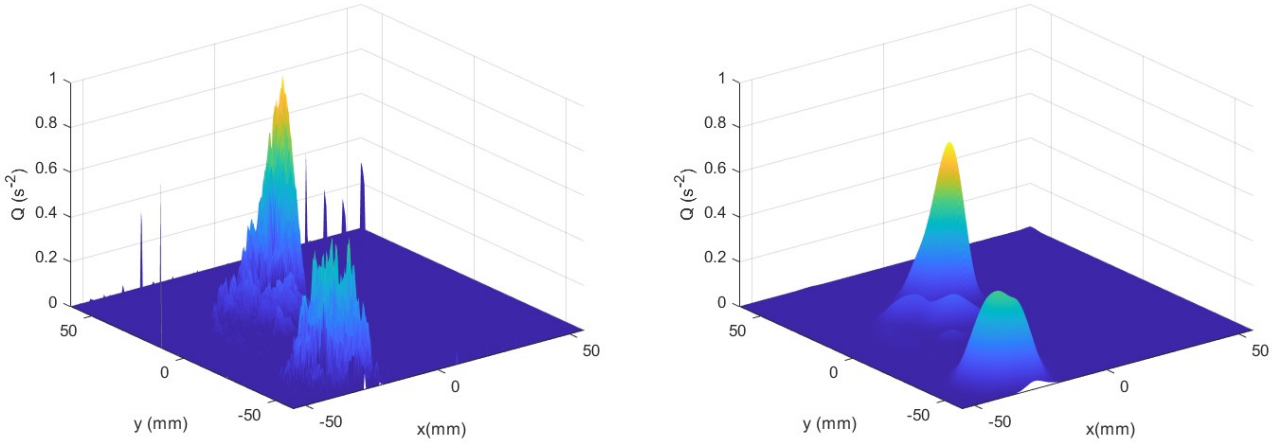

(a) Unfiltered **(b)** Filtered

Figure 4.5: Filtering of 2D Q-criteria surface plots for PLA

4.3.1. Averaged velocity field

The averaged velocity data obtained from DaVis was filtered or smoothened using a Matlab script, as mentioned previously in section 4.3. Additionally, the boundary values of the velocity field were removed as they were determined to be inaccurate outliers (due to lack of boundary conditions in the open-jet conditions) and as they didn't provide any valuable data.

Cross-flow planar velocities and core locations

Contour plots were generated for each of the case and the v component of velocity turned out to be particularly interesting. The velocity component was normalized with respect to the freestream values, and can be seen in Figure 4.6. It can be noted that at $\alpha = 10°$, multiple (upto 3) vortex cores materialize for the slotted winglets, and can be seen as doublet distributions since it represents a cross-plane component.

Particularly, the vortex emerging from the longest tip $T2$ (refer Figure 3.8b) was now evident in all the winglet cases. Patently, this is because the tip vortex of $T2$ does not interfere with the other tip vortices due to the height of the tip. The TPU and $cPLA$ winglets were seen to possess 3 vortex cores, which were identified through the peaks in the v velocity contour. On the other hand, PLA had 2 notable cores. However in general, the peak magnitudes at the three cores of TPU were lower compared to the other three winglets.

The vortex cores of the slotted winglets Figure 4.6b, Figure 4.6d, Figure 4.6c) is indeed at a lower core strength than that of the unslotted winglet (Figure 4.6a), as can be inferred from the v component plots. The winglet $norm$ has higher magnitudes of cross-flow velocities than the slotted winglets in the plane, at the vortex core and in the region surrounding it. This was expected however, as the slots breakdown the tip vortex and its circulation strength along with it. Within the slotted winglets,the $T2$ vortex core of TPU (Figure 4.6c) seems to have a lower magnitude of v velocity component, while PLA seems to have the highest. Comparing the slotted winglets with the unslotted one - the maximum value of the positive v component (corresponding to the core of $T2$ vortex) in the cross-flow plane field of PLA was 73 % lower than of that of $norm$, $cPLA$ was 82 % lower and TPU was the least at 90 % lesser magnitude than $norm$.

In addition to the magnitudes, the flowfield contours can be seen to possess different regions of positive and negative values of v velocity component, indicating the direction of the cross-flow. From the instantaneous flow vectors in Figure 4.3 it can be inferred that the flow in the bottom of the plane is from left to right and is represented with a negative magnitude, while the flow at the upper regions of the plane has positive values since they flow from left to

right. In the bigger picture, along with the w component visualization in Figure 4.7, this confirms the clockwise net circulation of flow within the plane, as briefed in Figure 4.15.

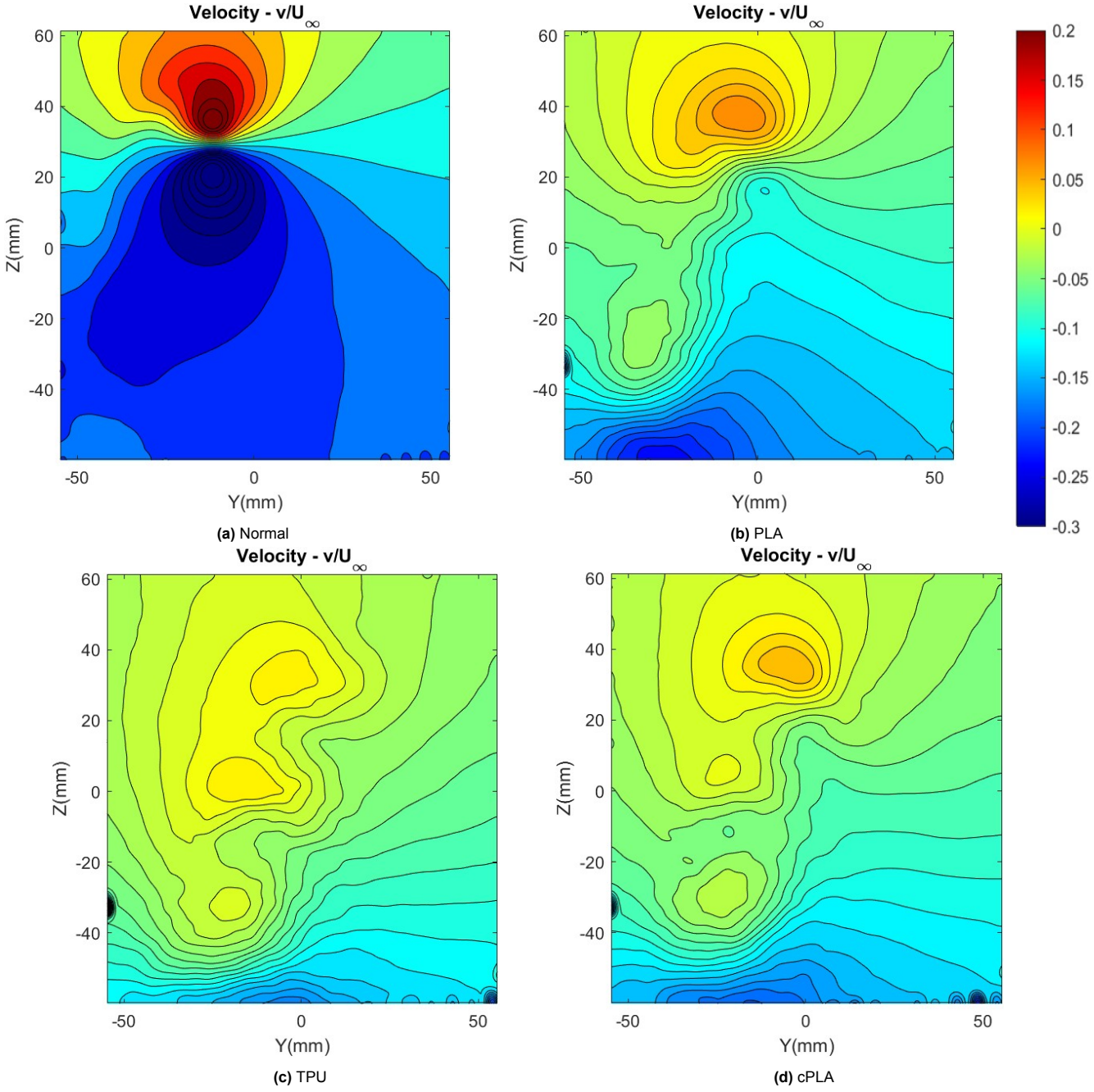

(a) Normal **(b)** PLA **(c)** TPU **(d)** cPLA

Figure 4.6: Averaged v velocity field with identified vortex core locations at Plane 1, $U_\infty = 10m/s$; $\alpha = 10°$

Looking at the cross-flow normal component w, the phenomenon of *spreading of vorticity* could be understood even further. Firstly, following the analysis of the averaged v component, it is quite clear now by looking at the sign of the normalized w velocities in different regions of the plane that there is a net upwash effect on the left side of the plane (flow is from bottom to top) and a net downwash effect on the right (flow is from top to bottom), thus creating a net clockwise circulation motion within the plane. There is little to no counter-rotation in the velocity field. Secondly, the intensity of the magnitude of w velocity could be seen to be distributed and thus less dense for the slotted wingtips compared to the normal one. Following from the initial analysis of the instantaneous flow contours in section 4.2, this confirms the spread of vorticity by the slotted winglets.

Looking at the slotted winglets cases, there seems to be a vortex core visible prominently at the bottom of Figure 4.7b, Figure 4.7c and Figure 4.7d. This could possibly be the $T5$ tip vortex cores, partially or completely merged with that of the $T4$ vortex core. Furthermore, the $T2$ vortex at the top seems to be completely dissipated with the TPU winglet, strongly notable in PLA, while $cPLA's\ T2$ core is visible yet less intense in terms of peak magnitudes, compared to

PLA. There could be a play of flexibility in this resulting phenomenon, as TPU is the most flexible material and has no $T2$ core visible, possibly due to higher effective angle of attack from bending and/or tip oscillation. It has to noted that the young's modulus (E) of the 3D printed material of PLA is the highest, followed by $cPLA$ and TPU at the lowest E. (Table 3.6).

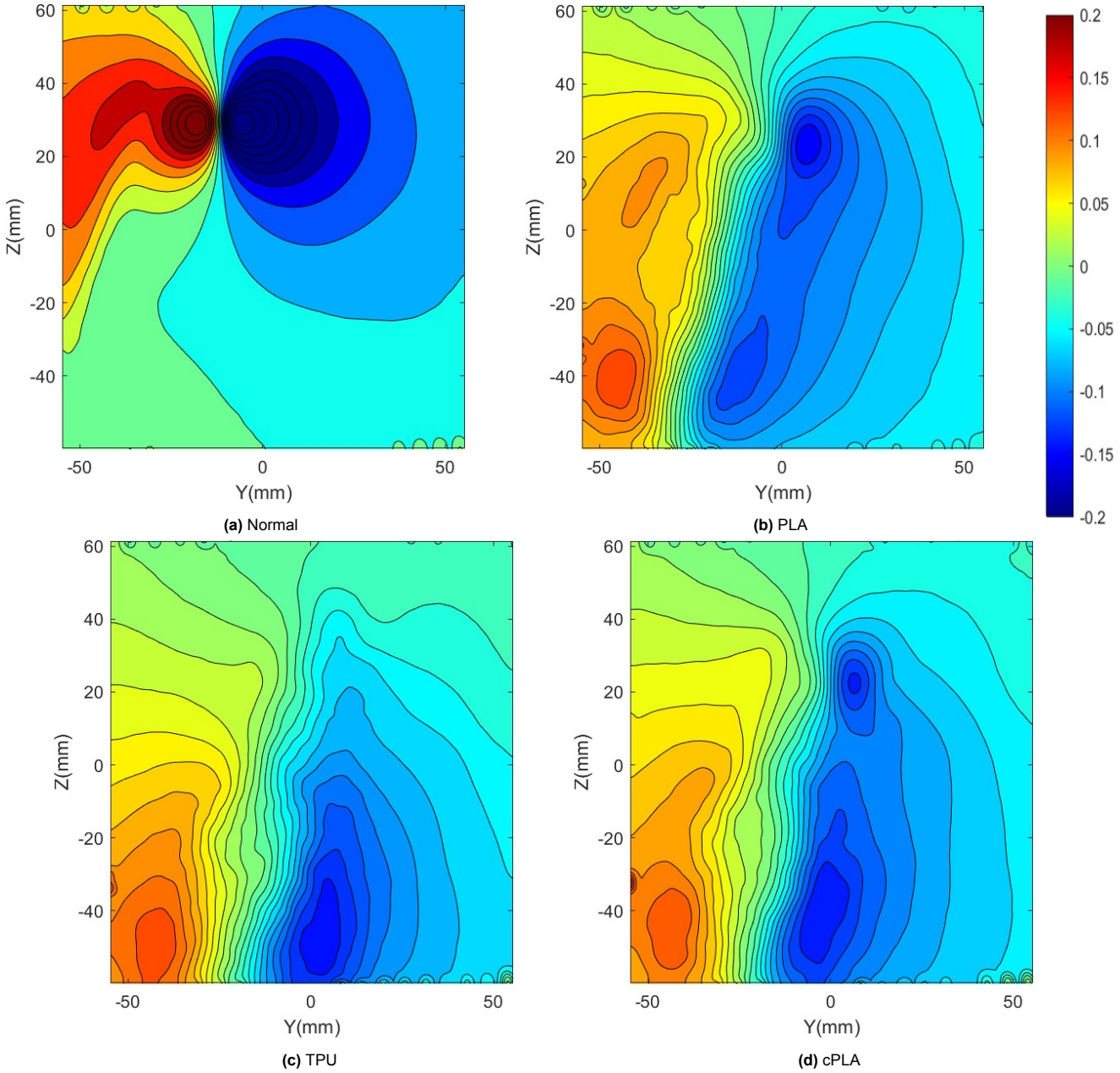

(a) Normal **(b)** PLA **(c)** TPU **(d)** cPLA

Figure 4.7: Averaged w velocity field with identified vortex core locations at Plane 1, $U_\infty = 10m/s$; $\alpha = 10°$

Effect of angle of attack (α)

The flowfield contours of u velocity component have been displayed in Figure 4.8, indicating the change in the wake vortex structure with respect to the angle of attack. The flow velocity in the x direction has reduced upto 50% of the freestream values, and the local minima points correspond with vortex cores. Comparing the averaged contours here with the instantaneous contours in Figure 4.2, it can be inferred that there has been vortex wandering (lateral motion in this context) at a greater extent for the slotted winglets, the individual vortices appear as a huge blob now. Additionally, the width of the averaged wake vortex structure appears to be higher for the higher angles of attack which is expected. The peak u velocity magnitude is evidently higher for the case of $\alpha = 15°$. On the other hand, the normal winglet ($norm$) moreover seems to be invariant in terms of the tip vortex structure, and the tip vortex is most prominently visible at all the angles of attack.

At $\alpha = 15°$, it can be observed through Figure 4.8 that there are multiple regions of reduced u velocity visible (compared to U_∞), and is most notable in the contour plot of PLA (Figure 4.8f), as compared to TPU and $cPLA$ in Figure 4.8i and Figure 4.8l respectively. There are two prominent troughs visible, particularly in Figure 4.8f. This could possibly indicate the location of one or more tip vortex cores, however, it is quite hard to talk about the level of mixing or overlapping of these vortices. Comparing the flowfields of $\alpha = 10°$ and $\alpha = 15°$, it can be inferred that the vortex cores are starting to materialize after $\alpha = 10°$, as the troughs are more significant at $\alpha = 15°$, but not at $\alpha = 10°$. In line with the physics of the wake region and flow separation, the global minima of magnitude of the averaged u velocity in the flowfield at $\alpha = 15°$ is around 13.33 % lower than that of $\alpha = 10°$. The same is around 23.5% lower than that of $\alpha = 0°$.

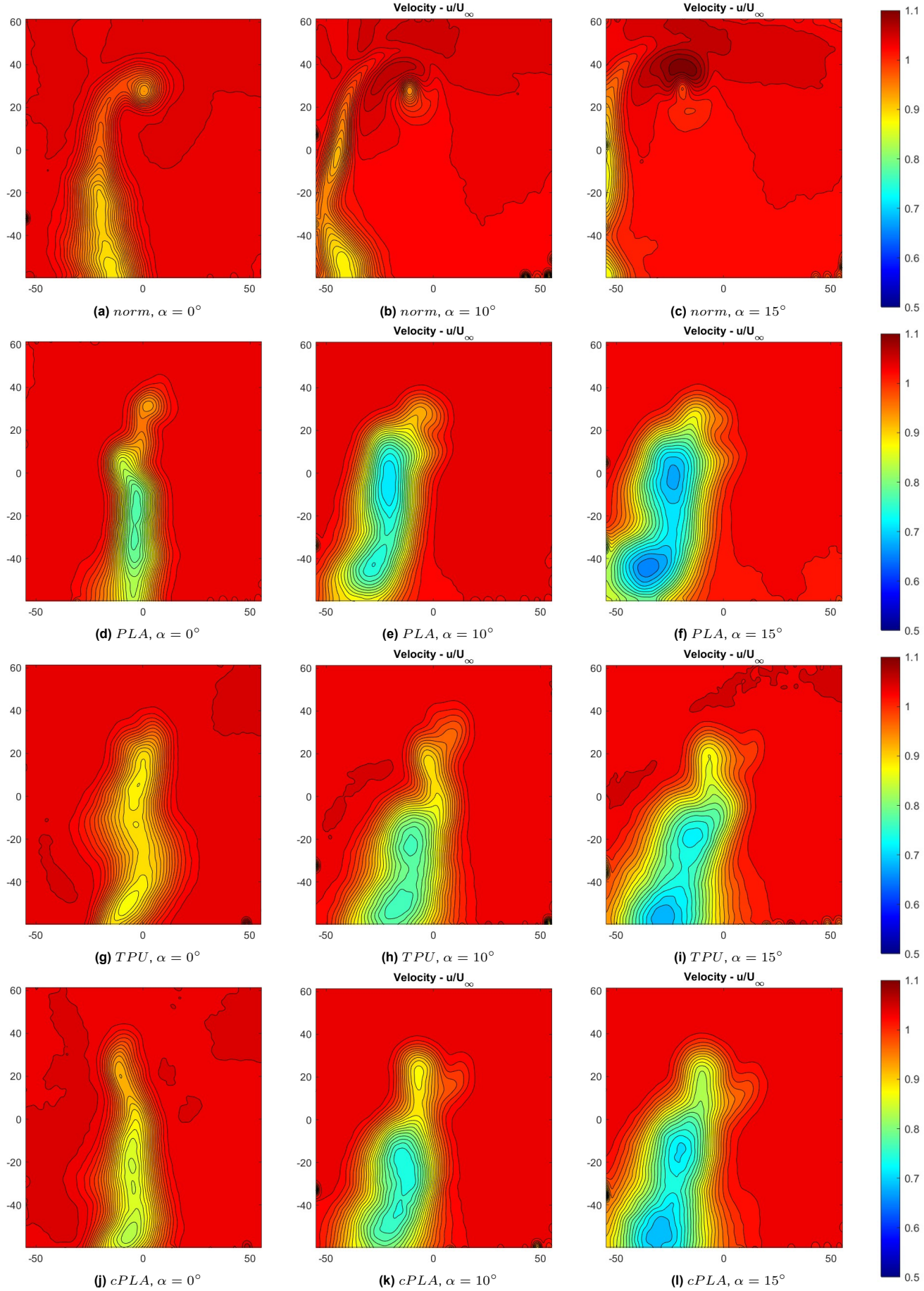

(a) $norm$, $\alpha = 0°$ **(b)** $norm$, $\alpha = 10°$ **(c)** $norm$, $\alpha = 15°$

(d) PLA, $\alpha = 0°$ **(e)** PLA, $\alpha = 10°$ **(f)** PLA, $\alpha = 15°$

(g) TPU, $\alpha = 0°$ **(h)** TPU, $\alpha = 10°$ **(i)** TPU, $\alpha = 15°$

(j) $cPLA$, $\alpha = 0°$ **(k)** $cPLA$, $\alpha = 10°$ **(l)** $cPLA$, $\alpha = 15°$

Figure 4.8: Effect of α visualized through averaged and normalized u velocity field (u/U_∞) at Plane 1 $(x/c = 0.23)$, $U_\infty = 10m/s$

4.3.2. Visualization of formation of tip vortices

Streamwise vorticity field is one of the key parameters essential to analysing the wake of a wing. The vortices generated could induce upwash/downwash on a following object in the wake region, and the amount of rotation on the object caused by this upwash/downwash could be analysed using the streamwise vorticity data. It is essential to note that the vorticity magnitude tends to infinity at the core, i.e., the core acts as a $singularity$ where $\omega_x \to \infty$. The streamwise vorticity using the PIV cross-flow planar data can be defined as follows:

$$\omega_x = \frac{\partial w}{\partial y} - \frac{\partial v}{\partial z} \tag{4.1}$$

The streamwise vorticity contour obtained has been presented in this subsection alongside the average deformations of each of the winglet's wingtips in order to depict the impact of the static deflection on the streamwise vorticity field. the vorticity vectors were normalized using the mean chord length of the winglet and the freestream velocity. Note that the normalized vorticity vectors are negative due to the clockwise orientation of the net circulation within the plane. There are outliers still present at the boundaries of the plane, however, they did not any pose any issues or impact our analysis. As can be inferred from the figures below , the vorticity levels are close to zero in the freestream, everywhere except in and around the vortex cores. The case of $\alpha = 15°$ was chosen to be presented as the distinction of the vorticity fields of different winglets and deformation of the wingtips were better noticeable.

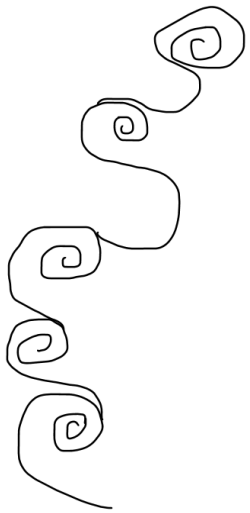

Figure 4.9: Expected tip vortex structures of the slotted winglets

The impact on the flowfield due to the addition of slots to the winglet is highly lucid. Figure 4.9 depicts the expected breakdown of the single huge tip vortex into multiple smaller vortices. However, although resembling the expected vortex sheet closely, the the structures were quite diffused with one or no prominently visible cores. The streamwise velocity component u Figure 4.2 depicts the change in the vortex structure in the wake from a distinct single vortex core to a highly diffused wake structure. The vortices in all the cases were highly diffused. As depicted in Figure 4.9,there were 5 wingtips in the model and hence there had to be 5 distinct vortices produced from the tips. The formation of tip vortices from the wingtips of the slotted winglets between $\alpha = 0°$ and $\alpha = 10°$ can be visualized in Figure 4.10. It is therefore evident from the figures that there is plethora of mixing between the vortices. The high level of diffusion could be a result of the close proximity of the wingtips, except for the longest tip $T2$ perhaps. The difference in the vortex structure(s) of the different winglets at the instantaneous times were not of much significance.

It can be noticed through the vorticity field in Figure 4.10 that at $\alpha = 0°$, the tip vortex of $norm$ is already visible along with that of the $T2$ tip (and possible $T1$) of PLA. The $T2$ tip cortex of $cPLA$ is slightly notable along with a stronger vorticity region in the bottom which appears to be a mixture of vortices from multiple tips. On the other hand, TPU barely has any vortex formation, possibly due to its highly flexible wingtips. At $\alpha = 10°$, the tip vortices of all the winglets can be noted clearly through the peaks in the streamwise vorticity. Particularly, the $T2$ tip vortex of PLA and $cPLA$ are quite significant now. However, although there is an increased vorticity region visible for TPU denoting the wake of the winglet, no significant peaks are visible compared to the other winglets. This could be the result of highly levels of turbulent mixing of the individual tip vortices leading to a reduction in the peak vorticity levels. It can clearly be noted that there unlike the rest of the slotted winglets, there is no clear $T2$ tip vortex core, which could be result of the higher bending of the tip (by $> 4.5mm$ as depicted in Figure 4.1)

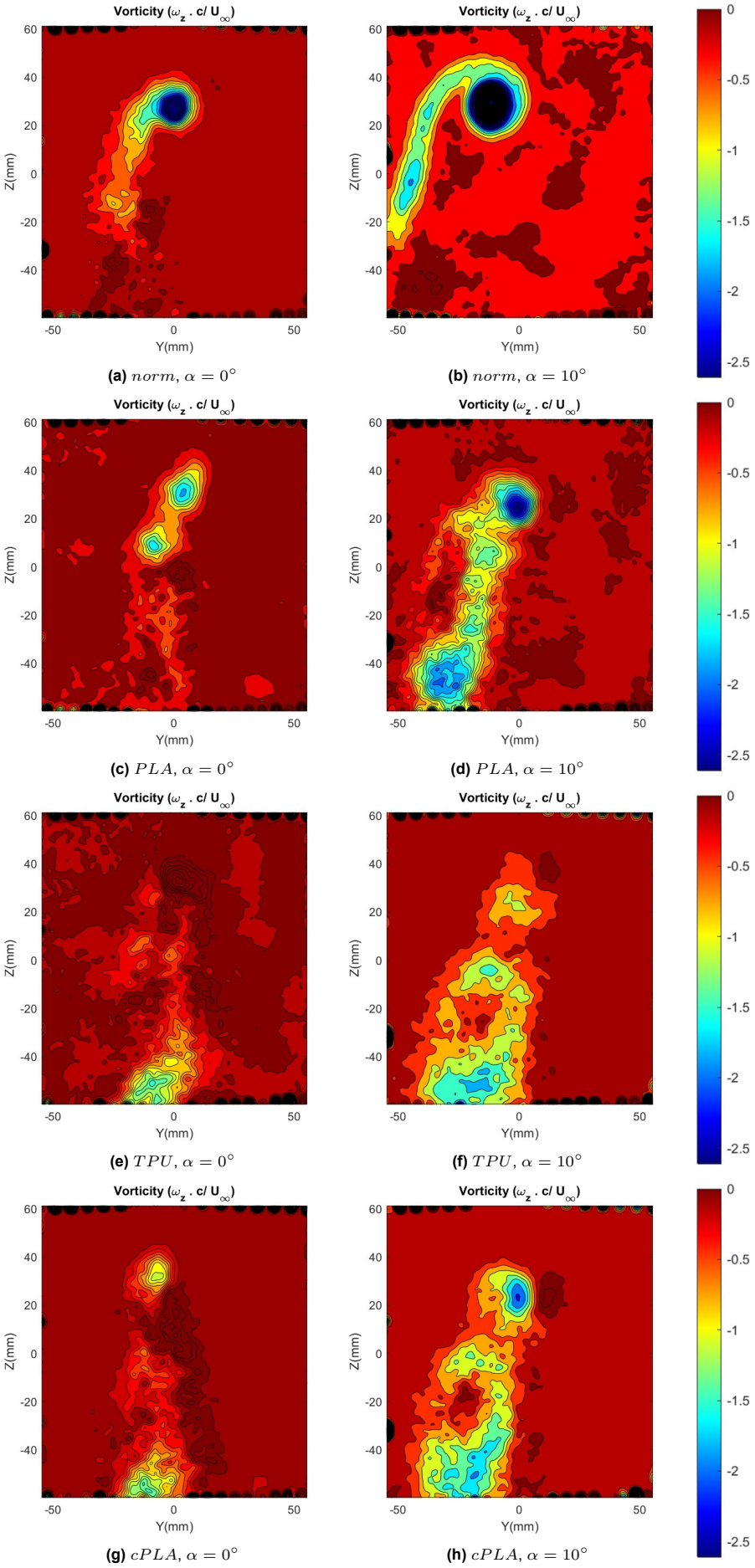

(a) $norm$, $\alpha = 0°$ **(b)** $norm$, $\alpha = 10°$

(c) PLA, $\alpha = 0°$ **(d)** PLA, $\alpha = 10°$

(e) TPU, $\alpha = 0°$ **(f)** TPU, $\alpha = 10°$

(g) $cPLA$, $\alpha = 0°$ **(h)** $cPLA$, $\alpha = 10°$

Figure 4.10: Formation of wingtip vortices visualized through averaged-normalized streamwise vorticity field $(\omega_z c/U_\infty)$ at Plane 1 $(x/c = 0.23)$, $U_\infty = 10m/s$

Although there might be a few distinct vortex cores present in the wake of the slotted winglets, they were hard to detect with the instantaneous flowfield contours from the raw PIV data. however, with a close observation of multiple images, it was inferred that the level of diffusion of the vortices from the very closely located tips $T3$ and $T4$ was more prominent in flexible TPU winglet compared to the more rigid winglets. At the bottom, there is a very high chance that the vortices from $T1$ and $T5$ have mixed together to form a larger diffused core, and this can be seen in Figure 4.2c and Figure 4.2b.

It is quite interesting to note that the vortex sheet is moreover in a linear pattern, contrasting to the vortices visualized by KleinHeerenbrink [33] for the actual Jackdaw wings which had a circular pattern of broken-down tip vortices. The circular pattern would have been the result of the rotational forces generated by the net circulation due to the tip vortices, which tend to make the individual vortices curl up into a circular pattern. This was however not seen in our case, probably due to the lack of impact from the smaller net circulatory forces.

4.3.3. Bending effect on streamwise vorticity

One general comparison that could be made between the different winglets is that the vorticity contour of TPU appears to have lower magnitudes of peak vorticity, with no distinctive peaks or in other words, no distinctive vortex cores/singularities except for a single one in the bottom. Meanwhile streamwise vorticity at the estimated location of the $T2$ vortex's (pseudo-)core for the case of TPU is around 20% lower than that of PLA and $cPLA$. A possible reason behind this could the incurrence of flow separation and/or transition to turbulence because of a higher effective α from wingtip bending of the upper tips ($T2 - T4$), as can be noticed in Figure 4.11b. The previous inference could be supported by the v velocity contour at $\alpha = 10°$ in Figure 4.6c where the location of the three different cores were notable at a relatively lower angle of attack. In addition to this, correlating with the averaged Q criteria contours at $\alpha = 10°$ for TPU, there the highest peak in vorticity is for the bottom-most vortex structure (which is a possible turbulent mixture of $T1$ and $T5$ vortices), and the $T2$ vortex core is much weaker.

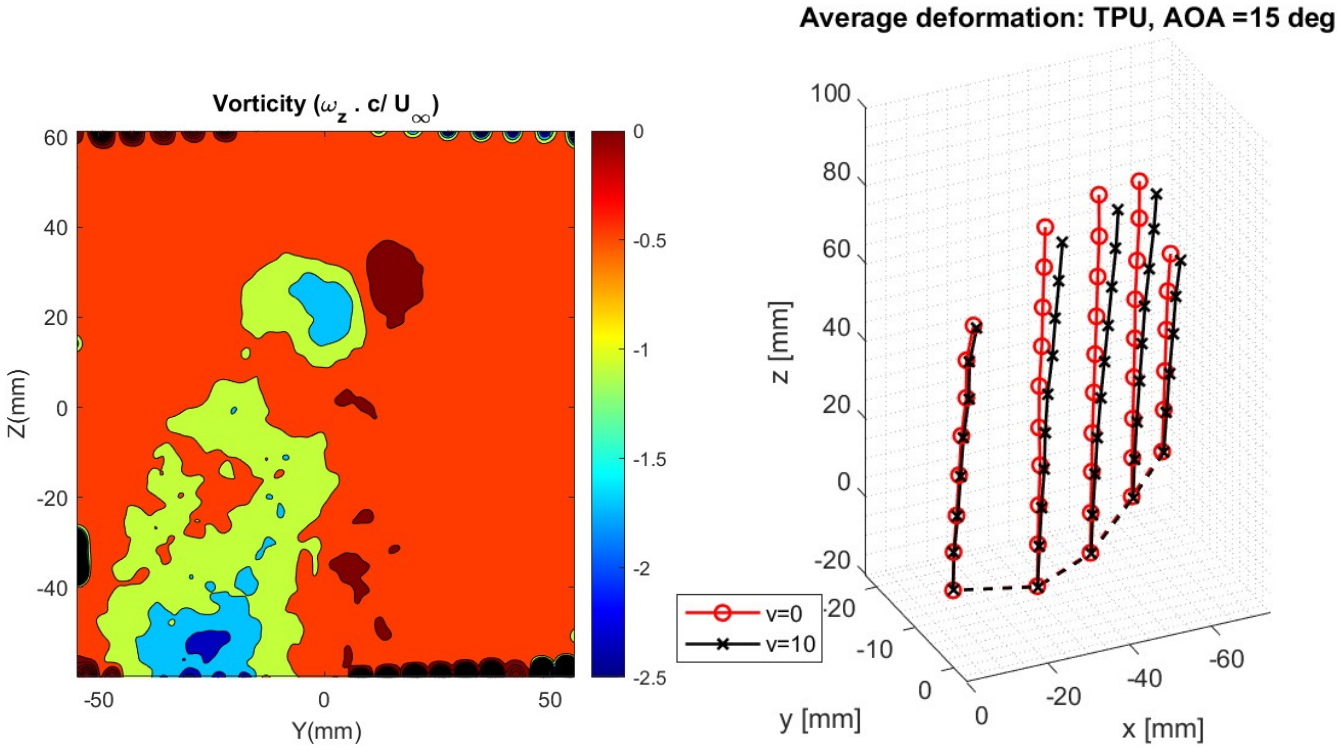

(a) Vorticity field at Plane 1 ($x/c = 0.23$)

(b) Averaged deformation of wingtips from stationary position

Figure 4.11: Normalised Vorticity and wingtip deformation of TPU ($EI_0 = 1.7 \times 10^{-3}$) at $\alpha = 15°$; $U_\infty = 10m/s$

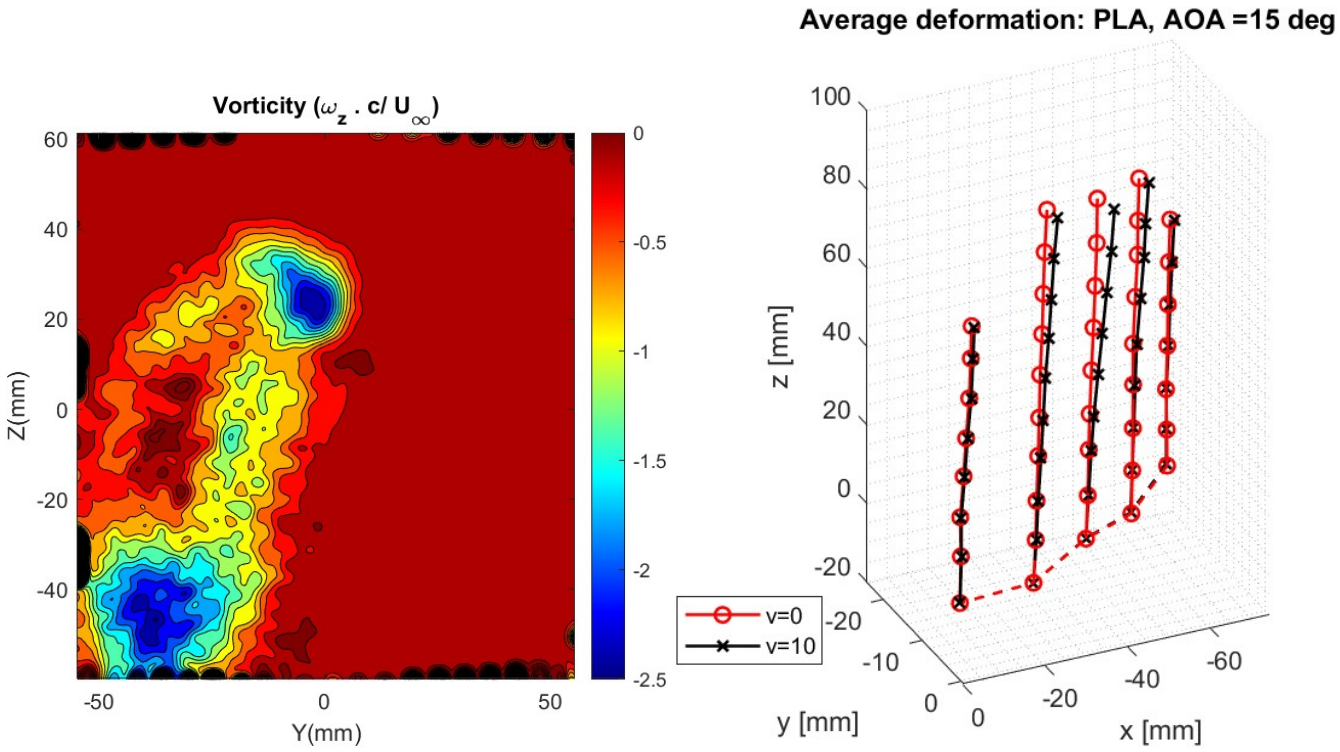

(a) Vorticity field at Plane 1 ($x/c = 0.23$)

(b) Averaged deformation of wingtips from stationary position

Figure 4.12: Normalised Vorticity and wingtip deformation of PLA ($EI_0 = 4.66 \times 10^{-3}$) at $\alpha = 15°$; $U_\infty = 10m/s$

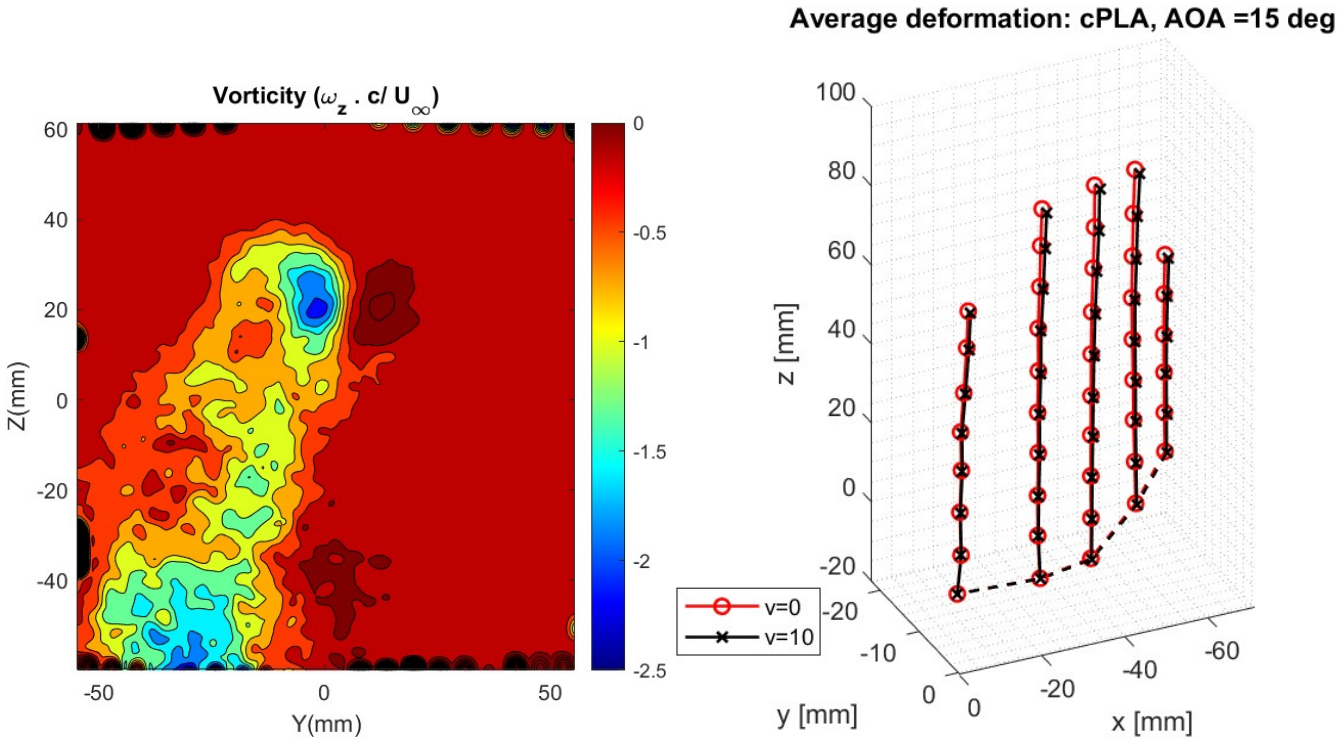

(a) Vorticity field at Plane 1 ($x/c = 0.23$)

(b) Averaged deformation of wingtips from stationary position

Figure 4.13: Normalised Vorticity and wingtip deformation of cPLA ($EI_0 = 30.6 \times 10^{-3}$) at $\alpha = 15°$; $U_\infty = 10m/s$

Is it essential to realize the reduction of the vortex strength by the slotted winglets in terms of the peak vorticity. The single vortex core in $norm$ winglet (refer Figure 4.14) was reduced into smaller vortices with vorticity peaks 90-94 % lesser in value, which is a quite enormous reduction.

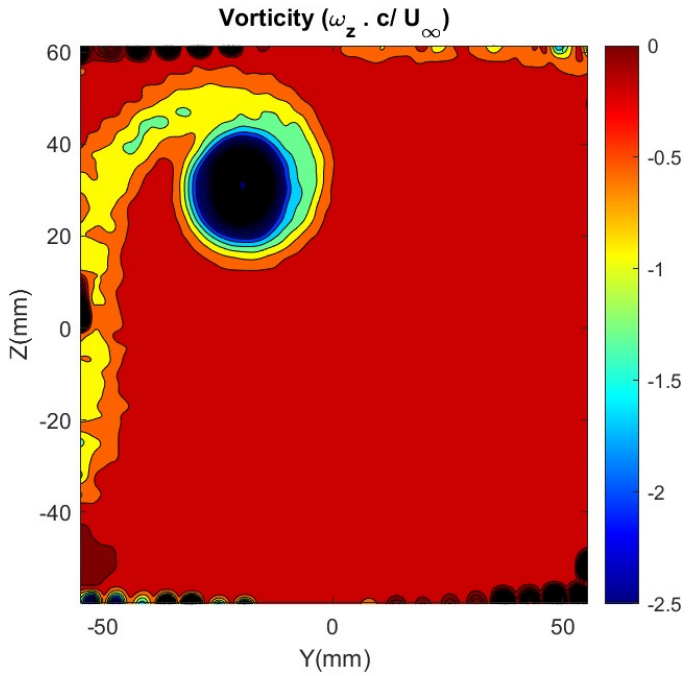

Figure 4.14: Vorticity field of $norm$ at Plane 1 ($x/c = 0.23$); $\alpha = 15°$; $U_\infty = 10m/s$

Let us now compare the peak vorticity levels of the prominently visible two vortex cores of the different winglet. Looking at the $T2$ core of Figure 4.11, Figure 4.12 and Figure 4.13, the core is the strongest for PLA. The $T2$ core of TPU is the lowest with a 36% lower streamwise vorticity peak, while the same for $cPLA$ is 14 % lower. However, it can be observed that the peak vorticity is present over a larger region within the $T2$ core of PLA than $cPLA$, indicating that the overall circulatory strength might be much higher for PLA. A similar phenomenon could be observed for the bottom vortex structure (possible mixture of $T1$ and $T5$ vortices). Observing the entire cross-plane flow field, it is evident at that this correlates well with the net circulation results at $\alpha = 15°$. Moving on to the vortex structure at the bottom of the plane, as mentioned previously, PLA winglets still persists to be the strongest in terms of streamwise vorticity in the present context. TPU has a 17% lower vorticity peak, while $cPLA$ is now the weakest at a 29% lower value.

In (Figure 4.11), except for the wingtip $T1$, all the other wingtips seem to have a notable deflection. Note that the deflection of the $T2$ wingtip in this case for TPU was $\Delta z_{T2} = 3.7mm$, which is around 36% higher than that of PLA and 53% higher than that of $cPLA$. The $T2$ wingtip has a length of $b_{T2} = 112.115mm$. Although the effective angle of attack cannot be directly estimated since the twist of the wingtip was not measured, we can use dihedral angle to indirectly talk about the angle of attack. The approximate dihedral angle (denoted by ϕ) of the $T2$ wingtip of the winglet will be:

$$\phi_i \approx tan^{-1}\left(\frac{\delta z_{T2}}{b_{T2}}\right) = tan^{-1}\left(\frac{3.7}{112.115}\right) = 1.89° \tag{4.2}$$

And hence, since the wingtips deflect further away with respect to the freestream, the tip has an effective dihedral angle of:

$$\phi_{eff} \approx \phi + \phi_i = 15 + 1.89 = 16.89° \tag{4.3}$$

The $1.89°$ increase in the effective dihedral angle the tip sees, which combined with the twist, could have possibly increased the effective angle of attack. This could have been sufficient to cause a tip stall on $T2$ and hence the resulting wake had an absence of a clear vortex core. In addition to this, there was a mild oscillation of the tip $T2$, and this was very significantly visible for TPU than the others, which could have resulted in a much distorted vortex structure during the averaging of the flowfield. On the other hand, the same $T2$ wingtip of PLA has a δz_{T2} of $2.13mm$ an hence an tip effective dihedral angle $\phi_{eff} \approx 16.09°$. This indicates that the weaker $T2$ vortex could be a product of unsteady vortex shedding and/or turbulence generated by the more flexible wingtip due to the increased ϕ_{eff} and a possible minor tip oscillation.

A concern that could arise is regarding the possibility of the thickness of the wingtips having an effect on the formation of the vortices, particularly for the smaller $T1$ and $T5$ tips, and with the vorticity peaks. TPU with the largest thickness has a more distorted or turbulent vortex structure at the bottom, the thinnest winglet PLA has a more well-noticeable vortex core while $cPLA$ with the intermediate thickness having a relatively weaker yet noticeable vortex core in the wake vortex structure. However this concern can be disregarded, as the bending of the wingtips can be seen to be a much impactful parameter than the thickness, given the smaller difference in the thickness between the winglets ($\Delta h/c < 0.02$) and the Reynolds number the experiment was held at ($Re_c \approx 5.9 \times 10^4$).

4.3.4. Net circulation & vorticity

Let ω_x represent the streamwise vorticity and Γ_x represent the net circulation in the plane. The streamwise vorticity values were integrated throughout the 2D plane, in order to have an estimate of the reduction of the total circulation strength of the tip vortex by the slotted tips:

$$\Gamma_{net} = \iint_S \boldsymbol{\omega_x} dS = \sum_{i=1}^{N}\sum_{j=1}^{N} \omega_{x_{(i,j)}} \Delta y \Delta z \tag{4.4}$$

The estimated values of the net circulation and vorticity in the streamwise direction at the near-field plane and mid-plane are plotted in Figure 4.15 for $U_\infty = 10m/s$. It is important to note that ***clockwise*** vorticity (hence circulation as well) is defined to be ***negative*** and this can be inferred from the vorticity plots in subsection 4.3.3. Evidently, the net circulation increases in magnitude with increasing angle of attack.

Let us look at the nearfield plane 1 ($x/c = 0.23$). At $\alpha = 0°$ and $\alpha = 10°$, as expected, the slotted winglets have lower net circulation magnitude than the unslotted winglet. Interestingly though, PLA with a lower flexural rigidity $EI_0 = 4.66 \times 10^{-3}$ has a greater circulation strength than $cPLA$ with $EI_0 = 30.6 \times 10^{-3}$, while TPU, which is more flexible than PLA with $EI_0 = 1.7 \times 10^{-3}$, has mitigated the circulation strength the most. At $\alpha = 0°$, the net circulation value of PLA is 37% lower, $cPLA$ is 39%, TPU is 47% lower than that of $norm$. Similarly, At $\alpha = 10°$, the net circulation magnitude of PLA is 12.13% lower, $cPLA$ is 15.36%, TPU is 34.47% lower than that of $norm$. However, there is an intriguing observation at $\alpha = 15°$. PLA now has the highest net circulation magnitude, being 7.13% higher than $norm$. TPU and $cPLA$ are close in magnitudes and are still lower than $norm$ by 17.48% and 18.38% respectively.

However, as seen in Figure 4.14, there is a possibility that the entire tip vortex wasn't captured by the field of view of the crossflow plane for $norm$, which could have resulted in an uncertainty in the data and thus, a lower net circulation magnitude for $norm$ than the other winglets.

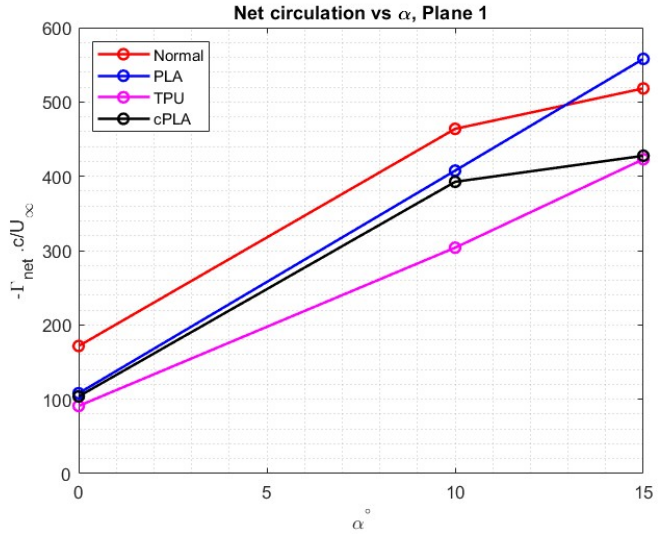

Figure 4.15: Net circulation at Plane 1; $U_\infty = 10m/s$

4.3.5. Vortex core characteristics for different winglets

Jumping into a deeper analysis on the core characteristics, In order to identify the vortex core locations and to quantify the singularities, the Q-criterion from Equation 2.8 was adapted to the 2D cross-plane velocity data that was obtained during the present thesis, as depicted in Equation 4.5.

$$Q = \frac{\partial v}{\partial y}\frac{\partial w}{\partial z} - \frac{\partial v}{\partial z}\frac{\partial w}{\partial y} - \frac{1}{2}\left(\frac{\partial v}{\partial y} + \frac{\partial w}{\partial z}\right)^2 \tag{4.5}$$

The numerical model for our adapted Q-criterion was validated using the $norm$ winglet's known vortex core location, as it possesses a single distinctive vortex core, by comparing Figure 4.16b with Figure 4.6a. It could be noticed that the adapted model was able to give an accurate location of $norm's$ vortex core, with almost no uncertainty. The adapted Q-criterion was further utilized for the slotted winglets with the hopes of precisely identifying the locations of the disintegrated tip vortex cores using the peak values in the field. Although not completely successful, the Q-criterion contour plots provided some essential inferences regarding the kinematics and dynamics of the vortices, and provides certain validation for the previously discussed results.

The difference in the vortex structures in the wake of different winglets interpreted using the normalized Q criteria can be seen in Figure 4.16. Additionally, as an extension of the analysis of the impact of α in subsection 4.3.1, Figure 4.16 depicts the waxing and waning of vortex cores as the angle of attack is increased.

Let us first consider the case of $\alpha = 10°$. As mentioned in subsection 4.3.1, the TPU and $cPLA$ were seen to possess three distinct vortex cores, probably with a few partially/completely merged, with lower peaks of Q , while PLA had two distinct one including a much stronger $T2$ vortex core. The peak Q criterion of the $T2$ vortex core of $cPLA$ is 27% lower than that of PLA, while $norm$ is around 43 % lower and TPU is at the bottom being 83 % lower. Even at $\alpha = 15°$, the peak Q criterion of the $T2$ vortex core (now significantly notable for TPU as well) of PLA is highest, $cPLA$ being 26.23% lower than PLA, however, contrasting to the case of $\alpha = 10°$, PLA is followed by TPU which is 47 % lower and $norm$ at the lowest with a 67 % lower peak than PLA. This brings us to the observation that $TPU's$ longest tip produces a distinct vortex only at a higher angle of attack. The Q values of the cores of the slotted winglets increase as the angle of attack increases. On the other hand, the single-core vortex of $norm$ has its peak Q value at $\alpha = 10°$ and reduces in strength at the $\alpha = 15°$ angle of attack, possibly due to higher momentum loss into the wake due to an increased α. Note that the each individual tip of the slotted winglet produces its own wake which may or may not combine with the wake of other tips, whereas the normal winglet has a much bigger singular wake.

An observation in Figure 4.16 is that of TPU at $\alpha = 10°$, where the bottom-most vortex structure appears to be a merger of two vortices. However at both $\alpha = 0°$ and $\alpha = 15°$, only a single vortex core (i.e., peak Q/Q_{max}) could be seen distinctly, and hence it was realized from unfiltered data that the entire blob is just a single turbulent vortex structure,and the twin-core structure was a side-effect of high filtering of the data.

Secondly, the impact of increasing the angle of attack α on the vortex formation could be observed clearly in Figure 4.16. The Q criteria contours depict this effect much better than the u velocity contours in Figure 4.8. At $\alpha = 0°$ amongst the slotted winglets, there are utmost two vortex cores visible. The vortices seem to be quite weak at this α, especially $PLA's$ cores appear to be extremely low in terms of peak Q/Q_{max} values with Q/Q_{max} in the order of 10^{-3}. The peak Q/Q_{max} values at the vortex cores were higher at $\alpha = 10°$ than at $\alpha = 15°$. This reconfirms that there is indeed loss in cross-flow momentum due to a very high effective angle of attack. The vortex core of $norm$ at $\alpha = 15°$ is at a 47% lower peak than that at $\alpha = 10°$ in terms of Q/Q_{max} values, and this indicates a possible wing stall and hence a weakened vortex. The $T2$ vortex core of PLA at $\alpha = 10°$ is 12% greater than at $\alpha = 15°$ in terms of peak Q/Q_{max}, while the same decrease is 10% and 67 % for $cPLA$ and TPU respectively. It is indeed clear that the extreme bending of the $T2$ wingtip of TPU is causing a flow separation and dissipating the vortex.

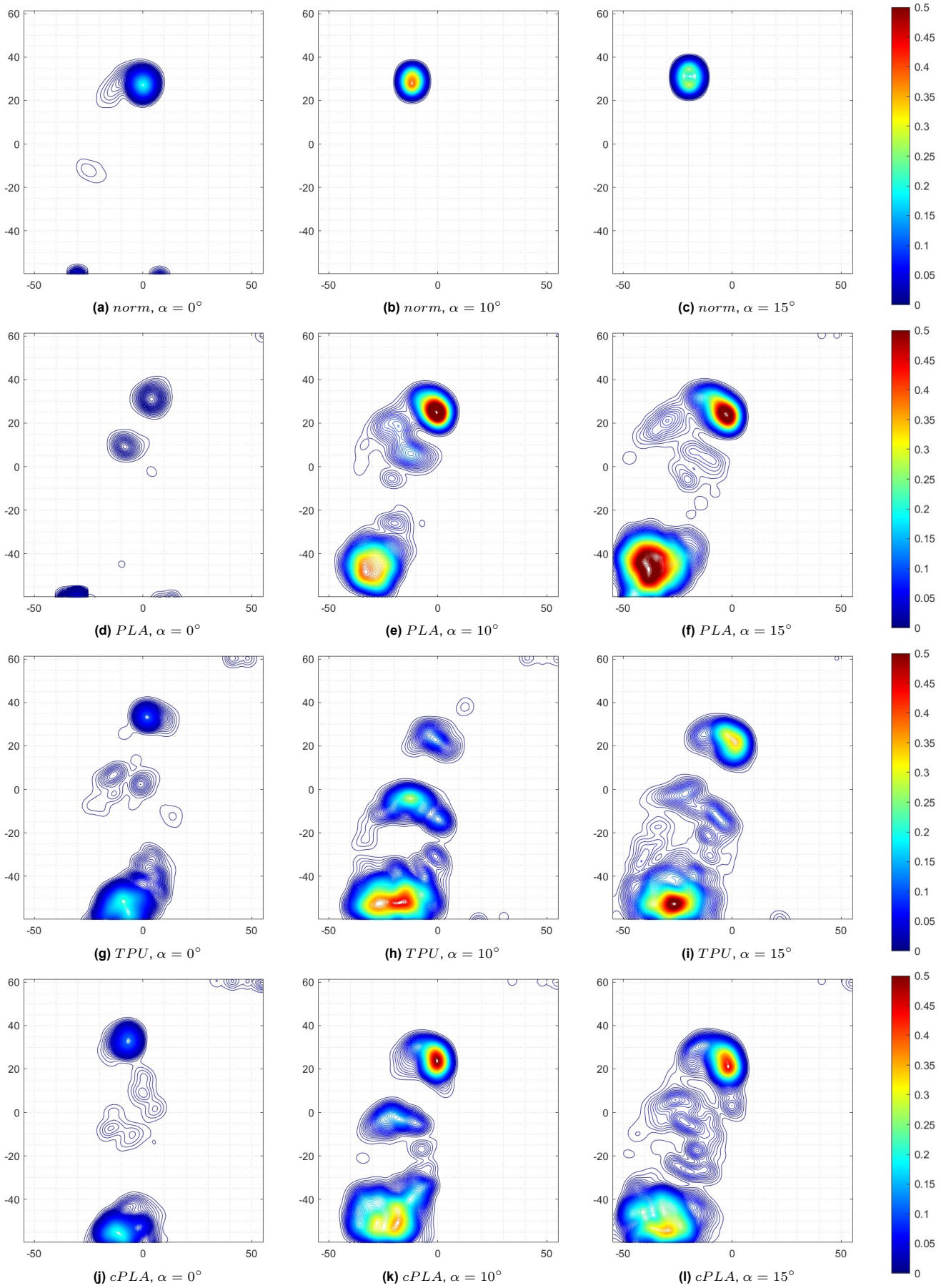

(a) $norm$, $\alpha = 0°$ **(b)** $norm$, $\alpha = 10°$ **(c)** $norm$, $\alpha = 15°$

(d) PLA, $\alpha = 0°$ **(e)** PLA, $\alpha = 10°$ **(f)** PLA, $\alpha = 15°$

(g) TPU, $\alpha = 0°$ **(h)** TPU, $\alpha = 10°$ **(i)** TPU, $\alpha = 15°$

(j) $cPLA$, $\alpha = 0°$ **(k)** $cPLA$, $\alpha = 10°$ **(l)** $cPLA$, $\alpha = 15°$

Figure 4.16: Normalized Q-criteria (Q/Q_{max}) for different winglets and α at Plane 1 $(x/c = 0.23)$, $U_\infty = 10m/s$

4.4. Aerodynamic performance

Now that we have visualized how the tip vortex breakdown looks in the wake and how the strength of the tip vortex is getting reduced, let us switch our analysis from a highly qualitative to a more quantitative perspective. The quantitative part of the thesis will dive into how much performance gain/loss the slots and flexible wingtips are being provided to the wing as a whole. During the first experimental campaign, the lift and drag forces were measured using a force balance. The behaviour of each of the winglets was analyzed across different Reynold's numbers and angles of attack. The following section presents a closer look into non-dimensionalized lift and drag parameters and how they vary for different angles of attack.

The $norm$ winglet consistently exhibited a higher lift force compared to the other materials across all angles of attack and velocities and the differences between the materials became more noticeable at higher velocities and greater angles of attack. It was observed that an abnormal kink existed in the curves of TPU at $\alpha = 5°$, as the the C_L and C_D values dropped immediately afterwards at $\alpha = 10°$ and later increased at $\alpha = 15°$. This raised a concern for the uncertainties that might have occurred during the experimental campaign that deviated the values from its true value. Therefore an uncertainty quantification was performed, and the outcome of the analysis has been presented in subsection 4.5.2. Hence, the data points at $\alpha = 5°$ was removed, and a curve fit was done based on an assumption that the graph is moreover linear between $\alpha = 0°$ and $\alpha = 10°$. This applies to both C_{L_α} and C_{D_α} polars.

One general inference that was realized is that the flow seemed to be quite unpredictable at these low Reynold's numbers ($\approx 3 \times 10^4 \, to \, 6 \times 10^4$), especially at higher angles of attack. The lift and drag coefficients were obtained by normalising the lift and drag forces using the semispan and the mean aerodynamic chord:

$$C_L = \frac{L}{1/2 \rho b c U_\infty^2} \qquad C_D = \frac{D}{1/2 \rho b c U_\infty^2} \tag{4.6}$$

where $b \approx 298mm$ is the semispan of the wing-winglet model (i.e. spanwise length between the root and the longest wingtip) and $c \approx 87mm$ refers to the mean aerodynamic chord length of the wing. The density of air was considered to be $\rho = 1.225 kg/m^3$ and the experiment was conducted at room temperature.

4.4.1. Lift of wing

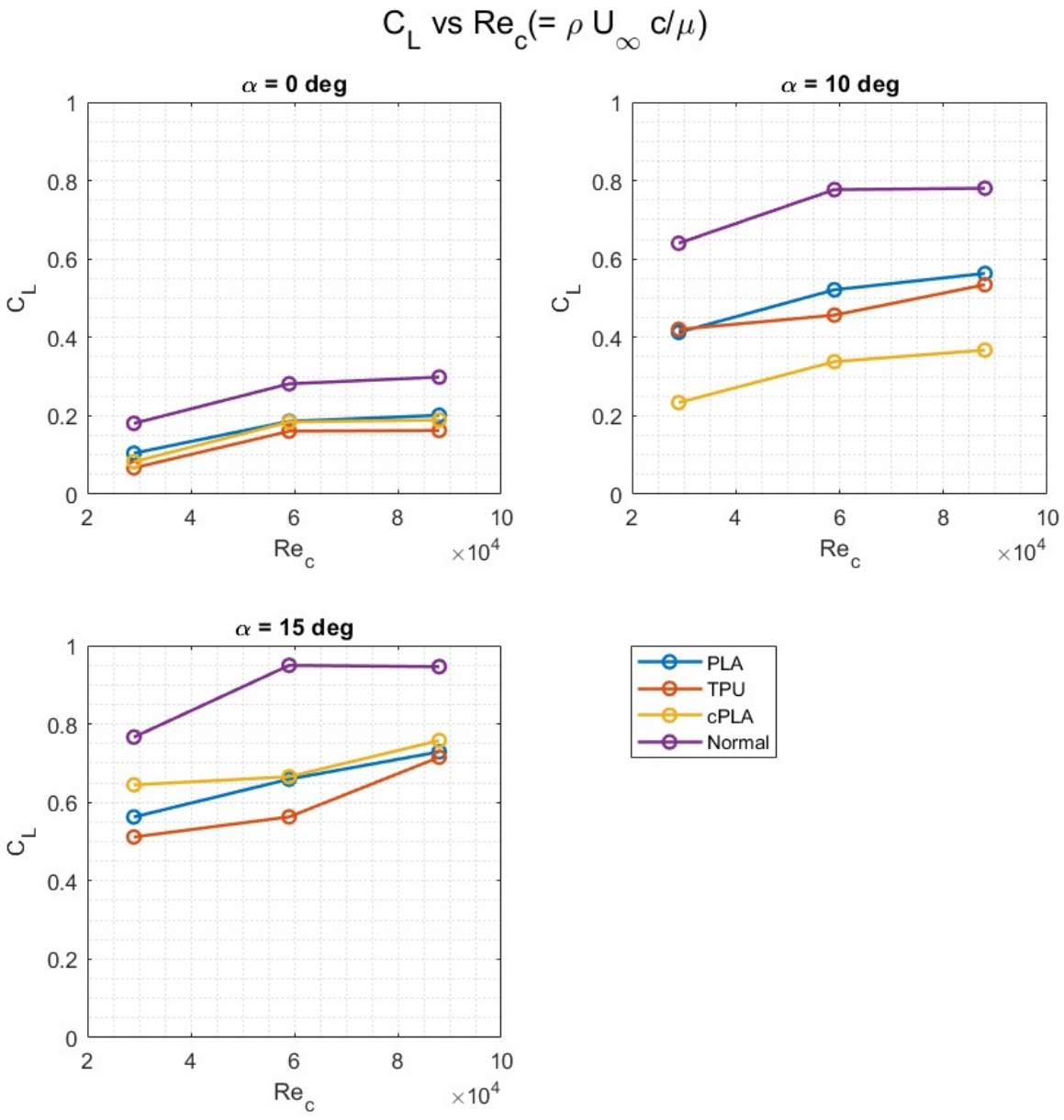

Figure 4.17: C_L vs Re_c of wing with different winglets

Firstly, it is quite evident from Figure 4.17 that C_L barley increases with increasing Re_c, whereas the angle of attack has a much bigger impact. The $C_{L_{max}}$ is barely reaching a value of 1, even at $\alpha = 15°$, which is expected at such a low Reynolds number flow. However, it is clear that $norm$ performs the best overall in the given range of angles of attack, and has a clear edge over the slotted winglets. The only exception is at $\alpha = 5°$, however, the obtained data remains with a lot of uncertainties as will be discussed in subsection 4.5.2, and hence was neglected from the plots.

At $\alpha = 0°$, the C_L values of $norm$ is almost 50% higher than that of the slotted winglets, across the entire Reynold's number regime. The C_L values of different slotted winglets however appear to be within $\pm 10\%$ of each other. At a higher angle of attack of $\alpha = 10°$, while $norm$ continues to be the highest in terms of C_L, the most rigid $cPLA$ has the least C_L values. The flexible winglets TPU and PLA seems to moreover close with respect to C_L. On the other hand, at $\alpha = 15°$, $cPLA$ has slightly higher values of C_L out of the slotted winglets, while TPU has the lowest. One possible inference is that the flow remains to be well attached and steady with the rigid winglet $cPLA$ at the highest angle of attack, thus contributing to a higher C_L. Whereas, the flexible winglets due to their bent and slightly vibrating wingtip ($T2$), has lesser C_L values. The slots and the flexibility of the wingtips are both negatively affecting the aerodynamic performance in this sense.

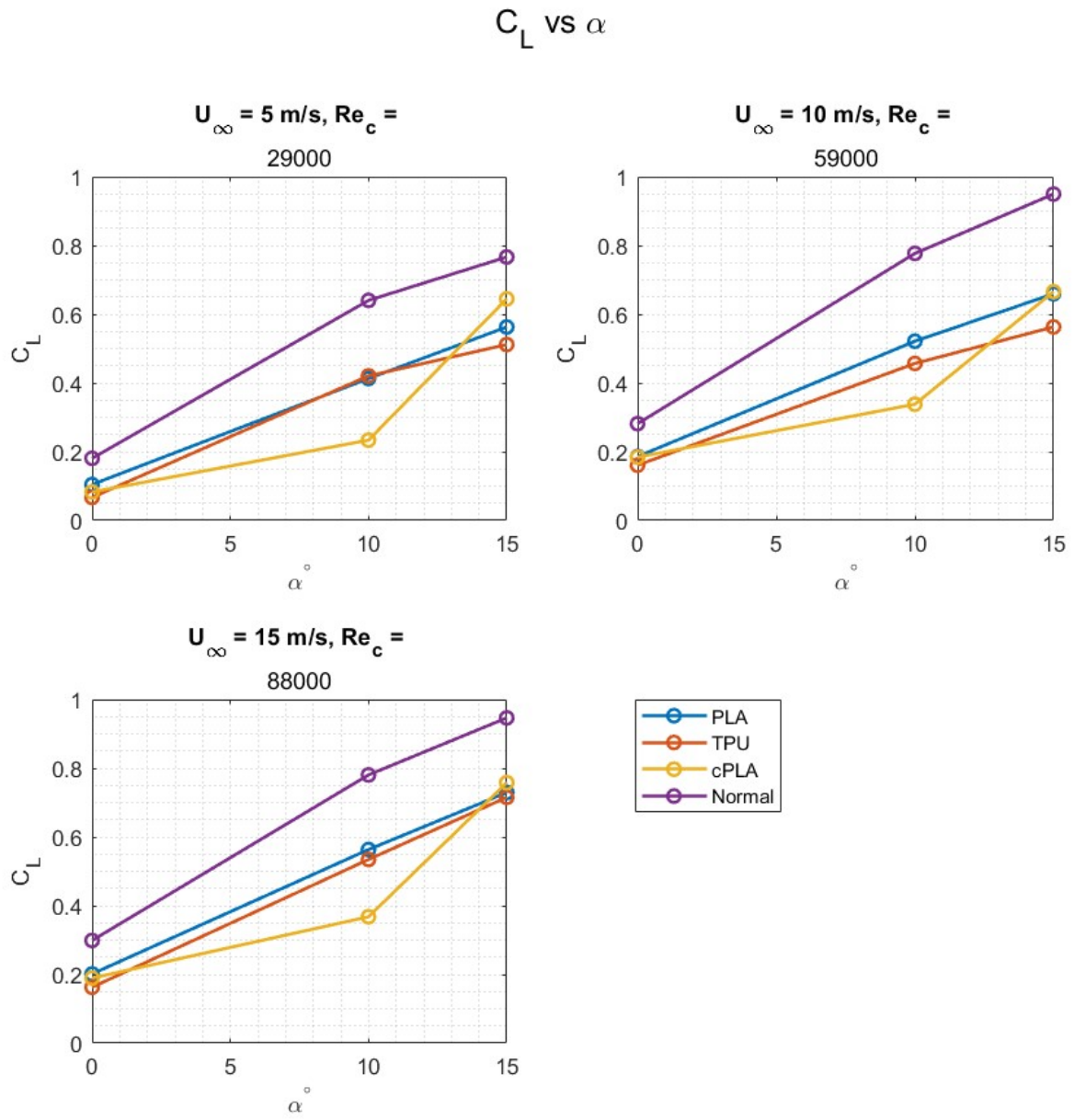

Figure 4.18: Coefficient of lift of wing vs α with different winglets

The C_{L_α} plot can be seen in Figure 4.18 to increase for all materials in an almost linear fashion. Except at $\alpha = 5°$, the C_L values of $norm$ is the highest at all the angles of attack. At a very low Reynolds number flow at $U_\infty = 5m/s$, at a very high angle of attack of $\alpha = 15°$, it can be noticed that the most rigid winglet $cPLA$ has the highest C_L values among the slotted winglets, and is at a 16% lower value than $norm$. It has to be noted that $cPLA$ was the lowest out of all the winglets at $\alpha = 10°$, whereas the flexible winglets TPU and PLA were almost equal. PLA was 33 % in C_L than $norm$ at $\alpha = 15°$, while TPU was the lowest at a 26.5% lower value than $norm$.

Looking at the case of $U_\infty = 10m/s$, the slotted winglets have moreover equal C_L values at $\alpha = 0°$. At an α of $10°$, $cPLA$ is the lowest again with a C_L 56% lesser than that of $norm$. PLA has the highest C_L value amongst the slotted winglets being 33% lower than $norm's$ value, while TPU is intermediate with a 41% lower $C_L$than $norm$.

However, at a higher angle of attack of $\alpha = 15°$, $cPLA$ is slightly higher than PLA in terms of C_L and is more notable at $U_\infty = 15m/s$. Other than this, the slotted winglets followed the same trend at $U_\infty = 15m/s$, however, they were much closer in terms of C_L at $\alpha = 10°$. $norm$ is followed by $cPLA$ with the highest C_L among the slotted winglets with a 30% lower C_L than norm, which is closely followed by PLA and TPU is at the lowest with a 40% lower C_L than $norm$.

To summarize the important inferences from the lift related plots, overall $norm$ performs the best in terms of C_L, while the slots seem to have a negative impact on the lift. Amongst the slotted winglets the most rigid $cPLA$ with an $EI_0 = 30.6 \times 10^{-3}$ seems to perform better at $\alpha = 15°$ but poor at $\alpha \leq 10°$, on a relative scale. The flexible winglets TPU and PLA, despite a 63% difference in EI_0 seems to produce similar values of C_L in general across $\alpha = 10°$ and $\alpha = 15°$. The case of $\alpha = 5°$ was neglected in this subsection due to its highly inconsistent results.

4.4.2. Total drag of wing

Let us now look at the total drag generated by the wing model under different conditions. As can be noticed from Figure 4.19, the total drag of the wing with the winglet seems to be moreover invariant for a change in the chordwise Reynolds number Re_c, in this low Reynolds number regime. Although the number of data points is relatively low, a deeper analysis of the total drag plots is presented in this subsection.

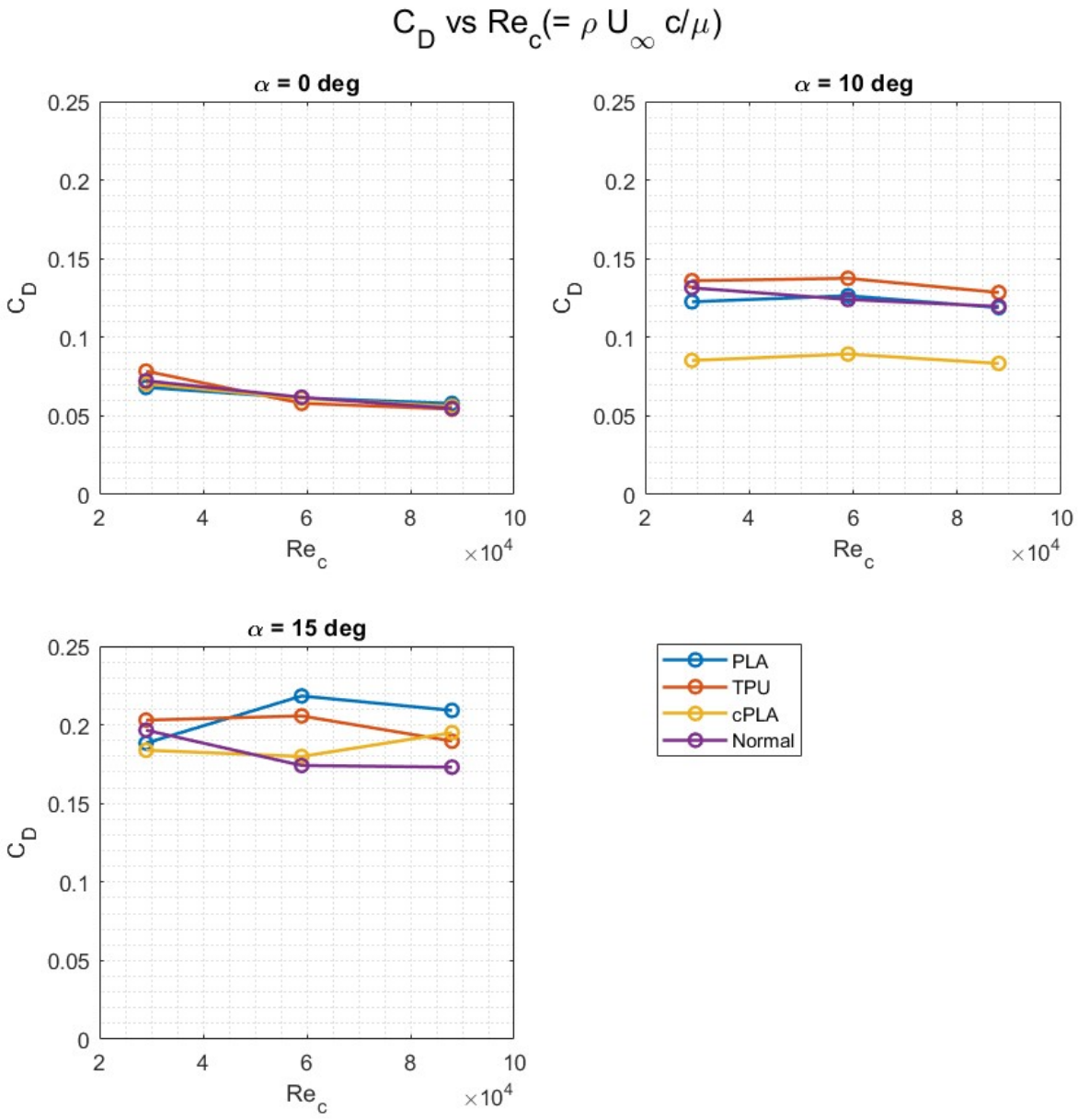

Figure 4.19: C_D vs Re_c of wing vs Re_c for different winglets

Firstly, it is significantly notable in Figure 4.19 that the drag-wise aerodynamic performance of all the winglets are almost the same at $\alpha = 0°$, particularly at $Re_c = 8.8 \times 10^4$. This could be due to the fact that the flow streamlines are barely affected by the slots at the higher Re_c due to a higher momentum in the flow, since the angle of attack is zero. However, a slightly higher lift (C_L) for $norm$ suggests that it is only the total drag that is unaffected, which in

turn implies that the profile drag is unaffected as the magnitudes of induced drag are quite low at $\alpha = 0°$. Therefore, $norm$ has a higher C_L for the same C_D at $\alpha = 0°$, which makes it evident that the lift-to-drag ratio is also higher for $norm$. This will be later discussed in subsection 4.4.4.

The more interesting aspect of this analysis is at the higher angles of attack. At $\alpha = 10°$, it can be noticed that $cPLA$ has the lowest C_D values across the Re_c range, while the most flexible TPU has the highest. Surprisingly, PLA had C_D values almost equal to that of $norm$. Note that the C_D values of $cPLA$ was at least 30 % lower than the rest of the winglets. However, at $\alpha = 15°$, the unslotted $norm$ winglet seemed to have a lower total drag C_D, particularly at higher Re_c in the observed range. While $cPLA$ has the lowest C_D and TPU has the highest C_D at the lower $Re_c = 2.9 \times 10^4$, at $Re_c = 8.8 \times 10^4$, $norm$ has the least coefficient of drag and PLA has the highest. At the higher Re_c, C_D of TPU is 9.5% higher than that of $norm$, $cPLA$ is 7% higher and PLA is 17 % in C_D than $norm$.

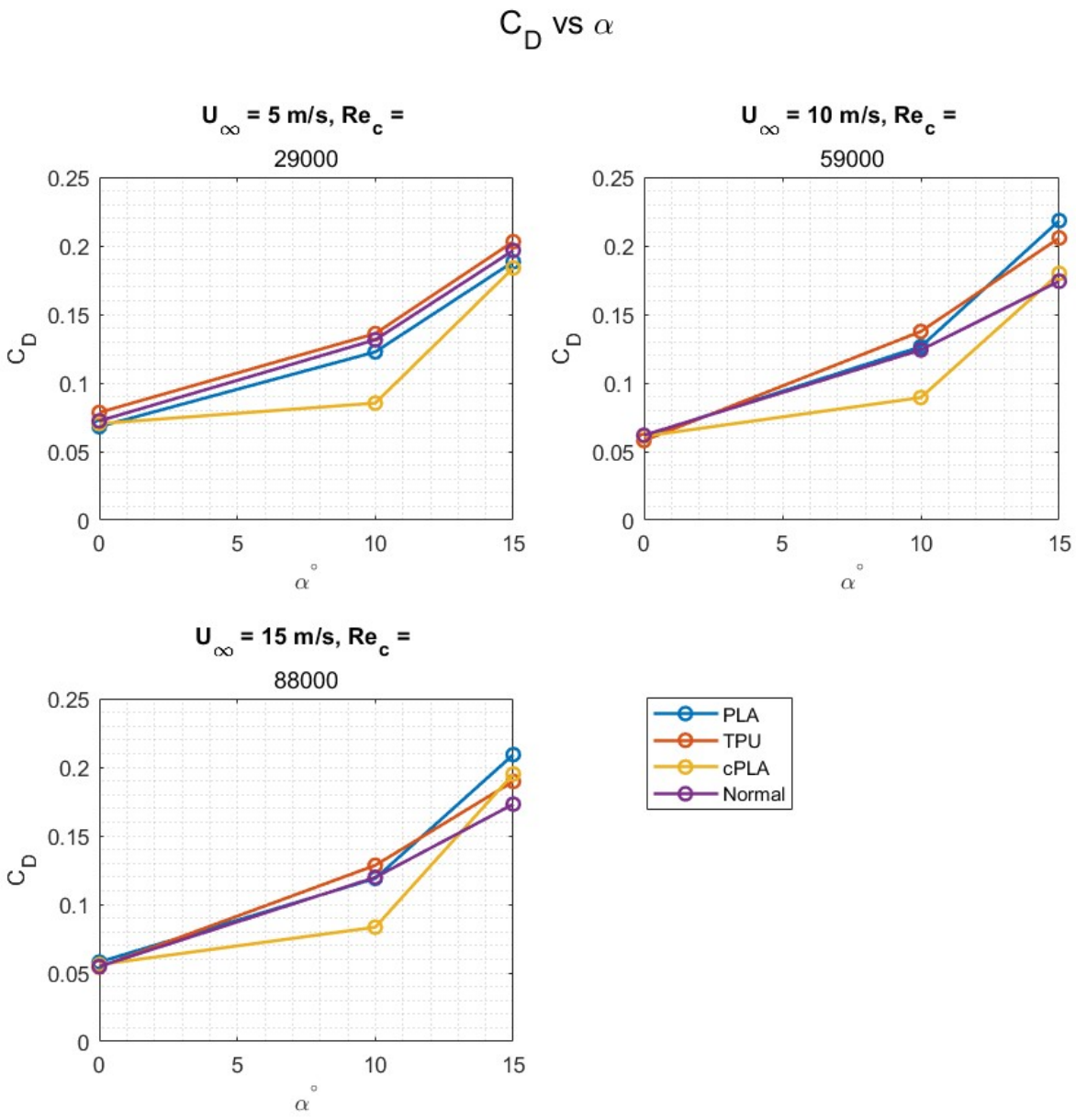

Figure 4.20: Coefficient of drag of wing vs α for different winglets

Figure 4.20 depicts the C_{D_α} curves for the different winglets at different Reynolds numbers. As expected, the C_{D_α} increases in an almost parabolic fashion (note that there are only 3 data points, hence the curve is discrete). It is evident that although C_D is highly comparable for the different winglets at $\alpha = 0°$, as the α increases the difference in C_D becomes significant between the different winglets. Contrary to what was expected, at $\alpha = 10°$, C_D of PLA and $norm$ appear to be almost similar at both $Re_c = 2.9 \times 10^4$ and $Re_c = 8.8 \times 10^4$. At $\alpha = 10°$, $cPLA$ appears to

have the least total drag coefficient while TPU appears to have the highest but comparable C_D values on a relative note with the other winglets. However, the trend changes at $\alpha = 15°$. At higher angle of attack, as inferred from Figure 4.20 previously, $norm$ winglet seems to have the lowest drag coefficient.

4.4.3. Wake Integration based drag estimations

How has the breakdown of the tip vortex affected the aerodynamic drag of our model? Following the wake integral approach from subsection 3.2.3 and using (Equation 3.19), the various components of drag have been estimated and plotted in Figure 4.21.

Note that the profile drag plot (hence total drag as well) depicted in this subsection, and in Figure 4.21a, Figure 4.21b and Figure 4.21c are that of the winglet only, as they were estimated based on the PIV data on the wake plane directly behind the winglet. However, since induced drag is associated with a sudden and steep gradient in pressure (i.e., pressure imbalance between upper and lower wing surfaces) which occurs only at the wingtip [2], the induced drag estimations can be considered to be roughly that of the entire wing.

The analysis was conducted at $U_\infty = 10m/s$ and $Re_c = 5.9 \times 10^4$. It is essential to note that the data used for these plots are from Plane 2, which is at a distance of $x/c \approx 2.3$ from the trailing edge of the winglet. Considering the flow quality in the open-jet tunnel, the ideal plane that could be utilized for the wake integral approach would be Plane 3. However, due to time constraints, data couldn't be obtained at every angle of attack and the obtained data wasn't enough to produce comprehensive conclusion. Despite this, plane 2 data was still valid in the context of the trend observed in the drag component plots.

Winglet	**% Error: $(P3 - P2)/P3$**		
	C_{D_i}	C_{D_p}	$C_{D_{tot}}$
TPU	2.26	15.3	14.25
PLA	1.85	31.03	26.78
cPLA	0.99	11.85	10.57
Normal	5.34	27.15	16.04

Table 4.2: Difference in drag components estimated at Plane 2 ($x/c = 2.3$) and Plane 3 ($x/c = 4.6$)

The values from Plane 2 ($x/c \approx 2.3$) were indeed compared against the much farther downstream plane 3 at ($x/c \approx 4.6$) in order to check for the validity of the far-field assumption as mentioned in subsection 3.2.3. The validation was done with available data at $\alpha = 10°$ and $U_\infty = 10m/s$. The error between the two data have been quantified in Table 4.2. It can be noted that the maximum error in C_{D_i} was 5 %, which seems to be reasonable to produce a legitimate inference. However, the maximum errors in C_{D_p} and $C_{D_{tot}}$ were around 31% and 27 % and this deems the profile and total drag results to be inaccurate, magnitude-wise. it is highly likely that the assumption of the static pressure in the wake has not yet reached the freestream value (i.e., $p \neq p_\infty$) at Plane 2. The following inferences on these parameters will be made based on the observed trend or relative evaluation only, and not based on the actual values.

One general observation was that the induced drag clearly increases with increasing angle of attack, irrelevant of having or not having slots, and the same goes for profile drag (with an exception for $norm$) and total drag as well. At $\alpha = 0°$, the profile drag makes up for 90-98 % of the total drag, while this percentage reduces as we go to $\alpha = 10°$ and $\alpha = 10°$. The contribution of induced drag to the total drag is much higher for the unslotted $norm$ wingtip than it is for any of the slotted winglet, especially at higher angles of attack. An interesting observation is that the profile drag of $norm$ at $\alpha = 15°$ was lower than its induced drag. C_{D_p} was only 37.93% of the total drag while induced drag made up the rest, and was lower than its C_{D_p} at $\alpha = 0°$. This was however not the case with the slotted winglets, and were in the range of 85-92% of the total drag.

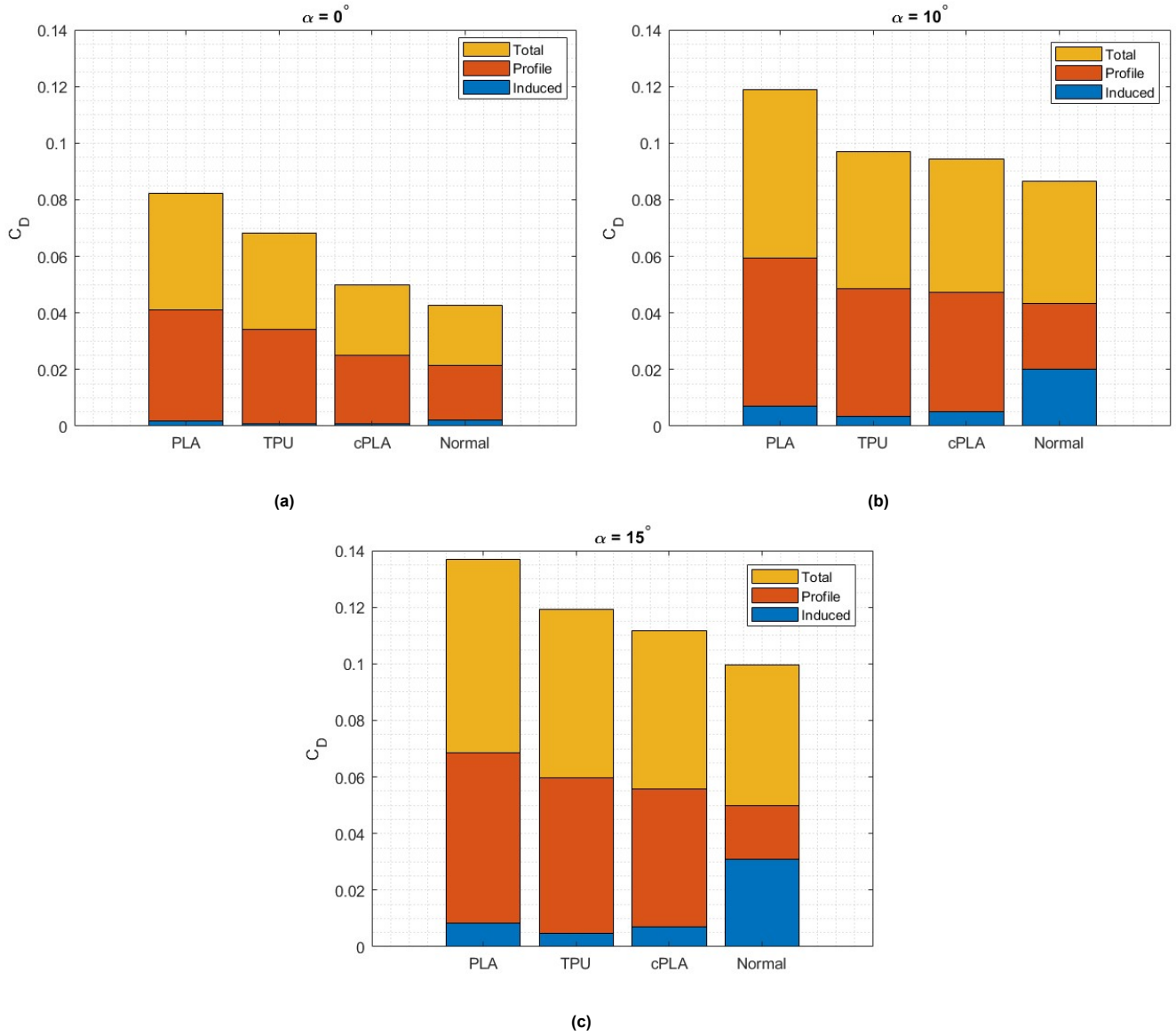

Figure 4.21: Components of drag measured using a far-field wake integral approach on Plane 2 $(x/c \approx 2.3)$ data, $U_\infty = 10m/s$

Agreeing precisely with previous researchers, it is evident from Figure 4.21a,Figure 4.21b and Figure 4.21c that the breakdown of tip vortices indeed mitigates the induced drag of the bio-inspired wing-winglet model. The reduction in induced drag by the slotted wingtips is relatively lower at $\alpha = 0°$ (refer Figure 4.21a), with PLA being around 9 % lower than norm, $cPLA$ 58 % lower, and TPU being 68% lower than $norm$. However, the induced drag coefficient of $norm$ seems to significantly increase at higher angles of attack. Among the slotted winglets, correlating with the net circulation and vorticity observations in subsection 4.3.4, TPU has the lowest C_{D_i} value across the analysed angles of attack, followed by $cPLA$ and PLA. At $\alpha = 10°$ (refer Figure 4.21b), PLA is 65% lower in C_{D_i}, followed by $cPLA$ at 75% lower value and TPU at a notable 83% lower value. Even higher is the difference between the C_{D_i} values at $\alpha = 15°$ - PLA is 73% lower, $cPLA$ is 78% lower while TPU is 84% lower than $norm$. This leads us to a conclusion that flexibility of the wingtips, in terms of EI_0, aids the reduction of induced drag by the slotted winglets.

On the other hand, the profile and total drag values of the slotted winglets are higher when compared to the unslotted winglet and flexibility deteriorates these drag components even further. This is also in support of literature data from Withers [56], partially at least, as it stated that with higher flexibility comes higher profile drag. PLA was having the highest profile and total drag, closely followed by TPU. $cPLA$ was next and $norm$ was the least. $PLA's$ profile drag was a little more than 200% that of $norm's$ at $\alpha = 0°$, while TPU and $cPLA$ were 170% and 240% greater respectively. From Figure 4.21b and Figure 4.21c it is clear that $norm$ outshines the slotted winglets at higher angles of attack by a good margin. At $\alpha = 15°$, C_{D_p} of PLA was more than 300% that of $norm$, whereas TPU and $cPLA$ were 290% and 260% of $norm$. Since profile drag had the major contribution towards total drag in almost all cases, the total drag of the winglets followed a similar trend. The only difference was at $\alpha = 15°$, where PLA, TPU and

$cPLA$ were more comparable with $norm$ with their C_{D_p} values being 140%, 120% and 110% of $norm$.

Now, the above mentioned inferences can be correlated from that of subsection 4.4.2 and we can conclude that at both lower and higher angles of attack, the decrease in induced drag by the wingtip slots is being overpowered by an increase in profile drag, thus leading to a higher total drag and deeming the slots ineffective.

Bending effect on drag components

The calculated vales of flexural rigidity and young's modulus of the different winglets have been depicted along with the drag components in Table 4.4. As can be inferred from the table, the most flexible TPU has the lowest induced drag and total drag. $cPLA$, the least flexible winglet with almost 18 times higher EI_0 than TPU, stands at the second lowest with induced and total drag, while PLA seems to be the intermediate one. Evidently, no associated trend that could possibly link the flexural rigidity to the drag component values were observed. It is necessary to have more data points, i.e., more winglets with different material and/or varying thickness in order to analyse and properly quantify the effect of the flexural rigidity on the drag components.n

However, interestingly just considering the material property that defines flexibility - young's modulus E, it can be noticed that the induced drag C_{D_i} is the lowest for the most flexible winglet TPU, almost 50 % lower than the 49 times more rigid (in terms of E) PLA and 67.5% lower than the 18 times more rigid $cPLA$.Another minor observation was that the profile drag values were much closer for all three winglets, with a difference of just 3% between PLA and TPU, and 6 % difference between PLA and $cPLA$. Note that EI_0 of PLA is 2.7 times that of TPU and $cPLA's$ EI_0 is 6.6 times that of PLA. It could thus be inferred that the geometry (including wetted area) has the most impact on the profile drag, than the thickness or the flexibility of the material.

	$\boldsymbol{EI_0(Nm^2)}$	$\boldsymbol{E(MPa)}$	$\boldsymbol{C_{D_i}(\times 10^{-4})}$	$\boldsymbol{C_{D_p}(\times 10^{-4})}$	$\boldsymbol{C_{D_{tot}}(\times 10^{-4})}$
TPU	1.70E-03	48.71	33.93	390.16	424.09
PLA	4.66E-03	2399.29	68.48	400.84	469.32
cPLA	3.06E-02	2190.69	50.26	376.34	426.60

Table 4.3: Variation of drag components with flexural rigidity and young's modulus; $\alpha = 10°$, $U_\infty = 10m/s$

Table 4.4: Variation of drag components with flexural rigidity (EI_0) and young's modulus (E); $\alpha = 10°$, $U_\infty = 10m/s$; Plane 3 ($x/c = 4.6$)

4.4.4. Lift-to-Drag ratio

Finally, let us look at the overall aerodynamic performance characterized by the C_L/C_D ratio generated by the wing with different winglet configurations.

At this point it is quite evident that under the low Reynolds number regime that was tested, the unslotted $norm$ winglet has a better aerodynamic performance compared to both rigid and flexible slotted winglets. It can be noticed in Figure 4.22 that $(C_L/C_D)_{max}$ for all the winglets occur at $\alpha = 10°$, with the exception of $cPLA$ at $U_\infty = 5m/s$. However, the level of uncertainty is high at such low Reynolds numbers due to the dominance of turbulent fluctuations and viscous effects, and is thus excluded from analysis.

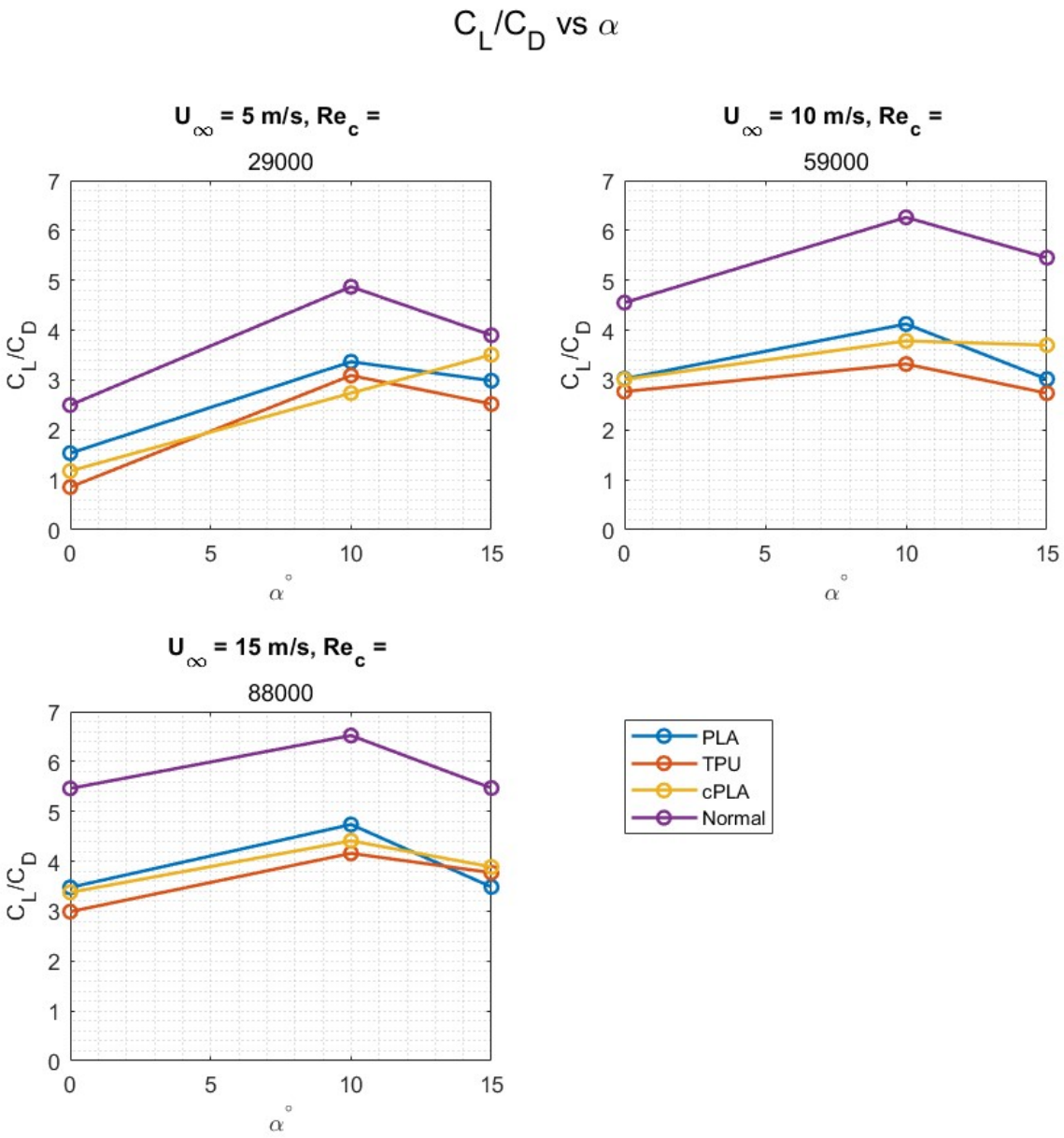

Figure 4.22: C_L/C_D ratio of wing vs α for different winglets

Inferring from Figure 4.22, at $U_\infty = 10m/s$ and $\alpha = 10°$, the $(C_L/C_D)_{max}$ of $norm$ is the highest at a value of 6.26, followed by $cPLA < PLA < TPU$. The $(C_L/C_D)_{max}$ ratio of $cPLA$ is 34% lower, while PLA is 40% lower and TPU is 47% lower. At $\alpha = 15°$, the trend remains the same with $norm$ having C_L/C_D ratio of 5.45. The same ratio for $cPLA$ is 32% lower than that of $norm$, PLA is 45% lower while TPU is almost 50% lower.

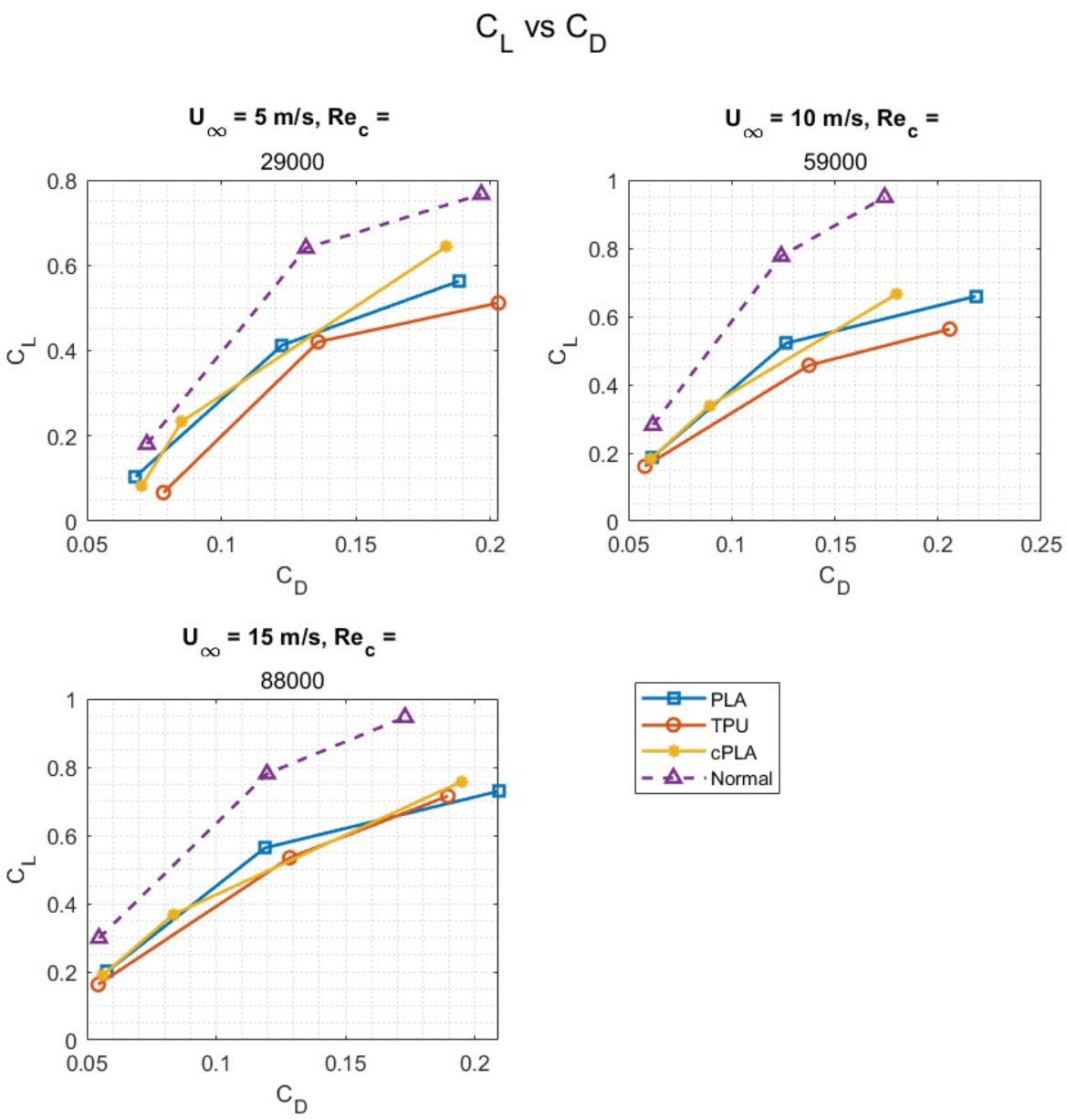

Figure 4.23: C_L vs C_D of wing with different winglets

The C_L vs C_D polar is depicted in Figure 4.23. Again, since there are only three data points, the curve is moreover discrete. However, it can be inferred that the slope of the curve is positive and non-linear. In general,it can be noticed that the slope of the C_L vs C_D curve is more steep for $norm$ than the slotted winglets in the entire Re range.

4.5. Uncertainty quantification

4.5.1. Uncertainty in PIV

In PIV, multiple parameters including particle image size, intensity and density, turbulent fluctuations, velocity gradients, noise level and interrogation window size, affect the uncertainty, as depicted in Figure 4.24. Despite the use of multiple tools to reduce the uncertainties such as the vectoring filtering, some still persist.

The peak ratio (ratio between the highest correlation peak and the second highest correlation peak), is a good measure of uncertainty [10] and the peak ratio for the PIV experiments were constantly between a range of 62-72.

One of the primary causes of random errors are the cross-correlation uncertainty and the turbulent fluctuations in the freestream velocity [45]. The ensemble size was relatively high at $N = 500$, and this helps in reducing the random uncertainties through better averaging, as the uncertainties reduce by a factor of $\sqrt{N}$. The turbulence level in the tunnel is said to be low, and it was assumed that the freestream turbulence is somewhere below 1%, however the deviations in the freestream velocity was around 4.5 % when measured with PIV.

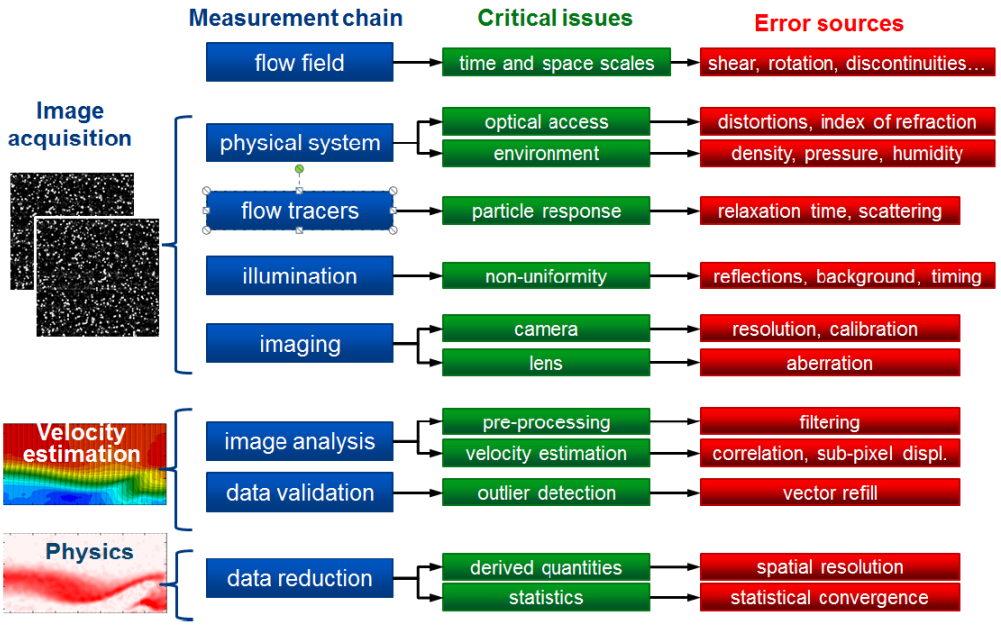

Figure 3.1. Overwiew of PIV error sources (courtesy of A. Sciacchitano, TU-Delft).

Figure 4.24: PIV uncertainty - sources of errors (*Courtesy of A. Sciacchitano, TU Delft* [55])

The most relevant sources of systematic uncertainties in the PIV measurements are considered to be peak locking, inaccurate image combination, lack of spatial resolution, particle tracers slip and aero-optical aberration [45]. The latter two effects can be neglected since the flow is at low-speed and since the tunnel was open-jet. To avoid significant bias errors due to peak locking it is important to have a particle image diameter of at least two pixel [44]. Smaller sizes usually appear in the case of low optical magnification or for camera sensors with large pixel spacing, which is typical for some high-speed cameras. In our case, the particle diameter fromt he smoke is around $2\mu m$. The spatial resolution has been quantified through the Dynamic Spatial Range (DSR), defined as the ratio between the sensor size (in pixels) to the interrogation window size [1], as mentioned in Table 4.5. Patently, a value of $DSR = 213$ is quite sufficient for lowering the uncertainties [44].

Error	Uncertainty	Error estimator	Error quantity	Relative velocity uncertainty % (u/U_∞)
	Cross-correlation	Max stereo reconstruction error	$0.6295m/s$	≤ 6
Random	Turbulent velocity fluctuations	$\sigma_{u_{max}}/\sqrt{N}$	$\sigma_{u_{max}} = 1.4m/s$	≤ 6.3
Systematic	Peak locking	$d_\tau/\Delta_{px} M\Delta t$	$0.03px - 0.09px$	≤ 2
	Spatial resolution	$DSR = x_{max}/D_I$	213	$<< 1$

Table 4.5: Uncertainties in PIV

4.5.2. Uncertainty in force balance data

The wind tunnel testing data from the force balance appeared to have a significant amount of uncertainty. The following were the possible sources of the uncertainty in measurement:

- Turbulent fluctuations in freestream
- Force transfer from the wing to the balance
- Accuracy of load cells in the balance
- Lack of boundary corrections
- Human errors
- Random errors

The level of turbulence in the freestream was moreover unknown, especially considering that the tunnel was used as an open-jet. The wing-winglet was mounted on the mounting table using a rod passing through the quarter chord approximately and the base of the wing was tightened to the mounting table. There is a possibility that the aerodynamic force transfer from the wing-winglet model to the balance was inefficient. Additionally, the accuracy of the load cells that measure the aerodynamic loads were not tested.

There was no boundary corrections applied due to a lack of necessary data and time. The wake blockage and the buoyancy corrections can be neglected since the tunnel is used as an open-jet. However, the cameras were mounted behind the model and therefore were present in the freestream, although at a distance of $x/c > 5$ from the trailing edge of the model. The correction for solid blockage was required, however weren't made. Information on constants such as body shape factor K_1 for estimating the solid blockage wasn't available for the currently used slotted winglets.

In order to obtain a rough picture of how much the uncertainty in the force balance data is, the instantaneous data from the force balance measurements were utilized. Recorded as $.tdms$ files, the instantaneous load cell readings over a time span of 10 sec was used to calculate the mean and standard deviation statistics. The calculated standard deviations were plotted to check how close they're to a gaussian distribution. The gaussian distributions of the force balance load cell data for the TPU winglet at $U_\infty = 10m/s$ have been depicted in Figure 4.25 and Figure 4.26. As can be seen in Figure 4.25, the load cell 3 has a very broad distribution of the measurements and has a relatively flatter peak. This indicates that the instantaneous measurements of drag (load cell 3 captures the drag force) are far away from the mean value, hence indicating a certain level of fluctuation in loads. It was therefore regarded that the data from $\alpha = 5°$ is unusable. However, the same load cell 3 bell-curve for $\alpha = 10°$ appears to be more narrow than the case of $\alpha = 5°$. Note that the drag force measurements are indeed lower than the lift ones, and hence the peak of load cell 3 is lower compared to that of load cell 1 and 3.

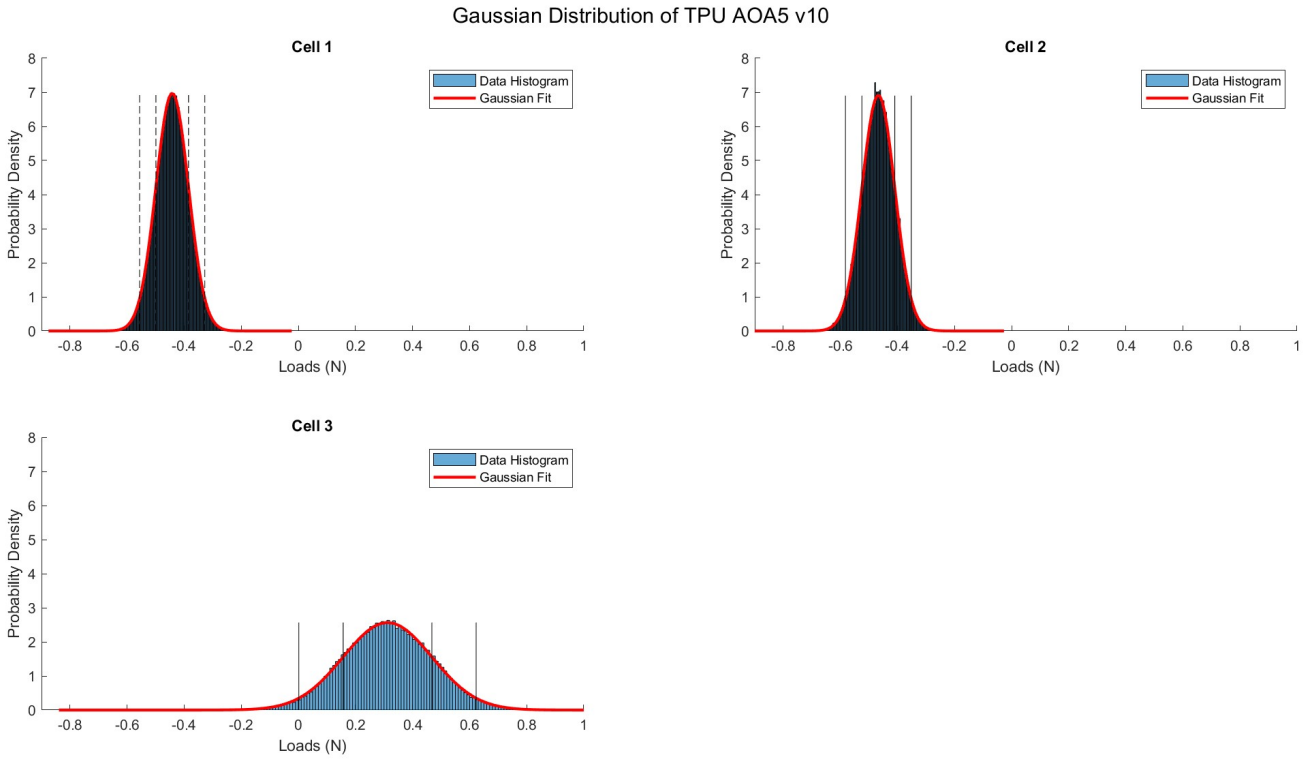

Figure 4.25: Gaussian distribution of TPU winglet loads from force balance; $U_\infty = 10m/s$; $\alpha = 5°$

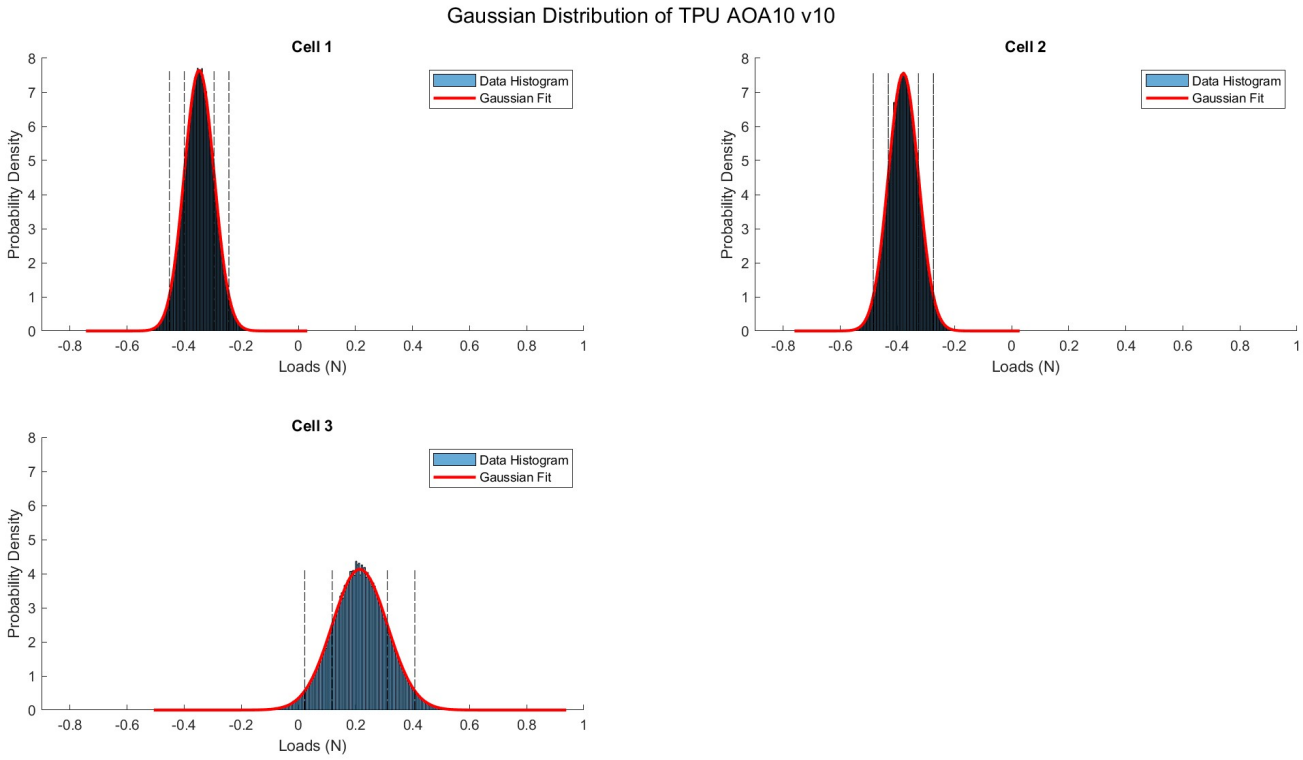

Figure 4.26: Gaussian distribution of TPU winglet loads from force balance; $U_\infty = 10m/s$; $\alpha = 10°$

4.6. Vortex wandering

One highly noticeable phenomenon from the averaged v velocity contours Figure 4.8 is vortex wandering. Vortex wandering is defined as the low-frequency coherent side-to-side motion of the trailing vortex in the surrounding flow and can be measured by the instantaneous vortex core locations in the field [12]. The instantaneous core locations were detected by utilizing the peaks in the Q-criteria plots. However, it was noticed that most of the tip vortex cores of the slotted winglets are diffused or not detectable. Only the topmost peak in the Q-criterion was easily obtained (corresponding to $T2$) whereas the other peaks could not be distinguished.

Due to time constraints, only one particular case was analyzed. The topmost peak in the Q-criteria field of $cPLA$, indicating the vortex core location of the $T2$ wingtip at $U_\infty = 10m/s$ and $\alpha = 10°$ has been plotted in Figure 4.27. Note that the PIV data is not time-resolved, and the instantaneous core locations plotted in Figure 4.27 are from the each of the 500 images captured over a time span of 10 seconds.

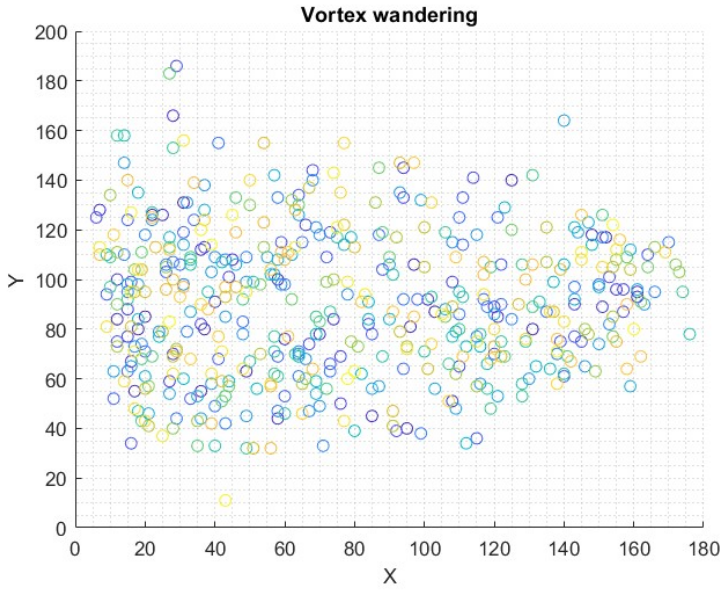

Figure 4.27: Vortex wandering of $T2$ tip vortex of $cPLA$; $\alpha = 10°$;$U_\infty = 10m/s$

It can be noticed that the core locations are all over the planar field. This indicates a high level of vortex wandering. The possible reasons could be mild vibrations of the wingtip, turbulence in the flow, flow separation and reattachment, *etc*. The dynamic behaviour of the tip vortices, i.e., the way it displaces in the wake is an interesting topic for future research, especially considering the multiple wingtips in the slotted winglets.

5
Conclusion

5.1. General notes

The thesis explored the phenomenon of tip vortex mitigation using slotted and flexible winglets both from a qualitative and a quantitative perspective. The wingtip bending of the individual tips were tracked, the stiffness of the wingtips were quantified using flexural rigidity and a brief 2D (planar) wake analysis was conducted using stereo-PIV. The vortex breakdowns by the wingtips were visualized, and the most significant vortex cores were identified.

It was realized that the slots indeed reduce the circulatory strength of the tip vortex and distributes them in the wake. Further, the flexibility (or stiffness) of the wingtips were correlated with the tip vortex breakdown, and their impact on the drag and net circulation were analysed.

Overall, it can be summarized that the unslotted $norm$ winglet has a better aerodynamic performance compared to the slotted winglets. It has a notable edge over the other winglets with the amount of lift it produces at different angles of attack and at different Reynolds numbers at low speed regime. Although slots do reduce the induced drag by breaking down the tip vortex and distributing its circulatory strength, the increase in profile drag (for the models used in this thesis) appears to overpower the induced drag mitigation. Hence, the total drag appears to increase more even at higher angles of attack where induced drag is significant.

Flexibility seems to aid the aerodynamic performance in general, and helps in reducing. All throughout the quantitative part of section 4.3, it can be noticed that $cPLA$ has a slightly better performance at very low Re_c and high α. This possibly implies that a rigid slotted winglet can produce a higher $(C_L/C_D)_{max}$ under very low Reynolds numbers, compared to a non-slotted or a flexible slotted winglet, and can postpone stall. This is in contrast to the inferences from the literature such as KleinHeerenbrinck's results [33] where they had mentioned that during flapping the outboard sections of a bird's wing experience an increased effective angle of attack and hence higher drag, which can be mitigated by aeroelastic twist of the individual tip feathers. Perhaps the twisting capability of the current models aren't sufficient to produce this effect. Therefore, the aforementioned hypothesis further needs to be tested out.

5.2. Research questions

5.2.1. Drag reduction:

1. **Do slots reduce induced drag and do flexible wingtips reduce it further?**
   Yes, slots do reduce the induced drag by upto 84%, and this aligns with the available literature data [40] [33] [15] [56] [51]. From the present thesis, it can be concluded that the role of flexibility is positive as the highly flexible TPU winglet has the lowest induced drag, followed by the intermediate PLA while the rigid winglet $cPLA$ has the highest among the three slotted winglets.
2. **Is this valid across a range of angles of attack?**
   The reduction in induced drag was noticed at all the angles of attack in the range, and the above statement about flexibility also held true for these angles of attack, including $\alpha = 0°$ where induced drag is very small.
3. **Is the total drag also reduced (or) is the reduction is induced drag compensated by an increase in profile drag?**
   Although the slotted winglets reduced the induced drag by upto 84%, the reduction is overshadowed by a larger increase in profile drag (going upto 200% higher). This is valid at a high angle of attack of $\alpha = 15°$ as well, where the induced drag is supposed to be equally dominant.
4. **How sensitive is this phenomenon to Reynold's number in the low-speed regime?**
   The total drag did not seem to vary significantly with a change in Reynolds number, within the tested low speed (Re_c) regime.

5.2.2. Aerodynamic efficiency:

1. **Do the slots improve aerodynamic performance? How about flexibility?**
   No, the $norm$ winglet has a higher C_L/C_D ratio than the slotted winglets, and the $(C_L/C_D)_{max}$ of the slotted winglets is atleast 34% lower than $norm$. The aerodynamic performance of PLA was the best among the slotted winglets. This brings us to a conclusion that flexibility shouldn't be too high nor too low for the best C_L/C_D ratio, and perhaps an optimization study is required. Additionally, it has be mentioned that the force balance results were not entirely accurate and hence requires a re-evaluation due to multiple uncertainties mentioned in subsection 4.5.2.
2. **Does flexibility in slotted wingtips improve $(C_L/C_D)_{max}$ by reducing the effective angle of attack?**
   No, the $(C_L/C_D)_{max}$ reduced opposing to what was expected. The effective angle of attack appears to have increased by then bending of the wingtips, and $(C_L/C_D)_{max}$ occurs at at $\alpha = 15°$ in most cases, and the ratio decreases at a higher angle of attack. However, as mentioned previously in section 5.1, the rigid winglet $cPLA$ appears to have a $(C_L/C_D)_{max}$ at $\alpha = 15°$ at a very low Reynolds number $Re_c = 2.9 \times 10^4$.
3. **Do slots only increase the total lift through an increase in surface area, or does it actually improve C_L?**
   The slots do not increase the C_L of the entire wing, in the tested models. This is in contradiction to the works of [33], however, it is to be noted that the testing conditions were quite different and an actual bird was subjected to testing instead of a bio-mimicked model. This brings us to a question of if the models used in the current thesis work were not very comparable to birds wings, in terms of the geometry and flexibility characteristics of the wingtips (or feathers).

5.2.3. Vortex characterization:

1. **How does tip vortex breakdown & dissipation look like? Are the vortex cores distinct and notable?**
   Please refer to subsection 4.3.1 and section 4.2 for visualization of the tip vortex breakdown. As expected, the cores become noticeable at $\alpha = 10°$, especially int he case of slotted winglets. There are maximum 3 vortex cores notable or distinct for the slotted winglets, however they are partially or highly diffused. The $T2$ tip cores are prominent for PLA and $cPLA$ at $\alpha = 10°$, whereas the core is relatively diffused particularly for TPU at the same α. Ont he other hand, the cores are significant for all the slotted winglets at $\alpha = 15°$.
2. **Are the slots reducing the strength of the tip vortex?**
   Yes, in general the slotted wingtips appear to reduce the net circulation in the captured wake plane. The reduction is 37-47% at $\alpha = 0°$, 12-35 % at $\alpha = 10°$ while the data at $\alpha = 15°$ is inconclusive.
3. **Vortex wandering effect - how does the vortex core displacement look like?**
   The wandering effect is highly noticeable (refer section 4.6), however more sophisticated post-processing algorithms are required to obtain the instantaneous core locations of all the 5 tip vortices. Perhaps most of the cores are too diffused for any algorithm to detect or distinguish.

5.3. Future recommendations

A persisting question is how precise and accurate can one bio-mimic bird wings to achieve an equivalent performance gain. Clearly, the models in the present thesis did not achieve the expected performance gains produced by an actual bird wing in soaring/gliding flight. And the wing was not tested out in the Reynolds number regime of real-flight. Additionally, it has to be noted that the wind-tunnel flow quality was low in our case, and that the test conditions were not the same as in the literature. The following are the future recommendations proposed for this field of research:

- Further test out different materials and wing geometries, and perform an optimization study particularly on the effect of flexibility parameters to understand what we are missing in terms of bio-mimicking actual bird wings.
- Build a bigger wind-tunnel model to test out at a Reynolds number comparable to real-flight, so that we can evaluate the advantage of these slotted winglets with or without flexibility, if utilized in airplanes.
- The planned next step in the field of slotted winglets is to test the winglet out in flapping flight. A hypothesis that the author proposes is that perhaps the slots are only advantageous in flapping flight and that is what gives birds the aerodynamic advantage. This hypothesis could be extended to newer technologies to power $VTOL$ vehicles (Vertical Take-Off and Landing), to provide them an aerodynamic boost. Flapping flights of birds and insects could possibly be bio-mimicked to provide us a newer dimension in air travel, especially with $VTOL$ aircraft for intra-city commuting.
- As mentioned in section 4.6, an interesting field of research would be to conduct a time-resolved anlaysis to understand the source of the vortex wandering effect, and look at how the vortices evolve over time.
- Reconstruction of the wake topology with multiple merging or dissipating tip vortices using Taylor's hypothesis with time-resolved data.

References

[1] R J Adrian. “Dynamic ranges of velocity and spatial resolution of particle image velocimetry”. In: *Measurement Science and Technology* 8.12 (Oct. 1997), p. 1393. DOI: 10.1088/0957-0233/8/12/003. URL: https://dx.doi.org/10.1088/0957-0233/8/12/003.

[2] John D. Anderson and Christopher P. Cadou. *Fundamentals of aerodynamics*. McGraw-Hill, 2024.

[3] E. W. F. Casimiri B. W. van Oudheusden F. Scarano. “Non-intrusive load characterization of an airfoil using PIV”. In: *Experiments in Fluids (2006) 40: 988–992* (2006). DOI: 10.1007/s00348-006-0149-2.

[4] Thomas Bachmann and Hermann Wagner. “Anatomical, morphometrical and biomechanical studies of barn owls’ and pigeons’ wings”. In: 2010. URL: https://api.semanticscholar.org/CorpusID:54199668.

[5] Martin Berens. “Potential of Multi-Winglet Systems to Improve Aircraft Performance”. PhD thesis. Technischen Universitat Berlin, 2008.

[6] Albert Betz. “A Method for the Direct Determination of Wing-Section Drag”. In: *Technical Memorandum* 337 (1925). URL: https://api.semanticscholar.org/CorpusID:118914658.

[7] Edward F. Blick et al. “Bird Aerodynamic Experiments”. In: *Swimming and Flying in Nature: Volume 2*. Ed. by Theodore Y.-T. Wu, Charles J. Brokaw, and Christopher Brennen. Boston, MA: Springer US, 1975, pp. 939–952. ISBN: 978-1-4757-1326-8. DOI: 10.1007/978-1-4757-1326-8_30.

[8] R. H. Brown. “The flight of birds”. In: *Journal of Experimental Biology* 30.1 (Mar. 1953), pp. 90–103. DOI: 10.1242/jeb.30.1.90.

[9] G. W. Brune. “Quantitative low-speed wake surveys”. In: *Journal of Aircraft* 31.2 (1994), pp. 249–255. DOI: 10.2514/3.46481. URL: https://doi.org/10.2514/3.46481.

[10] John J Charonko and Pavlos P Vlachos. “Estimation of uncertainty bounds for individual particle image velocimetry measurements from cross-correlation peak ratio”. In: *Measurement Science and Technology* 24.6 (Apr. 2013), p. 065301. DOI: 10.1088/0957-0233/24/6/065301. URL: https://dx.doi.org/10.1088/0957-0233/24/6/065301.

[11] Qigang Chen et al. “Comparison of vortex identification criteria for planar velocity fields in wall turbulence”. In: *Physics of Fluids* 27.8 (Aug. 2015), p. 085101. ISSN: 1070-6631. DOI: 10.1063/1.4927647. eprint: https://pubs.aip.org/aip/pof/article-pdf/doi/10.1063/1.4927647/15690324/085101_1_online.pdf. URL: https://doi.org/10.1063/1.4927647.

[12] Zepeng Cheng et al. “Effect of vortex dynamics and instability characteristics on the induced drag of trailing vortices”. In: *Chinese Journal of Aeronautics* 35.9 (Aug. 2021), pp. 160–173. DOI: 10.1016/j.cja.2021.12.012.

[13] Stacey A. Combes. “Wing flexibility and design for animal flight”. PhD thesis. Jan. 2002, pp. 101–103.

[14] Clarence D. Cone. “The soaring flight of birds”. In: *Scientific American* 206.4 (1962), pp. 130–140. DOI: 10.1038/scientificamerican0462-130.

[15] Clarence D. Cone. “Thermal soaring by migrating starlings”. In: *American Scientist* 47 (1959), pp. 180–209.

[16] Victor R. Corsiglia, Vernon J. Rossow, and Donald L. Ciffone. “Experimental Study of the Effect of Span Loading on Aircraft Wakes”. In: *Journal of Aircraft* 13 (1975), pp. 968–973. URL: https://api.semanticscholar.org/CorpusID:109051764.

[17] S. C. CROW. “Stability theory for a pair of trailing vortices”. In: *AIAA Journal* 8.12 (1970), pp. 2172–2179. DOI: 10.2514/3.6083. URL: https://doi.org/10.2514/3.6083.

[18] Greeshma Daniel and Ebenezer P. Gnanamanickam. “Understanding the structure of wing tip vortices of bio-inspired winglets”. In: *AIAA SCITECH 2024 Forum* (2024). DOI: 10.2514/6.2024-2690.

[19] *DaVis 10.2 FlowMaster product manual*. LaVision GmbH.

[20] Prantik Dutta et al. “Aerodynamic analysis of bionic winglet-slotted wings”. In: *Materials Today: Proceedings* 62 (2022), pp. 6701–6707. DOI: 10.1016/j.matpr.2022.04.752.

[21] Prum RO. Feo TJ Field DJ. “Barb geometry of asymmetrical feathers reveals a transitional morphology in the evolution of avian flight”. In: *Proc. R. Soc. B 282:* (2015).

[22] Michael B. Giles and Russell M. Cummings. “Wake integration for three-dimensional Flowfield computations: Theoretical development”. In: *Journal of Aircraft* 36.2 (1999), pp. 357–365. DOI: 10.2514/2.2465.

[23] Sheldon I. Green. *Fluid vortices*. Kluwer Academic, 1995.

[24] Alexander J. Heintz et al. “Influence of Configurational Parameters on the Vortex System of a Rotor in Hover”. In: (). DOI: 10.2514/6.2024-0896. URL: https://arc.aiaa.org/doi/abs/10.2514/6.2024-0896.

[25] J. Hunt, Alan Wray, and Parviz Moin. “Eddies, streams, and convergence zones in turbulent flows”. In: *Studying Turbulence Using Numerical Simulation Databases* 1 (Nov. 1988), pp. 193–208.

[26] Jinhee Jeong and Fazle Hussain. “On the identification of a vortex”. In: *Journal of Fluid Mechanics* 285 (1995), pp. 69–94. DOI: 10.1017/S0022112095000462.

[27] Song Jixiang et al. “Study on drag reduction of flexible structure under flows”. In: *E3S Web of Conferences* 245 (Jan. 2021). DOI: 10.1051/e3sconf/202124501019.

[28] L. C. Johansson and A. Hedenström. “The vortex wake of Blackcaps (Sylvia Atricapilla) measured using high-speed digital particle image velocimetry (DPIV)”. In: *Journal of Experimental Biology* 212.20 (2009), pp. 3365–3376. DOI: 10.1242/jeb.034454.

[29] Joseph Katz and Allen Plotkin. *Low-Speed Aerodynamics*. 2nd ed. Cambridge Aerospace Series. Cambridge University Press, 2001.

[30] Richard Keane and Ronald Adrian. “Theory of cross-correlation analysis of PIV images”. In: *Applied Scientific Research* 49 (Jan. 1992), pp. 191–215. DOI: 10.1007/BF00384623.

[31] Lukas Kilian et al. “Bio-inspired morphing wings: mechanical design and wind tunnel experiments”. In: *Bioinspiration and Biomimetics* 17 (May 2022). DOI: 10.1088/1748-3190/ac72e1.

[32] Marco KleinHeerenbrink. “In the wake of a bird - Quantifying aerodynamic performance of avian flight”. PhD thesis. Faculty of Science, Lund University, 2015.

[33] Marco KleinHeerenbrink, L. Christoffer Johansson, and Anders Hedenström. “Multi-cored vortices support function of slotted wing tips of birds in gliding and flapping flight”. In: *Journal of The Royal Society Interface* 14.130 (2017), p. 20170099. DOI: 10.1098/rsif.2017.0099.

[34] Kazuhiro Kusunose and James P. Crowder. “Extension of Wake-Survey Analysis Method to Cover Compressible Flows”. In: *Journal of Aircraft* 39.6 (2002), pp. 954–963. DOI: 10.2514/2.3048.

[35] Dan Liu et al. “A brief review on aerodynamic performance of wingtip slots and Research Prospect”. In: *Journal of Bionic Engineering* 18.6 (2021), pp. 1255–1279. DOI: 10.1007/s42235-021-00116-6.

[36] Tianshu Liu et al. “Avian Wing Geometry and Kinematics”. In: *Aiaa Journal - AIAA J* 44 (May 2006), pp. 954–963. DOI: 10.2514/1.16224.

[37] E. C. Maskell. “Progress towards a method for the measurement of the components of the drag of a wing of a finite span”. In: *Royal Aircraft Establishment, Technical Report 72232* (Jan. 1973).

[38] Barnes W. McCormick, James L. Tangler, and Harold E. Sherrib. “Structure of trailing vortices.” In: *Journal of Aircraft* 5.3 (1968), pp. 260–267. DOI: 10.2514/3.43936.

[39] Alden Midmer and Christoph Brücker. “Vortex dynamics in the wake of bio-inspired flexible, slotted winglets”. In: *Journal of Fluids and Structures* 128 (2024), p. 104138. ISSN: 0889-9746. DOI: https://doi.org/10.1016/j.jfluidstructs.2024.104138. URL: https://www.sciencedirect.com/science/article/pii/S0889974624000732.

[40] B. G. Newman. “Soaring and gliding flight of the Black Vulture”. In: *Journal of Experimental Biology* 35.2 (1958), pp. 280–285. DOI: 10.1242/jeb.35.2.280.

[41] C. Nithiyapathi, PS. Sreelakshmy, and M. Suman. “Aerodynamic characterization of an Albatross wing for Bio-inspired unmanned aerial vehicle”. In: *Materials Today: Proceedings* 37 (2021). International Conference on Newer Trends and Innovation in Mechanical Engineering: Materials Science, pp. 1659–1664. ISSN: 2214-7853. DOI: https://doi.org/10.1016/j.matpr.2020.07.182. URL: https://www.sciencedirect.com/science/article/pii/S2214785320352755.

[42] F. NOCA and D. SHIELS anad D. JEON. “A COMPARISON OF METHODS FOR EVALUATING TIME-DEPENDENT FLUID DYNAMIC FORCES ON BODIES, USING ONLY VELOCITY FIELDS AND THEIR DERIVATIVES”. In: *Journal of Fluids and Structures* 13.5 (1999), pp. 551–578. ISSN: 0889-9746. DOI: https://doi.org/10.1006/jfls.1999.0219.

[43] Hans Oehme. “On the aerodynamics of separated primaries in the avian wing”. In: *Scale Effects in Animal Locomotion by T. J. Pedley* 4 (1977), pp. 479–495.

[44] Markus Raffel et al. *Particle image velocimetry*. Springer, 2007. DOI: 10.1007/978-3-540-72308-0.

[45] D Ragni et al. “Surface pressure and aerodynamic loads determination of a transonic airfoil based on particle image velocimetry”. In: *Measurement Science and Technology* 20.7 (May 2009), p. 074005. DOI: 10.1088/0957-0233/20/7/074005. URL: https://dx.doi.org/10.1088/0957-0233/20/7/074005.

[46] E. G. Reid. *Applied Wing Theory*. McGraw-Hill, 1932.

[47] Mikael Rosén and Anders Hedenström. “Gliding flight in a jackdaw: a wind tunnel study”. In: *Journal of Experimental Biology* 204.6 (Mar. 2001), pp. 1153–1166. ISSN: 0022-0949. DOI: 10.1242/jeb.204.6.1153. URL: https://doi.org/10.1242/jeb.204.6.1153.

[48] Chang kwon Kang Shyy Wei Hikaru Aono and Hao Liu. “An Introduction to Flapping Wing Aerodynamics”. In: *Cambridge University Press* 37 (2013). DOI: 10.1017/cbo9781139583916.

[49] A. M. O. Smith. “High-Lift Aerodynamics”. In: *Journal of Aircraft* 12 (1975), pp. 501–530. URL: https://api.semanticscholar.org/CorpusID:109188570.

[50] J. J. Spillman. “Wing tip sails; progress to date and future developments”. In: *The Aeronautical Journal* 91.910 (1987), pp. 445–453. DOI: 10.1017/s0001924000050624.

[51] Vance A. Tucker. “Gliding birds: Reduction of induced drag by wing tip slots between the primary feathers”. In: *Journal of Experimental Biology* 180.1 (1993), pp. 285–310. DOI: 10.1242/jeb.180.1.285.

[52] M.F. UNAL, J.-C. LIN, and D. ROCKWELL. “FORCE PREDICTION BY PIV IMAGING: A MOMENTUM-BASED APPROACH”. In: *Journal of Fluids and Structures* 11.8 (1997), pp. 965–971. ISSN: 0889-9746. DOI: https://doi.org/10.1006/jfls.1997.0111. URL: https://www.sciencedirect.com/science/article/pii/S0889974697901110.

[53] Dr. Leo Veldhuis. *Aircraft Aerodynamics Lecture Series*. Faculty of Aerospace Engineering, TU Delft.

[54] J Westerweel. “Fundamentals of Digital Particle Image Velocimetry”. In: *Journal of Bionic Engineering* 8.6 (1997).

[55] B.F.A. Wieneke. “PIV Uncertainty Quantification and Beyond”. PhD thesis. 2017, pp. 33–94.

[56] P. C. Withers. “The aerodynamic performance of the wing in red shouldered hawk buteo linearis and a possible aeroelastic role of wingtip slots”. In: *Ibis* 123.2 (1981), pp. 239–247. DOI: 10.1111/j.1474-919x.1981.tb00933.x.

[57] Philip C. Withers. “An aerodynamic analysis of bird wings as fixed aerofoils”. In: *Journal of Experimental Biology* 90.1 (1981), pp. 143–162. DOI: 10.1242/jeb.90.1.143.

[58] Gang Chen Zhe Hui Yang Zhang. “Aerodynamic performance investigation on a morphing unmanned aerial vehicle with bio-inspired discrete wing structures”. In: *Aerospace Science and Technology* 95 (2022). DOI: 10.1016/j.ast.2019.105419.

6
Appendix

6.1. Material Selection for Winglet

Material	**Abbreviation**	**Young's Modulus (E)**	**3D -printable?**
Balsa Wood	∼	1-10 Gpa	No
Carbon fibre	∼	200 –700 Gpa	No
CFRP	Carbon Fibre Reinforced Polymer	150-300 Gpa	Yes
PETG	Polyethylene Terephthalate Glycol	1711 ± 45 MPa	Yes
TPU	Thermoplastic Polyurethane	56 ± 3 MPa	Yes
PLA	Polylactic Acid	3071 ± 181 MPa	Yes
TPE	Thermoplastic Elastomers	1-50 Mpa	Yes
PBS	Polybutyene Succinate	2.2 - 2.7 Gpa	Yes
cPLA	Carbon-infused PLA	2420 ± 120 MPa	Yes
	Bird feathers (Owl & Pigeon)	6-8 Gpa	

6.2. Averaged velocity components

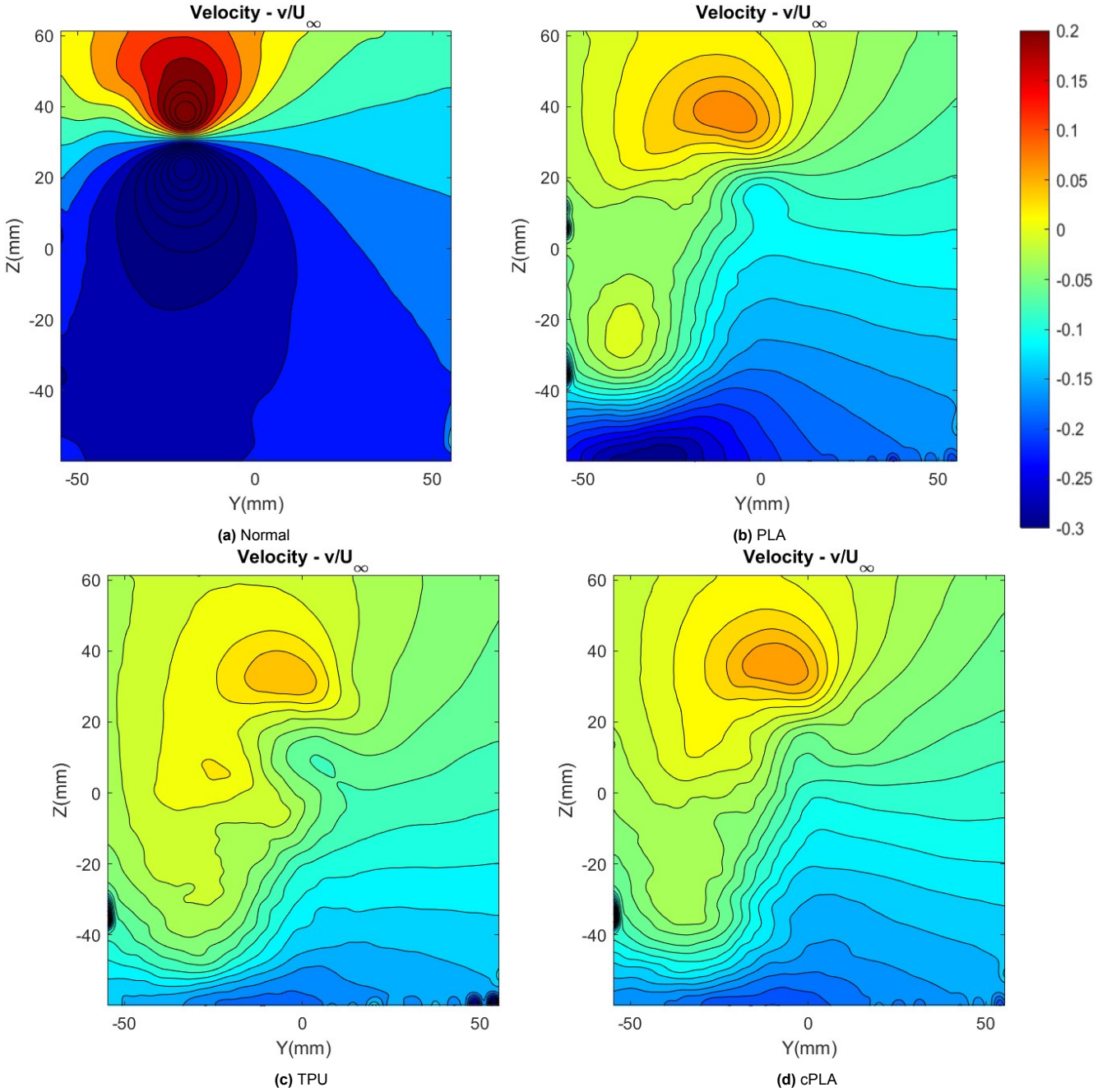

(a) Normal **(b)** PLA **(c)** TPU **(d)** cPLA

Figure 6.1: Averaged v velocity field with identified vortex core locations at Plane 1, $U_\infty = 10m/s$; $\alpha = 15°$

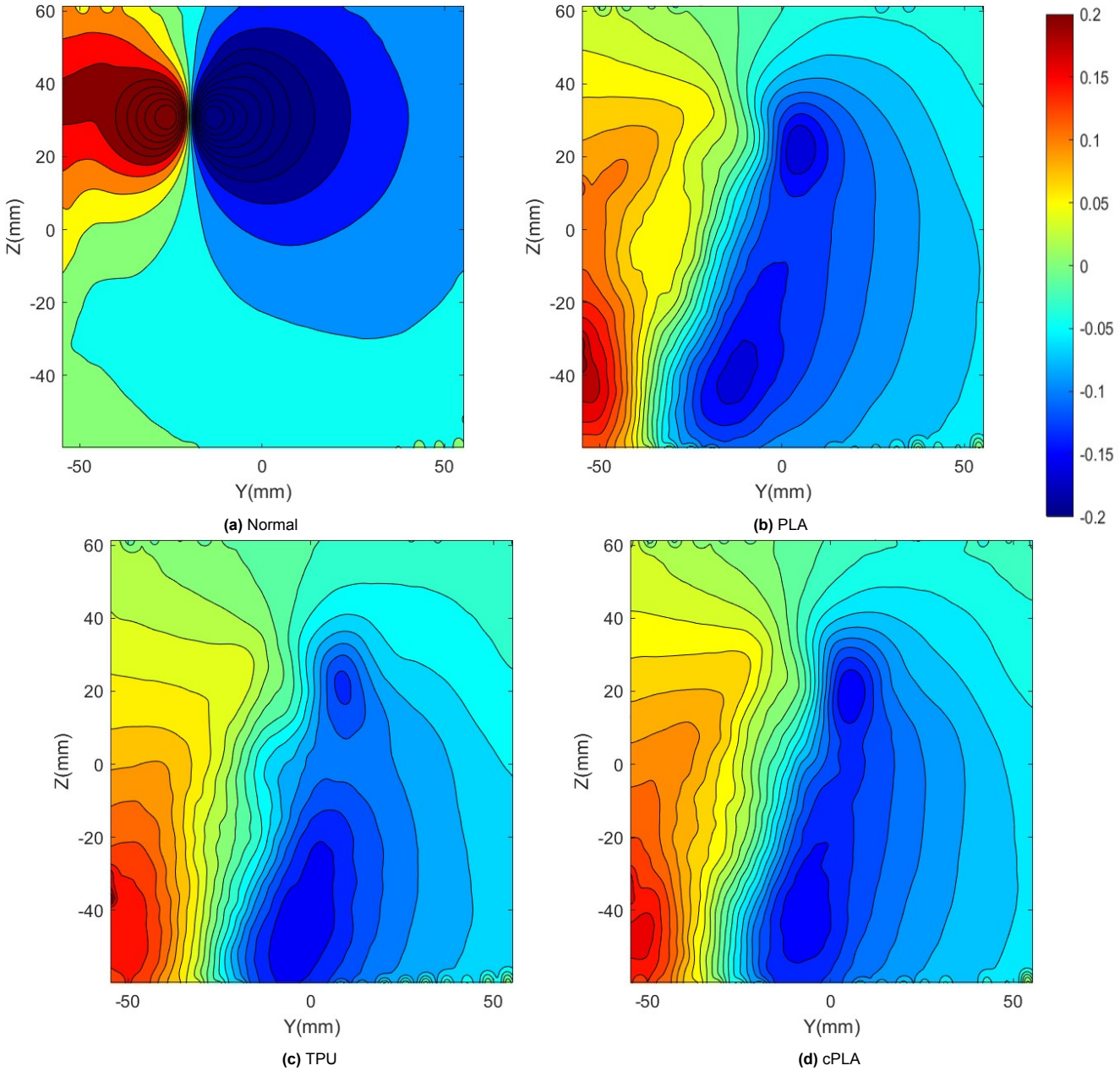

(a) Normal **(b)** PLA

(c) TPU **(d)** cPLA

Figure 6.2: Averaged w velocity field with identified vortex core locations at Plane 1, $U_\infty = 10m/s$; $\alpha = 15°$

6.3. Instantaneous Q-criterion plots

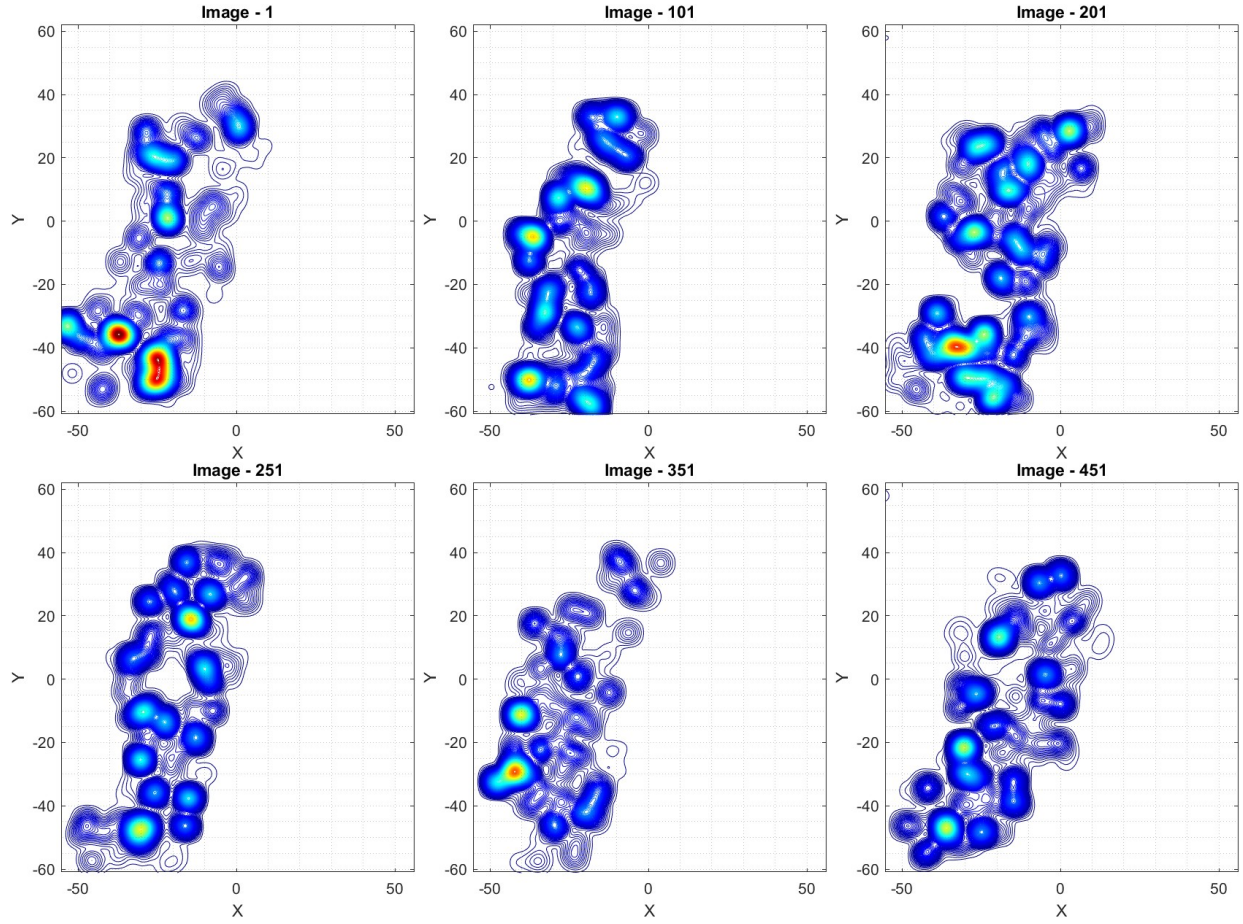

Figure 6.3: Q criterion contour of PLA winglet at $\alpha = 10°$; $U_\infty = 10m/s$

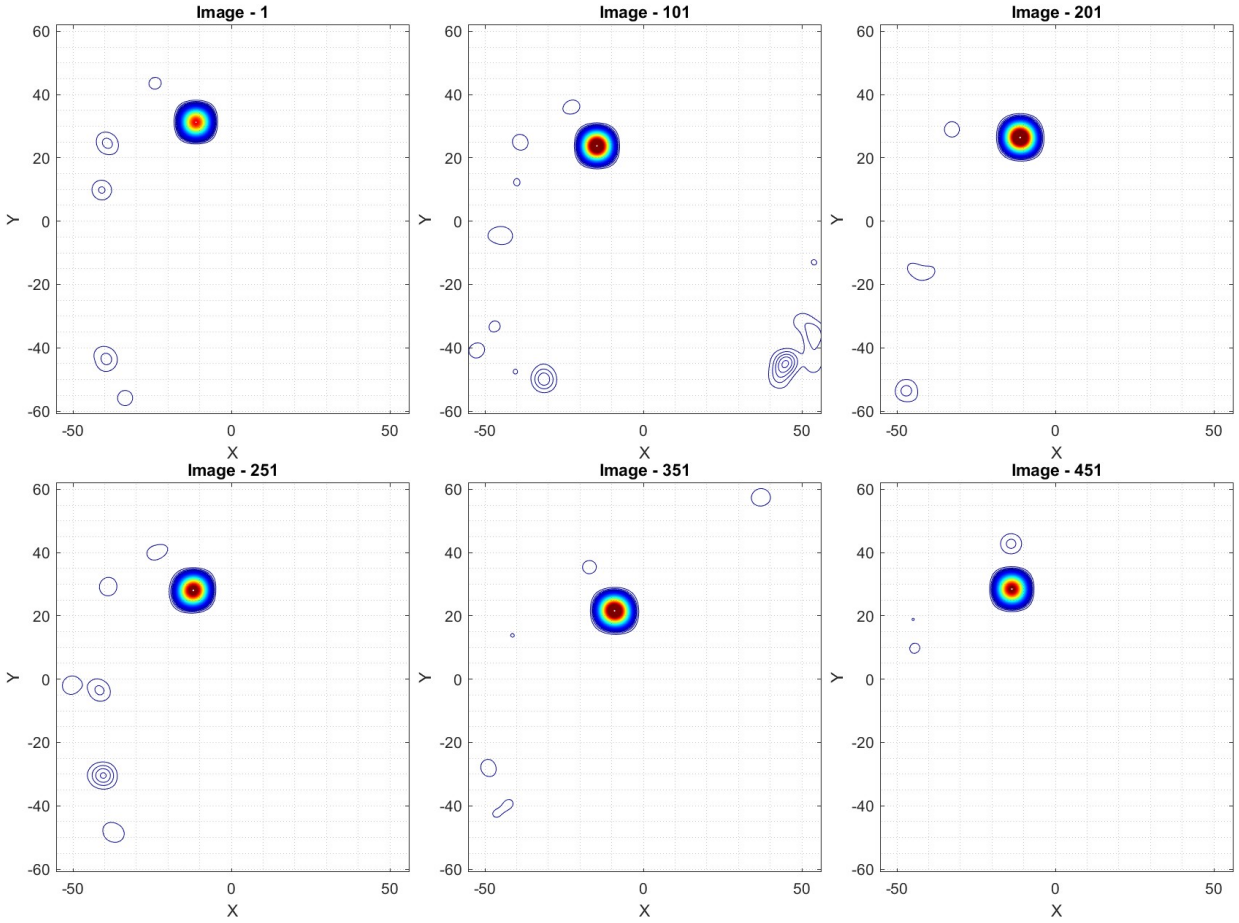

Figure 6.4: Q criterion contour of normal winglet at $\alpha = 10°; U_\infty = 10m/s$

6.4. Uncertainty in force balance data

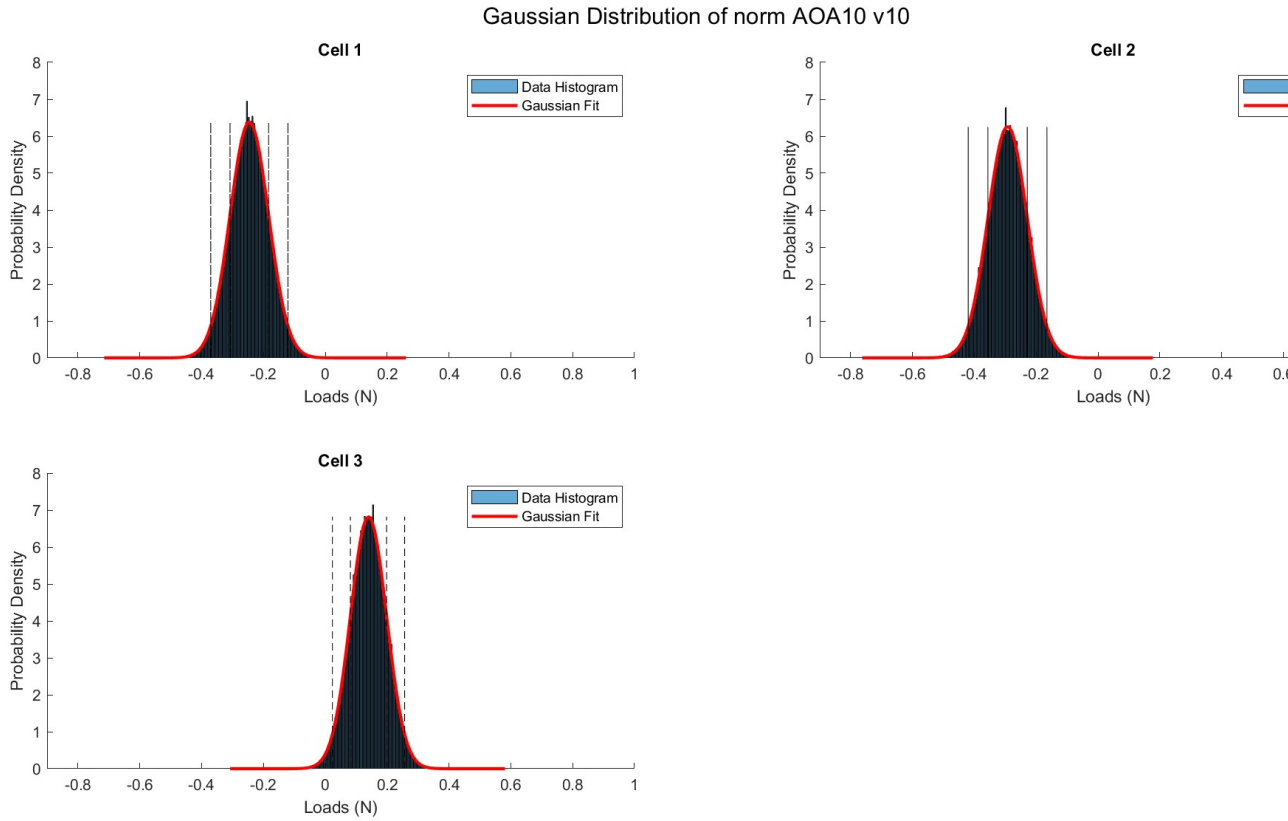

Figure 6.5: Gaussian distribution of $norm$ winglet loads from force balance; $U_\infty = 10m/s$; $\alpha = 10°$

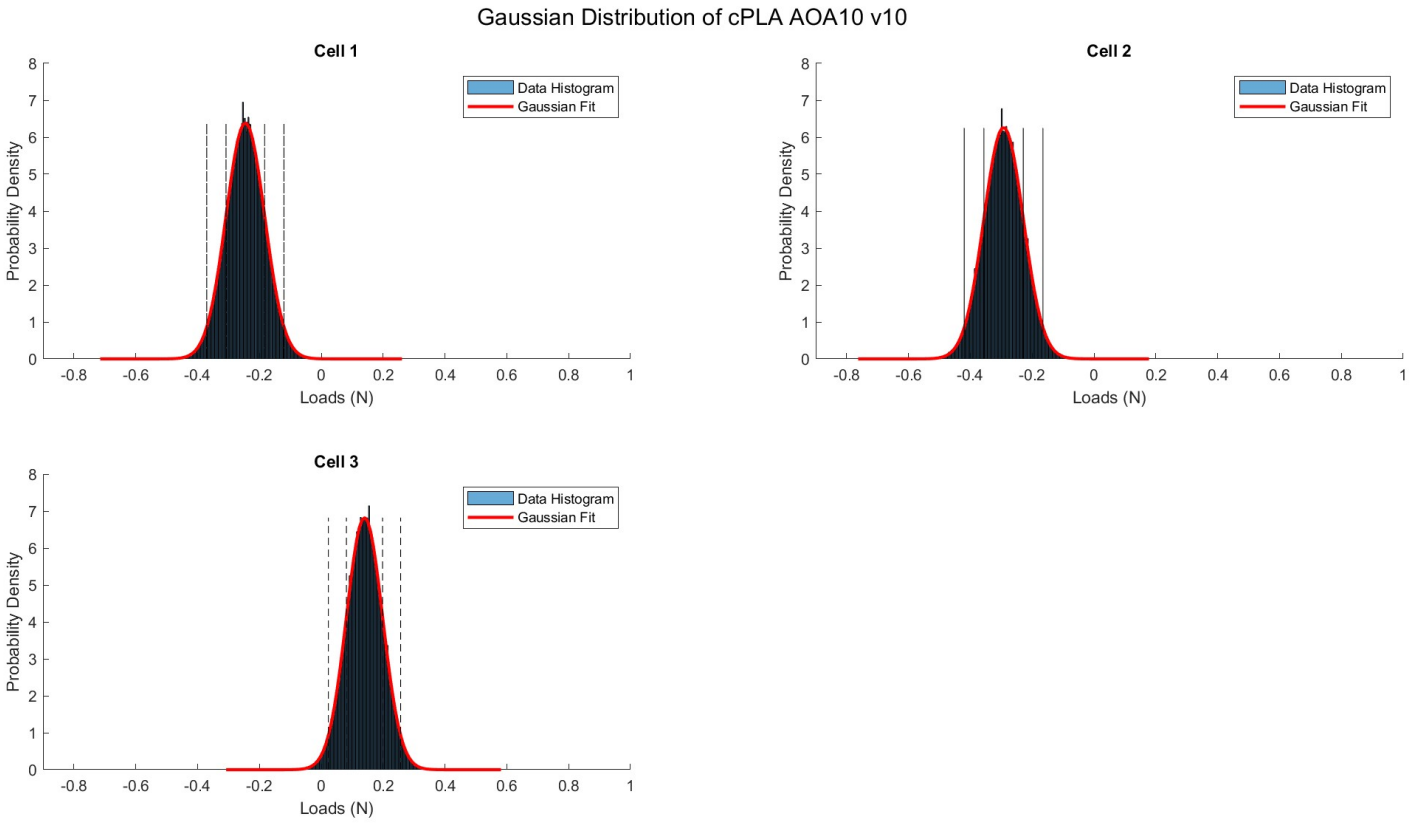

Figure 6.6: Gaussian distribution of $cPLA$ winglet loads from force balance; $U_\infty = 10m/s$; $\alpha = 10°$

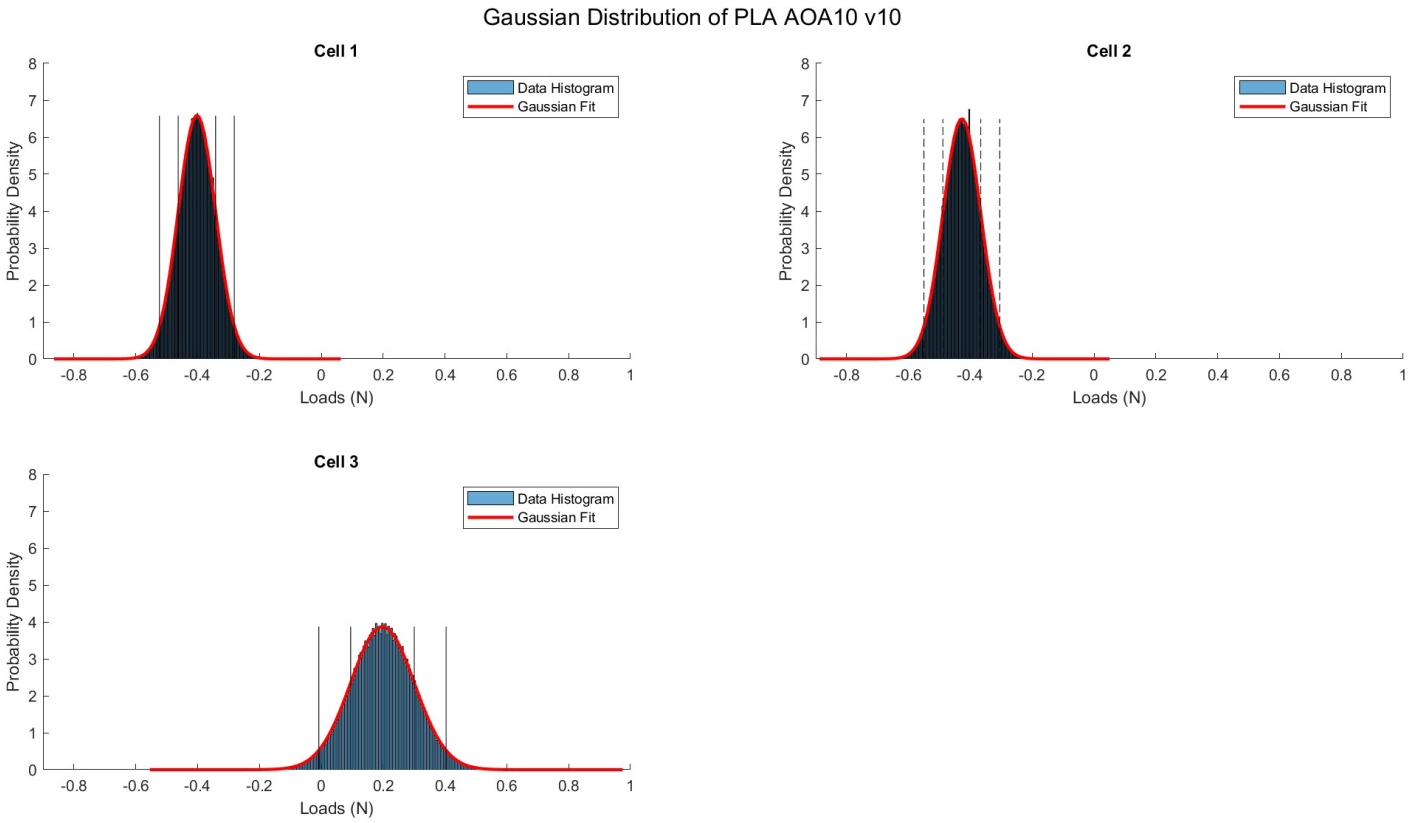

Figure 6.7: Gaussian distribution of PLA winglet loads from force balance; $U_\infty = 10m/s$; $\alpha = 10°$